United Arab Emirates University
Scholarworks@UAEU

Chemistry Theses | Chemistry

4-2019

Time-Resolved Photoluminescence of 6-Thienyl-Lumazine Flourophore In Cellulose Acetate Nanofibers For Detection Of Mercury Ions

Noura A. Humaid Al Shamisi

Follow this and additional works at: https://scholarworks.uaeu.ac.ae/chem_theses

Part of the Chemistry Commons

Recommended Citation

Al Shamisi, Noura A. Humaid, "Time-Resolved Photoluminescence of 6-Thienyl-Lumazine Flourophore In Cellulose Acetate Nanofibers For Detection Of Mercury Ions" (2019). *Chemistry Theses*. 2.
https://scholarworks.uaeu.ac.ae/chem_theses/2

This Thesis is brought to you for free and open access by the Chemistry at Scholarworks@UAEU. It has been accepted for inclusion in Chemistry Theses by an authorized administrator of Scholarworks@UAEU. For more information, please contact fadl.musa@uaeu.ac.ae.

UAEU

جامعة الإمارات العربية المتحدة
United Arab Emirates University

United Arab Emirates University

College of Science

Department of Chemistry

TIME-RESOLVED PHOTOLUMINESCENCE OF 6-THIENYL-LUMAZINE FLOUROPHORE IN CELLULOSE ACETATE NANOFIBERS FOR DETECTION OF MERCURY IONS

Noura A. Humaid Ali Al Shamisi

This thesis is submitted in partial fulfilment of the requirements for the degree of Master of Science in Chemistry

Under the Supervision of Dr. Na'il Saleh

April 2019

Declaration of Original Work

I, Noura A. Humaid Ali Al Shamisi, the undersigned, a graduate student at the United Arab Emirates University (UAEU), and the author of this thesis entitled "*Time-Resolved Photoluminescence of 6-Thienyl-Lumazine Fluorophores in Cellulose Acetate Nanofibers for Detection of Mercury Ions*", hereby, solemnly declare that this thesis is my own original research work that has been done and prepared by me under the supervision of Dr. Na'il Saleh in the College of Science at UAEU. This work has not previously been presented or published, or formed the basis for the award of any academic degree, diploma or a similar title at this or any other university. Any materials borrowed from other sources (whether published or unpublished) and relied upon or included in my thesis have been properly cited and acknowledged in accordance with appropriate academic conventions. I further declare that there is no potential conflict of interest with respect to the research, data collection, authorship, presentation and/or publication of this thesis.

Student's Signature: _____ Date: 28/5/2019

Approval of the Master Thesis

This Master Thesis is approved by the following Examining Committee Members:

1) Advisor (Committee Chair): Na'il Saleh Ibrahim

   Title: Associate Professor

   Department of Chemistry

   College of Science

   Signature _____ Date April 21st, 2019

2) Member: Muna S. Bufaroosha

   Title: Associate Professor

   Department of Chemistry

   College of Science

   Signature _____ Date April 21st, 2019

3) Member (External Examiner): Ahmed A. Mohamed

   Title: Associate Professor

   Department of Chemistry

   Institution: University of Sharjah

   Signature _____ Date April 21st, 2019

This Master Thesis is accepted by:

Dean of the College of Science: Dr. Ahmed Ali Murad.

Signature _____ Date 28/5/2019

Acting Dean of the College of Graduate Studies: Professor Ali Al-Marzouqi

Signature Ali Hassan Date 29/5/2019

Copy 5 of 8

Copyright © 2019 Noura A. Humaid Ali Al Shamsi
All Rights Reserved

Abstract

Time-resolved photoluminescence measurements were used to characterize the photophysical properties of 6-thienyllumazine (TLm) fluorophores in cellulose acetate nanofibers (NFs) in the presence and absence of mercuric acetate salts. In solution, excited-state proton transfer (ESPT) from TLm to water molecules was observed at pH from 2 to 12. The insertion of thienyl group into lumazine (Lm) introduces *cis* and *trans* conformers while keeping the same tautomerization structures. Global and target analysis were employed to resolve the true emission spectra of all prototropic, tautomeric, and rotameric species for TLm in water. However, in the NFs solid film no ESPT from TLm to a nearby water molecule was observed. The addition of NFs increases the excited-state lifetime of TLm in the solid state because of combined polarity/confinement effects. The solid-state fluorescence of TLm (in NFs) was quenched by mercuric acetate through different mechanisms—dynamic and static—depending on the applied pressure—atmospheric and vacuum, respectively. The new solid-state sensor is simple, ecofriendly, and instantly fabricated. 20 µmol TLm-loaded NFs is able to detect down to 200nmol of mercuric ions in aqueous media. The formation of non-fluorescent ground-state complex between TLm molecules and mercuric ions inside the pores of NFs was achieved under vacuum condition.

Keywords: Lumazine, nanofibers, time-resolved photoluminescence, ESPT, fluorescence quenching.

Title and Abstract (in Arabic)

الأطياف الفلورية لمركب 6- ثنيل لومازين وفترات عمرها في الحالة المهيجة داخل الألياف النانونية بغرض الكشف عن أيونات الزئبق

الملخص

تم الاستعانة بالقياسات الزمنية للاطياف الفلورية للتعرف على الخصائص الكيمائية-الضوئية لمركب 6-ثنيل لومازين داخل ألياف السيليلوز النانونية في حال وجود وغياب ايونات الزئبق. بالاضافة الى ذلك، تم دراسة انتقال البروتونات من المركب، في الحالة المهيجة، الى جزيئات الماء المحيطة عندما يتراوح معدل الحموضة في المحلول بين 2-12. و تشير نتائج الدراسة إلى أن اضافة مجموعة الثيوفين الى مركب اللومازين أدت إلى تباين المركب بين الشكلين (سيس) و (ترانس)، مع الحفاظ على بقية الاشكال المرتبطة بعمليات انتقال البروتونات. وكما تم التعرف على الأطياف لجميع الاشكال المحتملة لهذا المركب، كل على حدى، من خلال التحليل المتقدم للفترات الزمنية للأطياف. في المقابل لم يتم رصد عمليات انتقال البرتونات من المركب إلى جزيئات الماء المحيطة خلال تواجد المركب داخل الالياف النانونية. وقد لوحظ زيادة الفترة العمرية للحالة المهيجة عند تواجد المركب في الألياف، والذي قد يعود إلى تأثير القطبية والاحتجاز. أدى وجود أيونات الزئبق الى اسخماد التألق الفلوري للمركب بطرق مختلفة اعتماداً على ظروف الضغط المطبقة خلال تحضير المنتج النهائي. من الجدير بالذكر أن ظروف اضافة المركب للألياف في وعاء مفرغ من الهواء، أدت حصرياً إلى تكوين معقَد بين المركب وايونات الزئبق داخل فجوات الألياف. يعتبر جهاز الاستشعار سهل التصنيع و مفيد للبيئة، و باستطاعته استشعار وجود ايونات الزئبق بتراكيز منخفضة (0.2 مايكرومول – 2 مايكرومول).

مفاهيم البحث الرئيسية: لومازين، الألياف النانونية، القياسات الزمنية، انتقال البروتونات في خلال الحالة المهيجة، استخماد التألق الفلوري.

Acknowledgements

I am sincerely thankful and grateful to my supervisor Dr. Na'il Saleh for enrolling me in this research topic, which expanded my knowledge and experience in the field of photoluminescence. I really appreciate his constant help and his way of solving regarding issues. My thanks also go to Dr. Yaser Greish for his fruitful advice through my preparation of this thesis.

I would like to thank the chairman, Dr. Mohamed Alazab, and all members of the Department of Chemistry at the United Arab Emirates University, for their continuous support as a master student and as an academic assistant.

Special thanks go to my parents, brothers, and sisters for their endless encouragement and support in all stages of my life and helping me believing in myself.

Dedication

To my beloved parents and family

Table of Contents

Title i
Declaration of Original Work ii
Copyright iii
Approval of the Master Thesis iv
Abstract vi
Title and Abstract (in Arabic) vii
Acknowledgements viii
Dedication ix
Table of Contents x
List of Tables xii
List of Figures xiii
List of Abbreviations xiv
Chapter 1: Introduction 1
1.1 Overview 1
1.2 Statement of the problem 1
1.3 Relevant literature 1
1.4 Steady-state (PL) and time-resolved photoluminescence (TRES) measurments 4
1.5 TRPL data analysis method 8
1.6 Photophysical processes 10
1.6.1 Exited state proton transfer 10
1.6.2 Quenching of fluorescence 12
1.7 Time-resolved photoluminescence (TRPL) of 6-thienyl-lumazine fluorophore in cellulose acetate nanofibers 13
Chapter 2: Methods 18
2.1 Reagents and synthesis Procedures 18
2.2 Interactions of TLm with cellulose acetate nanofibers (NFs) 18
2.3 Interactions of TLmNFs with mercuric acetate 19
2.4 Preparation of $TLmHg^{2+}$ complex in solid state 19
2.5 Techniques 19
2.5.1 Absorption/steady-state fluorescence spectroscopy 19
2.5.2 Fourier transform infrared (FTIR) spectroscopic measurements 20
2.5.3 Scanning electron microscopy (SEM) 20
2.6 The pH-titration studies 20

2.7 Time-resolved photoluminescence (TRPL) measurements 20
2.7.1 Kinetic (global and target) analysis 21
2.7.2 Average excited-state lifetime calculation 22

Chapter 3: Results and Discussion 23
3.1 Conformational and tautomerization effects on the photoacid behavior of 6-thienyl-substituted lumazine chromophore in aqueous solution 23
3.2 Spectrophysics of TLm in cellulose acetate nanofibers (confinement vs. polarity effects) 31
3.3 Fluorescence detection for mercuric acetate in solid state and nanofibers (static vs. dynamic quenching) 36
3.4 Complex formation of TLm with mercuric acetate in the solid state 39

Chapter 4: Conclusion 40

References 41

List of Publications 47

Appendix 48

List of Tables

Table 1: The extracted excited-state lifetimes in nanoseconds of all tautomers and conformers of TLm in water from the global/target analysis of TRPL data at different pH values. 28
Table 2: The extracted excited-state lifetimes in nanoseconds of all species of TLm in solid state with and without the NFs from the global analysis of TRPL data. Range of DAS maxima is shown in brackets. Average excited-state lifetime at 450 nm was calculated 35

List of Figures

Figure 1: Jablonski diagram 2
Figure 2: Emission decay traces of three species, which are characterized by different lifetimes. 6
Figure 3: Emission decay trace for a mixture of two species. Their excited-state lifetimes are indicated by τ_1 and τ_2 7
Figure 4: Emission decay of a fluorophore, IRF and the single exponential fit 8
Figure 5: Illustration of TCSPC electronics. 9
Figure 6: TCSPC method of signal conversion. 9
Figure 7: Excited state de-protonation of photo-acids 11
Figure 8: 6-Thienyllumazine (6-TLm) and other similar pteridines 15
Figure 9: Cellulose acetate nanofibers (NFs), and the two possible loading of TLm in NFs under vacuum and atmospheric conditions 16
Figure 10: TLm neutral, anionic, and dianionic tautomers present in aqueous solution 24
Figure 11: Emission spectra of different prototropic species of TLm excited at 375 nm 25
Figure 12: SEM images and EDS spectra for cellulose acetate nanofibrs with and without stirring in TLm solution under atmospheric conditions 31
Figure 13: Photoluminescence spectra in the solid state for TLm before and after stirring with NFs under atmospheric and vacuum pressure; and their fluorescence decay traces monitored at 400 nm and 450 nm after 375 nm excitation 33
Figure 14: Photoluminescence spectra and and fluorescence decay traces of solid TLmNFs(vac) and TLmNFs(atm) before and after addition of mercuric ions at various molar ratios 37
Figure 15: The dependence of the average and the longest excited-state lifetimes (τ) monitored at 450 nm for TLmNFs(atm) on the number of added moles of Hg^{2+} 39

List of Abbreviations

DAS	Decay Associated Spectra
ESIPT	Intramolecular Excited-State Proton Transfer
ESPT	Exited-State Proton Transfer
FTIR	Fourier Transform Infrared Spectroscopy
IRF	Instrument Response Function
Lm	Lumazine
NFs	Cellulose Acetate Nanofibers
PL	Photoluminescence
Q	Quencher
SAS	Species Associated Spectra
TCSPC	Time Correlated Single Photon Counting
TRPL	Time-Resolved Photoluminescence
TLm	6-thienyllumazine

Chapter 1: Introduction

1.1 Overview

The study of photophysical phenomena utilizing time-resolved photoluminescence measurements can be a great assistant in understanding the behaviour (structure and dynamics) of molecules in their excited states (fluorophores). It can also provide knowledge about the surrounding local environment, which is experienced by the fluorophore. Photoacidity and fluorescence quenching are two important photophysical behaviours of a fluorophore. They can be employed as an indicator for any variation in the sample medium or the presence of other species, which has the potential to interact with the emissive molecule in question.

1.2 Statement of the problem

To characterize the photophysical properties of a new lumazine derivative at different pH values, in quest for unfolding the nature of conformers or tautomer which can transfer proton to a nearby water molecule in the excited state. In addition, the aim is to decipher the mechanism of fluorescence quenching by mercury ions inside the cellulose acetate nanofibers.

1.3 Relevant literature

Luminescence is generally defined as the emission of photons during the electronic relaxation of an excited substance from a higher energy state to a lower energy state. Luminescence can also be categorized into two types: fluorescence and phosphorescence (Figure 1). Generally, the main difference between the two types of emission arises from the change in the spin direction of the excited electron relative to its spin in the ground state, which leads to different emission rates and excited-state lifetimes for the two processes (Lakowicz, 2006). Perrin-Jablonski diagram in Figure

1 illustrates all other processes, besides fluorescence, that are possibly involved during the population transfer from the excited state to the ground state of a fluorophore.

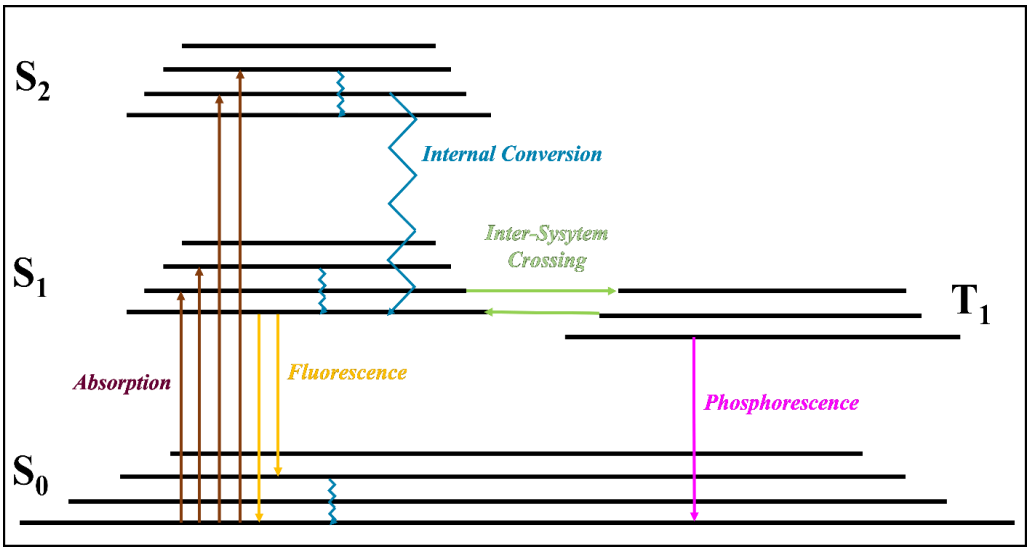

Figure 1: Jablonski diagram

Excitation is the first step when molecule interacts with light, during which a transition from the ground state (S_0) to the higher energy electronic state (S_1 or S_2) is induced by the absorption of light, or other types of energy such as heat or electrical energy. This transition takes place within a time of 10^{-15} s. During the lifetime of the excited state (S_1 or S_2), some of the initially absorbed energy possibly can be lost, in what is called internal conversion, or as heat to the surrounding because of an instant vibrational relaxation from S_2 to S_1. This kind of transition usually takes place within 10^{-12} s, that is much faster than fluorescence which occurs within 10^{-9} s; therefore it usually precedes fluorescence emission. Additionally, internal conversion can proceed from S_1 to S_0 by analogous to fluorescence emission. An additional transition, which a molecule in S_1 possibly undergoes, mostly in the presence of heavy atoms, is

intersystem crossing from S_1 to the first triplet electronic state T_1. This kind of transition is forbidden according to specific rules in quantum mechanics. Fluorescence usually originates from the lowest vibrational energy level of S_1 in a time scale of nanoseconds. On the other hand, phosphorescence is the kind of luminescence that originates from T_1 and occurs within a much longer time than fluorescence, since it is precedent by internal conversion ($S_1 \rightarrow T_1$) (Lichtman & Conchello, 2005).

Prior to fluorescence emission or other excited state transition, the time that an excited molecule spends in higher energy levels is called an *excited-state lifetime* and considered a characteristic property of a fluorescent molecule. Several factors can tune the excited-state lifetime value, which includes the structure of molecule and the nature of the surrounding medium. In addition to excited-state lifetime, *fluorescence quantum yield* is normally used to characterize the emission of a fluorophore (Valeur & Berberan-Santos, 2013). Quantum yield simply indicates the ratio of the intensity of the emitted light intensity to that of the absorbed light:

$$\phi = \frac{Intesity\ of\ emitted\ fluorescence}{Intensity\ of\ absorbed\ light} = \frac{I_f}{I_{abs}} \tag{1.1}$$

Consider the following kinetic mechanism for the population transfer between the ground state and the excited state of a fluorophore:

Absorption: $M + light \rightarrow M^*$ $\quad rate = I_{abs}$

Radiative decay: $M^* \rightarrow M + light$ $\quad rate = k_r[M^*]$

Non-radiative decay: $M^* \rightarrow M$ $\quad rate = k_{nr}[M^*]$

Applying the steady-state approximation for the change in the concentration of the excited species, M* gives the following kinetic expression:

$$\frac{d[M^*]}{dt} = I_{abs} - k_r[M^*] - k_{nr}[M^*] = I_{abs} - (k_r + k_{nr})[M^*] = 0$$

$$I_{abs} = (k_r + k_{nr})[M^*]$$

substituting in eq 1.1 leads to the following expression for quantum yield:

$$\phi = \frac{k_r}{k_r + k_{nr}} \tag{1.7}$$

However, considering only the decay mechanism of the excited molecules in eqs 1.2 and 1.3, the change in concentration of M* with time becomes:

$$\frac{-d[M^*]}{dt} = k_r[M^*] + k_{nr}[M^*]$$

The final rate law by integration is then:

$$[M^*] = [M]_0 \, e^{(k_r + k_{nr}) - t}$$

The time at which the concentration of excited molecule at the first singlet state reaches 0.368 (1/*e*) of its initial value after excitation is usually referred to as (τ), and it equals to the reciprocal of decay rate constant:

$$\tau = \frac{1}{k_r + k_{nr}} \tag{1.10}$$

Excited-state lifetime τ can also be expressed as:

$$\tau = \frac{1}{k_r + k_{nr}} = \frac{\phi}{k_r} \tag{1.11}$$

1.4 Steady-state (PL) and time-resolved photoluminescence (TRES) measurments

Fluorescence emission and its implementation as a spectroscopic tool is considered a powerful one to provide a better knowledge and understanding about

nature and behaviour of chemicals, which glows when excited by a specific light energy. Generally, photoluminescence measurements are either classified as steady-state (PL) or time-resolved photoluminescence (TRPL) measurements. In comparison with TRPL, samples analyzed using PL measurements are illuminated with a continuous beam and the emitted signal is recorded continuously as a function of the emitted wavelength. However, TRPL data are obtained utilizing a short pulse of light, in which the fluorescence intensity decay time is recorded after sample excitation. PL spectra are considered an average of the TRPL spectra across the entire wavelengths (Engelborghs & Visser, 2016).

In our laboratory, these time domain measurements of emission lifetime are usually conducted using the *Time Correlated Single Photon Counting* (TCSPC) method. When a single fluorophore absorbs the energy of a short pulse, the decay of its emission intensity (I(t)) is represented by an exponential decay equation, as follows:

$$I(t) = I_0 \, e^{-t/\tau} \tag{1.12}$$

where I_0 is the intensity at time = 0 and τ is the excited state lifetime.

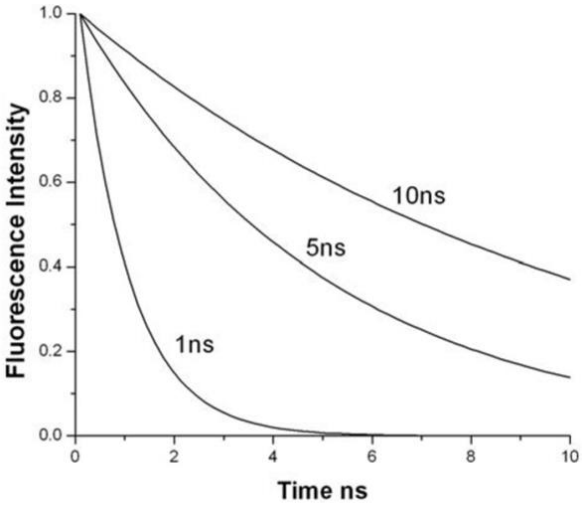

Figure 2: Emission decay traces of three species, which are characterized by different lifetimes 1, 5 and 10 ns (Reprinted with permission from (Owens, 2009), Copyright NUI Galway)

According to this equation, the intensity of fluorescence reaches 36 % of its initial value when $t = \tau$. Figure 2 shows three different single exponential decays, which represent fluorescent species with different excited-state lifetimes. In the event where more than one fluorophore is presented in the studied sample, the resultant decay (Figure 3) does not follow eq 1.12, but instead it is described using sum of exponentials decay function, as follows:

$$I(t) = \sum_{i=0}^{n} \alpha_i \, e^{-t/\tau_i} \tag{1.13}$$

where α represents the contribution of each fluorophore (i) to the total decay function and τ_i is the individual excited state lifetime. However, the fraction that each decay contributes to the PL spectrum is calculated by f_i:

$$f_i = \frac{\alpha_i \tau_i}{\sum_j \alpha_j \tau_j} \tag{1.14}$$

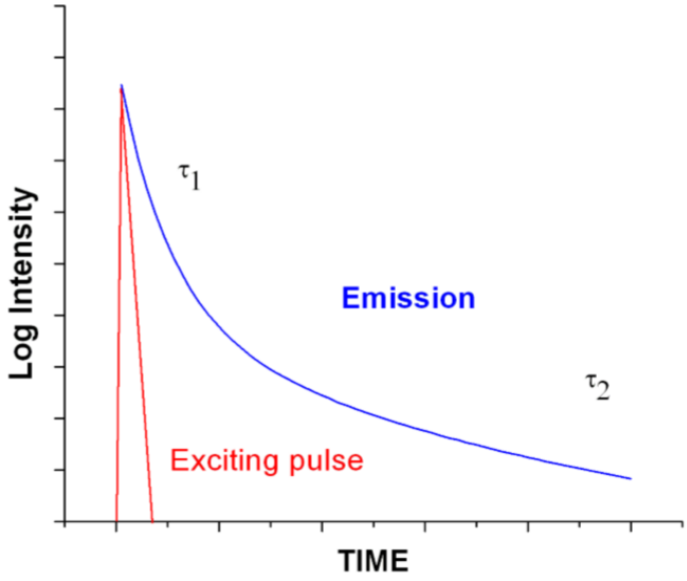

Figure 3: Emission decay trace for a mixture of two species. Their excited-state lifetimes are indicated by τ1 and τ2 (Reprinted with permission from (Owens, 2009), Copyright NUI Galway)

The measured emission decay usually contains contribution from the *instrument response function* (IRF), which reflects the time resolution of the instrument. The IRF is simply measured using a sample with a light scattering property such as the Ludox solution. Figure 4 shows how IRF usually appears relative to the measured emission decay.

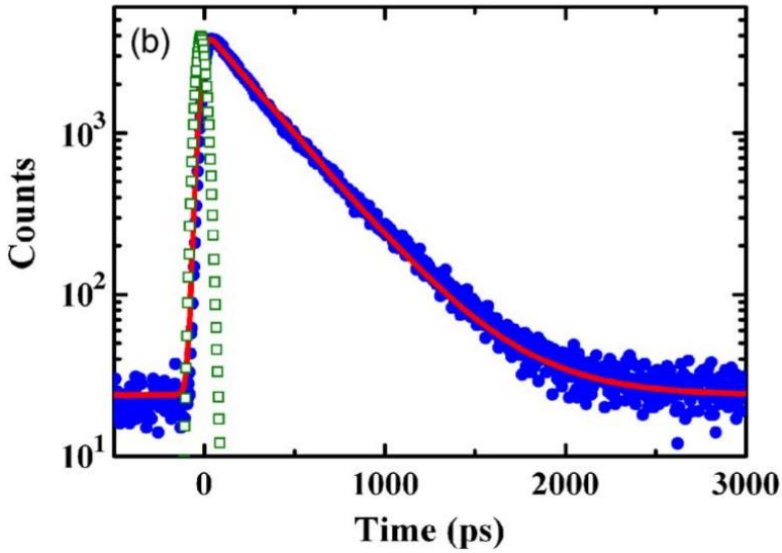

Figure 4: Emission decay of a fluorophore (blue dots), IRF (empty green squares) and the single exponential fit (red line), see data analysis (Reprinted with permission from (Stevens et al., 2006), Copyright Applied Physics Letters)

1.5 TRPL data analysis method

TCSPC is considered the leading technique implemented for TRPL measurements. It involves processing the time distribution of the emitted photons from a given sample following the short excitation pulse. Specifically, it measures the time difference between the excitation pulse and the detection of the emitted photons. Then, it converts such time difference to a voltage value (Figure 5). The final histogram (Figure 6) manifests how the emission intensity at a given wavelength varies with time. Therefore, TCSPC requires a special setup of electronics as shown in Figure 5 (Lakowicz, 2006).

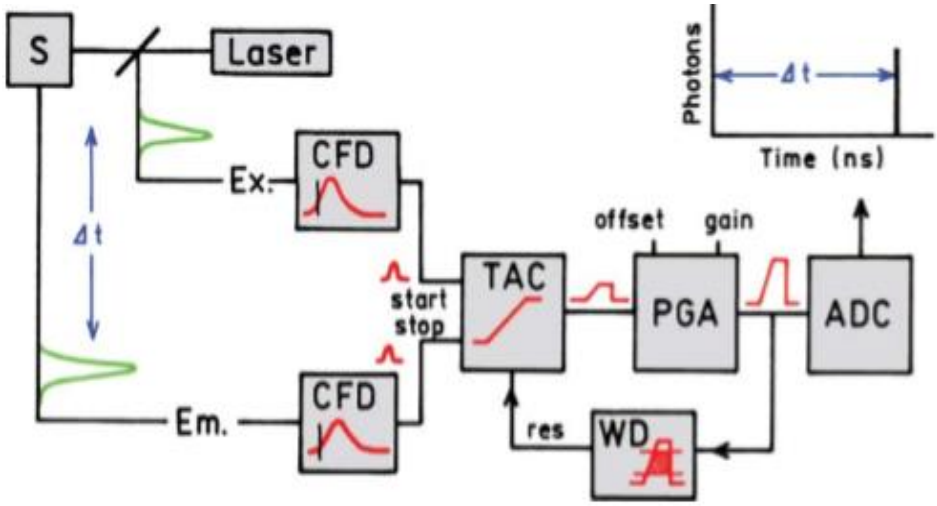

Figure 5: Illustration of TCSPC electronics. S = sample, Δt = the time difference between excitation and emission signals, CFD = discriminator to filter noise signals, TAC = time-to-amplitude convertor, WD = widow discriminator and PGA = programmable gain amplite, which are electeronic units to minimize false readings and amplify the signals. ADC = amplitude digital convertor (Reproduced with permission from (Lakowicz, 2006). Copyright agreement by Springer)

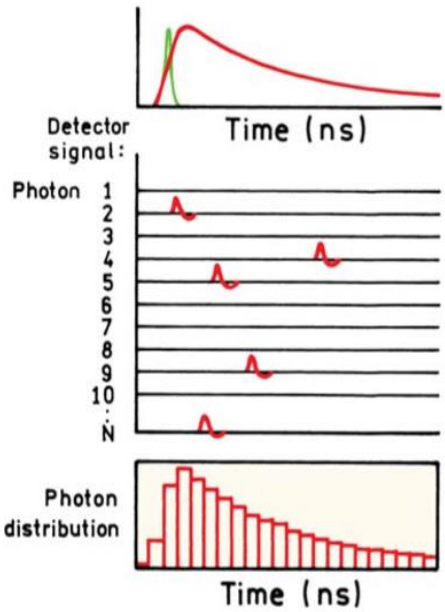

Figure 6: TCSPC method of signal conversion. (Reproduced with permission from (Lakowicz, 2006) Copyright agreement by Springer)

1.6 Photophysical processes

Among the different implementation of TRPL technique is to understand how a fluorophore in the excited state interacts with its surrounding environment, which is difficult to unfold using many other techniques. This kind of information can be retrieved through the analysis of the emission decays using a proper method of analyses, as described below. In our work, we are focusing on two photphysical processes, excited-state proton transfer (ESPT) and fluorescence quenching, which are modulated by the local environment.

1.6.1 Exited state proton transfer

Reactions involving proton transfer are of essential importance, since it is related to controlling the reactivity of organic molecules in many reactions, (Hsieh, Jiang, & Chou, 2010) defining the ion mobility in many materials, (Kundu et al., 2015) and understanding several life processes in organisms (Li et al., 2010). Release of a proton or more defines the acidic property of a compound. Photoacids are chromophores having the ability to donate proton (H^+) to the nearby solvent molecules at the excited-state, (Green, Gajst, Simkovitch, Shabat, & Huppert, 2017) normally at lower pH value than their acid-dissociation constant (pK_a) of their ground state (Halbritter et al., 2017). Because protons are released to the surrounding media, the process is described as an intermolecular photophysical process. However, when the proton is transferred after excitation, from a donating group to an accepting one within the same molecule, it is defined as an intramolecular photophysical process. The former is called excited-state proton transfer (ESPT), whereas the latter is defined as intramolecular excited-state proton transfer (ESIPT) (Serdiuk & Roshal, 2017).

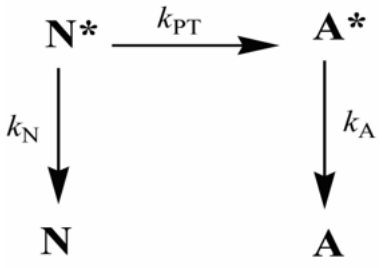

Figure 7: Excited state de-protonation of photo-acids

Figure 7 shows the kinetic scheme, which corresponds to an ESPT process, in which N* represents the excited neutral form (before proton transfer) of a fluorophore population while A* is the excited anionic form (after proton transfer). The rate constants k_N and k_A correspond to decay to the ground state for neutral and anionic, respectively and k_{PT} is the rate of proton transfer from N to A. The population transfer of neutral excited state (N*) to anionic excited state (A*) is considered as an example in accordance with the known two-state model as described below:

$$\frac{dN^*(t)}{dt} = -(k_N + k_{PT})\, N^*(t)$$

$$\frac{dA^*(t)}{dt} = k_{PT} N^*(t) - k_A A^*(t) \qquad (1.14)$$

$$N^*(t) = N_0^*\, e^{-(k_N + k_{PT})t} = N_0^*\, e^{\frac{-t}{\tau_1}}$$

$$A^*(t) = -\frac{N_0^*\, k_{PT}}{k_N + k_{PT} - k_A}\, e^{-\frac{t}{\tau_1}} + \frac{N_0^*\, k_{PT}}{k_N + k_{PT} - k_A}\, e^{-\frac{t}{\tau_2}}$$

$$\tau_1 = \frac{1}{k_N + k_{PT}} \qquad \tau_2 = \frac{1}{k_A}$$

1.6.2 Quenching of fluorescence

Fluorescence Quenching is defined as a reduction in the normal intensity of a fluorophore emission. Many factors can cause emission quenching such as the presence of molecular oxygen, halides, acidity or basicity of the media, metal ions, just to name a few.

The mechanism by which the fluorescence is quenched can be described as either static or dynamic. In the dynamic case, the intensity of emission decreases because of the creation of new deactivation process (eq 1.7) through collision in the presence of a quencher (Q).

$$Q + M^* \rightarrow M + Q \qquad\qquad rate = k_q[Q]\,[M^*]$$

Consequently, the emission quantum yield in the presence of dynamic quencher over becomes:

$$\phi_q = \frac{k_r}{k_r + k_{nr} + k_q[Q]}$$

The equation confirms the reduction in quantum yield by dynamic quenching. The ratio of ϕ_q/ϕ, where ϕ is the emission quantum yield in the absence of a quencher (eq 1.7), becomes:

$$\phi_q/\phi = 1 + \tau\, k_q[Q]$$

and it is known as the *Stern-Volmer* equation. Since both of emission intensity and lifetime are related to the quantum yield, the above equation can also be written as:

$$\frac{I_0}{I} = \frac{\tau_0}{\tau} = 1 + \tau_0 k_q[Q]$$

On the contrary, static quenching occurs whenever a fluorophore forms a stoichiometric complex with the quencher in the ground state. Because the complex is non-emissive, the measured emission intensity decreases upon the addition of the quencher to the fluorophore by virtue of the reduction in the number of fluorescent species. However, no change in the excited-state lifetime is expected since the number of deactivating channels remains fixed with the addition of the quencher. To distinguish the two types of quenching from each other, intensity measurements are not enough, since $\frac{I_0}{I}$ is related to quencher concentration in both cases. However, lifetime decreases as a function of quencher concentration in the case of the dynamic quenching and remains unchanged during static quenching (Lakowicz, 2006).

1.7 Time-resolved photoluminescence (TRPL) of 6-thienyl-lumazine fluorophore in cellulose acetate nanofibers

For so many years, there have been numerous reports dealing with the utilization of nanofibers in broad range of applications, such as chemical sensing, filtration, drug delivery, tissue engineering, oil industry, and energy research (Klemm et al., 2011; Omollo et al., 2013) of interest, the utilization of the large surface area-to-volume ratios of those electrospun nanofibers (Nguyen et al., 2013).

The characterizations of nanofibers by steady-state (Wang et, Meng, Huang, & Qian, 2012) (PL) and time-resolved photoluminescence (TRPL) techniques (Davis et al., 2011; Sun et al., 2015) have been reported by many researchers for many applications. In the TRPL measurements, which have recently come to fore, the time dependence of the fluorescence intensity or spectrum is monitored after excitation with a brief light flash, reflecting directly the rate constants of the depopulating processes of the excited states. The excited-state lifetime is, then, the time when the initial

population of the excited state reaches 1/*e* its initial value (Valeur & Berberan-Santos, 2013). It provides information on how the energy, orientation and movement of a chromophore change relative to the framework of the surrounding microenvironment. Our specific aspiration comes from the fact that such TRPL techniques offer the ability to obtain more information about the local environments when compared to the stationary PL measurements, coupled with the fact that the fluorescence lifetime is an absolute measure, whereas the steady-state just provides relative and average information (Valeur & Berberan-Santos, 2013).

Exploring the properties of lumazine (Lm) derivatives at both the ground and the excited states should help in explaining the properties of structurally related flavins and pterins (Figure 8) in their surrounding microenvironment. This motivates us to specifically select 6-thienyllumazine (TLm in Figure 8) as the chromophore to probe cellulose acetate nanofibers (NFs, Figure 9) (Greish, et al., 2010). The spectrophysics of Lm in a series of solvents with varying dielectric constants and hydrogen bonding properties was studied by fluorescence spectroscopy and density functional theory calculation. The analysis revealed that the hydrogen bond acceptance ability of the solvent is the most important parameter, which characterizes the excited state behavior of Lm (Moyon et al., 2013). Moreover, Lm contains both acidic and basic groups in proximity and, thus, may undergo intramolecular proton transfer (tautomerization) in the excited state. Intermolecular excited state proton transfer (ESPT) to a solvent has also been widely researched for many years (Agmon, 2005; Förster, 1950; Ireland & Wyatt, 1976; Mohammed, Pines, Dreyer, Pines, & Nibbering, 2005; Mondal et al., 2005; Presiado , 2010; Simkovitch & Huppert, 2017). The ESPT process enables those chromophores to produce protons at pH value, upon excitation, lower than that in the ground state. For example, such photoacid behaviour of Lm has been specifically

studied by Huppert research group utilizing TRPL spectroscopy in water (Presiado et al., 2010; Simkovitch & Huppert, 2017) and of other photoacids when adsorbed on cellulose, (Simkovitch & Huppert, 2015a) starch, and other biomaterials (Simkovitch & Huppert, 2015b).

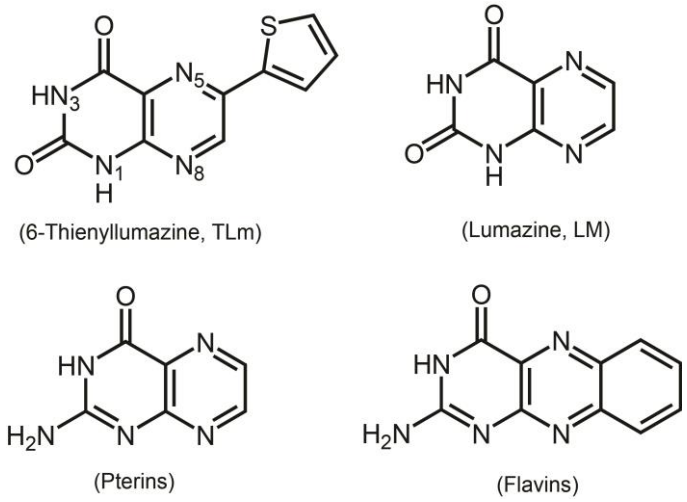

Figure 8: 6-Thienyllumazine (6-TLm) and other similar pteridines

In the present work, the ESPT phenomenon is taken into consideration when TLm is used to probe cellulose acetate nanofibers (NFs, Figure 7), which were obtained by electrospinning in our laboratory (Greish et al., 2010). The TRPL of TLm molecules are then measured to decide which factors inside the NFs affect their proximity to mercury ions. Electrospinning is one simple technique to fabricate nanofibers (Ohkawa, 2015). It is based on exposing a solution of the polymers to a high voltage. The nanofibers have special advantages because of their good mechanical properties that could sustain reversible sensing and high surface area for water absorbing (Nguyen et al., 2013).

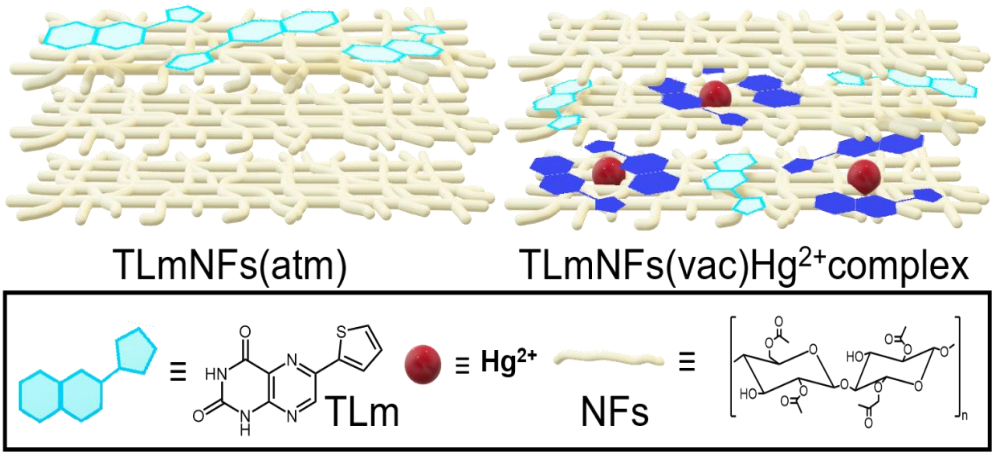

Figure 9: Cellulose acetate nanofibers (NFs), and the two possible loading of TLm in NFs under vacuum (vac) and atmospheric (atm) conditions. Cyan and blue colors of TLm reflect the static quenching by mercury ions (red ball) under vacuum

In the present study, not only we are motivated to report more information about the structure of NFs, but also, we seek to fabricate a solid-state sensor for Hg^{2+}. Lm compounds are known to form coordination bonds with biologically essential metals in some metalloenzymes (Sigel, 2004). In fact, TLm itself was designed and prepared by our research group (Saleh et al., 2007) as selective fluorescent sensors for pH (Saleh et al., 2012) and heavy metal ions, such as Cd^{2+} and Hg^{2+} in pure water (Saleh et al., 2007; Saleh et al., 2009). Thus, our second aim is to fabricate TLmNFs as a fluorescence-based solid sensor to detect micromoles or less of Hg^{2+} ions, urged by the increasing global concern on water pollutions (Mahato et al., 2014). In our approach, the fabrication of TLmNFs was established by stirring directly in aqueous solution, instead of electrospinning, the mixture of the fluorescent probe and the precursor polymer. The later procedure was used for the detection of several metal ions using nanofibers, such as Cu^{2+}, Cr^{3+}, $Fe^{3+}$and Hg^{2+} ions (Wang et al., 2012; X et al., 2002). However, we were inspired to consider the former procedure, which allows TLm to distribute freely throughout the NFs system. We also aim to benefit from the

superiority of TRPL techniques for detecting mercury ions, when compared to the stationary methods (Wang et al., 2012; X et al., 2002). In fact, the belated loading of many fluorescent probes on cellulose-related biomaterials has also been employed by many researchers. For example, Kaur et al. (2016) published a dual colorimetric and fluorescent sensor for Hg^{2+} and Cu^{2+}, which is simply made of phenothiazine-bound TLC plates/test papers. The detection limit of the sensor was determined to be 1.5 nM for Hg^{2+} and 3 nM for Cu^{2+}.

Putting all together, the present work is aimed at understanding the mechanism of fluorescence quenching utilizing TLm and mercuric acetates as model guests for both optimizing the performance of the selected nanofibers for sensing application. The results should also help in expanding the utilization of nanofibers for other applications in biotechnology, nanotechnology, and beyond.

Chapter 2: Methods

2.1 Reagents and synthesis Procedures

TLm was synthesized as reported previously (Saleh et al., 2007). All reagents were purchased from Sigma-Aldrich (St. Louise, MO, USA) with purity > 99%. Millipore water had conductivity less than 0.05 μS. The pH values of the solutions were adjusted (± 0.2 units) by adding adequate amounts of HCl or NaOH. Cellulose acetate nanofibers (NFs) were prepared by electrospinning. Solution of cellulose acetate was prepared in a solvent mixture of acetone and dimethyl acetamide, with 12% weight of the polymers to the volume of solvent. Then, it was warmed at temperature of 30–35 ºC until solid completely dissolved (Greish et al., 2010).

2.2 Interactions of TLm with cellulose acetate nanofibers (NFs)

The interaction of TLm solids with NFs was established by stirring a mixture of TLm with acetate moieties (in NFs) in aqueous solution with a ~ 1:2 molar ratio under atmospheric pressure, in ethanol with a ~ 1:3 molar ratio under atmospheric pressure, or in aqueous solution with a ~ 2:1 molar ratio under vacuum pressure. The NFs was assumed to contain 39.6% acetate content in calculating the number of moles. The exact number of moles, depending on media, were as follows; For TLm, n = 32 and 21 μmol in water under atmospheric and vacuum condition, respectively, whereas, n = 21 μmol in ethanol under atmospheric condition; For the acetate moieties (in NFs), n = 78 and 10 μmol in water under atmospheric and vacuum condition, respectively, whereas n = 70 in ethanol under atmospheric condition. The pH of the formed suspension was adjusted to 2.1. The TLm/NFs mixture was immersed in water overnight with stirring in darkness under fixed pH. The resulted TLmNFs films were then washed with deionized water and left to dry for 48 hours under ambient air.

2.3 Interactions of TLmNFs with mercuric acetate

TLmNFs films of around 4 mm^2 area prepared either under atmospheric or vacuum conditions were immersed in mercuric acetate solutions in water (4 mL, pH 2) having the following concentration (number of moles of Hg^{2+} ions): 1 mM (4,000,000 µmol), 1 µM (4,000 µmol) and 1 nM (4 µmol), 364 pM (1.5 µmol), 100 pM (0.4 µmol) and 50 pM (0.2 µmol). After shaking the suspension for overnight, the final nanofibers were left to dry completely for 48 hours. The number of moles of TLm in the NFs was kept at 20 µmol.

2.4 Preparation of TLmHg^{2+} complex in solid state

The complex was prepared by grinding method, in which a 1:1 ratio of TLm/mercuric acetate mixture was grounded in solid state using a mortle and pestle for about 20 minutes before washing the new composite by acetone.

2.5 Techniques

2.5.1 Absorption/steady-state fluorescence spectroscopy

The UV–visible absorption spectra were measured on Cary-300 instrument (Agilent, Santa Clara, CA, USA) at room temperature between 200 and 600 nm. Fluorescence spectra measurements were scanned at room temperature between 400 and 700 nm on a Cary-Eclipse fluorimeter. Slit widths were 5 nm for both excitation and emission monochromators, unless otherwise specified. The pH values were recorded using a pH meter (WTW 330i equipped with a WTW SenTix Mic glass electrode). Quartz cuvettes (1.0 cm, 4.0 mL) were used in all spectroscopic measurements and were obtained from Starna Cells Inc. (Atascadero, CA, USA).

2.5.2 Fourier transform infrared (FTIR) spectroscopic measurements

Structural composition of the electrospun fibrous sorbents was carried out using Fourier transform infrared spectrometer (FTIR) (IRPrestige-21, Shimadzu, Tokyo, Japan) in a transmission mode.

2.5.3 Scanning electron microscopy (SEM)

The morphology of the fibrous sorbents was evaluated using a scanning electron microscope (SEM) (Oxford Inca Energy EDS System, Oxford, UK) after gold coating.

2.6 The pH-titration studies

The pH titration by UV–visible absorption and fluorescence spectroscopic method was accomplished by measuring the pH values of about 3 mL-solution in a rectangular quartz cuvette with 1 cm optical path length, and the absorption spectra were then recorded. To adjust pH, microliter volumes from 0.01 and 0.1 M NaOH and HCl solutions were pipetted consecutively to achieve the indicated pH values. The pK_a value was determined finally from fitting the titration data at a selected wavelength to a sigmoidal formula derived from Henderson-Hasselbalch and Beer-Lambert laws. The fitting algorithm was provided by SigmaPlot software (version 6.1; SPSS, Inc., Chicago, IL, USA).

2.7 Time-resolved photoluminescence (TRPL) measurements

The emission decays of TLm in water at different pH values were collected using time-correlated single photon counting (TCSPC) technique implemented on a LifeSpec II spectrometer (Edinburgh Inc., Edinburgh, UK). The excitation was set at 375 nm by using Edinburgh's diode laser with a repetition rate at 50 ns. A red-sensitive high-speed PMT (H5773-04, Hamamatsu, Japan) was used for fluorescence detection. The time resolution of the system is on the order of 30 ps. Emission decays were

collected every 2 nm (unless otherwise specified) over the entire emission spectra of TLm in aqueous solution at certain pH value with a dwell time of 10 s at each wavelength.

2.7.1 Kinetic (global and target) analysis

The data were globally analyzed using publicly available software Glotaran (Snellenburg et al., 2012). In the global analysis, the data measured at all wavelengths are fitted simultaneously by a sum of exponential decays convoluted with the instrument response function, IRF. The lifetimes assumed to be the same across the whole dataset while the pre-exponential factors are left free. The estimated pre-exponential factors/amplitudes represent the estimated spectra, with a lifetime given by the inverse of the rate constant of the exponential decay. The first type of global analysis that was used to analyze presented data utilizes a model of number of parallel decaying components. In this case, the estimated amplitudes at each wavelength are termed decay-associated spectra (DAS). A positive amplitude means a fluorescence decay, whereas a negative amplitude means a rise of fluorescence. A DAS which is positive in one wavelength region and negative in another can be indicative of an excited-state population transfer with the lifetime being associated with that DAS. It is important to note that the DAS do not necessarily represent the spectra of pure physical (chemical) species but rather a mixture of states with similar lifetimes, however in case of parallel decaying species DAS will represent true spectra. A second, more advanced form of the global analysis here uses a kinetic compartmental model. In this case each microscopic rate constant represents the transfer of population of one (excited-state) species into another or the decay to the ground state. The estimated spectra resulting from such an analysis are termed “species associated spectra” (SAS).

2.7.2 Average excited-state lifetime calculation

The data were fitted globally in terms of the multiexponential model. The data were analyzed by the iterative reconvolution method using the instrument's FAST software that utilizes the Levenberg–Marquardt algorithm to minimize χ^2. The contribution of each time constant to the steady-state intensity is given by

$$f_i = \frac{\alpha_i \tau_i}{\sum_j \alpha_j \tau_j} \tag{2.1}$$

where the sum in the denominator is over all the decay times and amplitudes.

The average lifetime at a given wavelength is then given by

$$\bar{\tau} = \sum_i f_i \tau_i \tag{2.2}$$

Chapter 3: Results and Discussion

3.1 Conformational and tautomerization effects on the photoacid behavior of 6-thienyl-substituted lumazine chromophore in aqueous solution

The first part of the present study is aimed at investigating the spectrophysics of TLm in water before mixing it with the NFs to unfold its structure and dynamics under this condition alone. Various cations and anions in the structure of TLm may occur in various tautomeric forms because of protonation at the nitrogen atom sites and deprotonation at the oxo sites. Fortunately, (Afaneh & Schreckenbach, 2014) computationally investigated the most stable prototropic structures of TLm in gas and aqueous phases at the ground state taken into consideration all possible tautomers and conformers, as illustrated in Figure 10. The authors concluded that insertion of thienyl group into the carbon atom at position 6 introduced two different conformers (*cis* and *trans*). The calculated pK_a values of TLm at the ground state for the two subsequent deprotonation equilibria in Figure 10 were also in good agreement with our experimental values (Saleh et al., 2012). Moreover, their calculations for the relative stability of the 13-N and 38-N tautomers (Figure 10) were different than those calculated for Lm tautomers. Accordingly, separating the effects of both tautomeric and rotameric equilibria on ESPT of TLm in aqueous solution are motivated. We have, therefore, measured the TRPL properties of TLm in water solutions at different pH values. Specifically, global and target analyses (Snellenburg et al., 2012) are used to analyze the experimental data and extract the true emission spectra for all possible tautomers and conformers, as illustrated in detail in the Appendix, page 51.

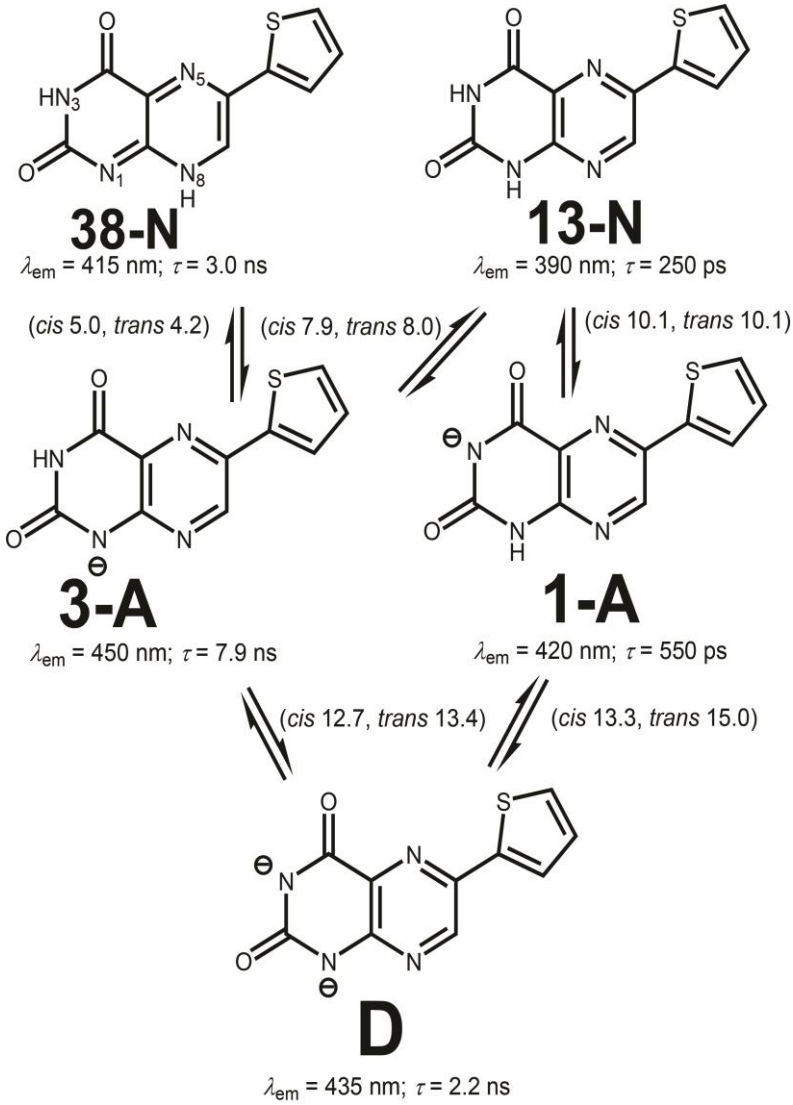

Figure 10: TLm neutral (N), anionic (A), and dianionic (D) tautomers present in aqueous solution. The corresponding calculated acid-dissociation constants (pKa's) at ground states are also included (in parenthesis) as adapted from Afaneh et al., 2014. Only major conformational structures are shown (*cis*). λ_{em} is the emission maximum from the extracted true spectra in the present study and τ is the corresponding fluorescence lifetime for all possible tautomers and conformers (see Figure 8B and Table 1). The numbers in the 38-N, 13-N, 3-A, and 1-A notations are numbers of atom where the hydrogens are attached

Figure 11A shows the steady-state emission spectra of TLm in aqueous solution at different pH values (2, 9, and 12). The sample was excited at 375 nm, which is rationalized by virtue of the absorption spectra of all forms (inset of Figure 11A). The

peaks of the lowest energy absorption bands were at ∼360, 380, and 420 nm for the N, A, and D forms, respectively. One broad band with two maxima at around ∼452 and ∼390 nm are observed at pH 2, which we attribute to the A* and the N* forms of TLm, respectively. At pH of 12, the dianionic D* form emits at around ∼445 nm. In a precedent study, (Saleh et al., 2012) we have measured UV–vis absorption spectra of TLm in several aqueous solutions at different pH values from 3 to 12, from which two subsequent pK_a values for the deprotonation processes were extracted from the titration plots at about 350 and 300 nm; pK_a = 6.84 ± 0.07 and 10.8 ± 0.1, respectively.

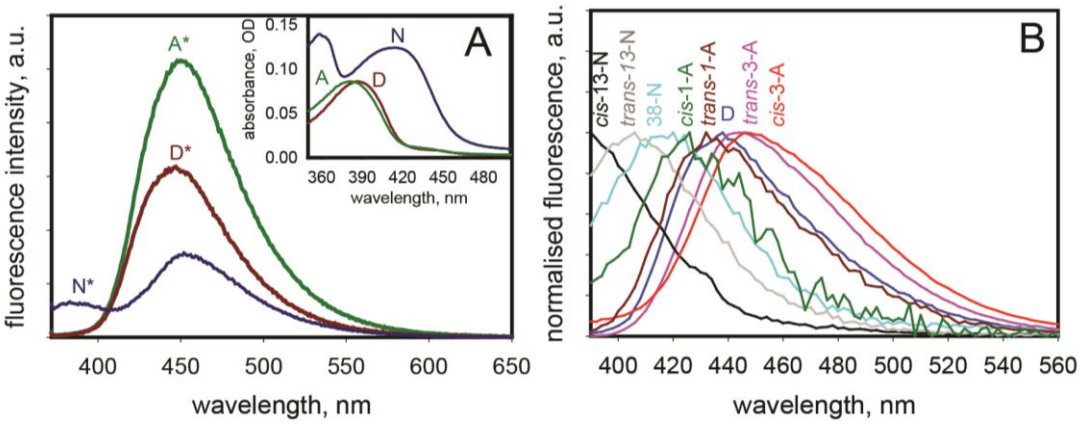

Figure 11: A) Emission spectra of different prototropic species of TLm excited at 375 nm; neutral (N), anionic (A), and dianionic (D) in aqueous solutions at room temperature. The inset shows that all three species can be excited simultaneously at 375 nm. B) The extracted true emission spectra for all possible tautomers and conformers from the global/target analysis

Table 1 and Figure 11B summarize the global and target analysis of TRPL data at different pH values (see page 50 in the Appendix). It transpires that the two species at pH lower than the first pK_a ~ 5-6 (Figure 10), whose emissions appear below 418 nm are attributed to the different neutral tautomers—13-N and 38-N (390 and 405 nm for *cis* and *trans* 13-N and 415 nm for 38-N), whereas the two corresponding anionic forms, whose emission appears above 418 nm, belong to the 3-A and 1-A forms (440

and 450 nm for *trans* and *cis*-3-A and 420 and 430 nm for *cis* and *trans*-1-A). The D form has an emission maximum at 435 nm. The most stable neutral and anionic tautomers and conformers, which were calculated in aqueous solution by (Afaneh & Schreckenbach, 2014), were assumed to give the decay-associated spectra (DAS) amplitudes and the excited-state lifetime values in Table 1. Because strong acids are known to significantly decrease lifetime constants, the two conformers of the minor species 38-N (3.0 ns) were not resolved by our instrument at pH 2–4. However, *cis*-13-N versus *trans*-13-N have emission peak and lifetime of 390 and 250 ps versus 405 and 470 ps, in agreement with theoretical prediction that the *trans* form is red-shifted with respect to the *cis* form (Afaneh & Schreckenbach, 2015). The subsequent formation (with no time evolution) of 3-A and 1-A species from 38-N and 13-N, respectively, are expected at pH above the pK_a values of 5, 8 and 10 (Figure 10), which correspond to pH 4.3, 6.6 and 8.5 (Table 1). The results in the present work highlight the true emission spectra and excited-state lifetime for each conformer, not only tautomer of TLm; and for both anions. Noticeably, both the *trans* and *cis*-3-A forms have longer excited-state lifetime values than their counterparts *trans* and *cis*-1-A forms (7.3 and 7.9 ns versus 3.7 ns and 550 ps, respectively), thus dominating the steady emission spectra at about 452 nm (Figure 8A). It is worth to mention that only the decay of the short-wavelength species *cis*-13-N (250 ps) and *cis*-1-A (550 ps) begins to fit the rise time of anionic species *cis*-3-A (7.9 ns), and D (2.2 ns) forms, respectively, with a concomitant increase in the DAS's negative amplitude (see Part S1 in the Appendix, page 73 and 55).

In their article, Presiado et al. (2010). reported the emission properties of Lm using steady-state and TRPL techniques, concluding that the deprotonation time of

neutral Lm to form the corresponding anion is about ~35 ps at the excited state. They interpreted the photophysical properties of Lm at different pH values taken into consideration the various tautomeric species at both the ground and excited states. The authors also concluded that the neutral form of Lm is an irreversible mild photoacid, and that only one of the two tautomer has ESPT activity (Simkovitch & Huppert, 2017). We also conclude that ESPT (with a deprotonation time of ~350 ps) occurs only from *cis* forms, confirming the significant role played by confirmation, not only tautomerization. The conformation effects on the emission properties of TLm, which distinguish the present work, have also been theoretically addressed. The emission maxima of TLm was calculated to be 439 nm (for *cis*-TLm) and 441 nm (for *trans*-TLm) in agreement with our experimental results (Afaneh & Schreckenbach, 2014).

Table 1:The extracted excited-state lifetimes in nanoseconds of all tautomers and conformers of TLm in water from the global/target analysis of TRPL data at different pH values

	13-N		38-N	3-A		1-A		D
	cis	trans		trans	cis	cis	trans	
λ_{em} /nm	390 nm	405 nm	415 nm	440 nm	450 nm	420 nm	430 nm	435 nm
pH 1.8	0.232 ns [0.565 ns]	ND	ND		3.1 ns [1.3 ns]			
pH 2.4	0.254 ns [0.918 ns]	ND	ND		4.7 ns [0.933 ns]			
pH 2.8	0.253 ns [0.937 ns]	ND	ND		5.9 ns [1.0 ns]			
pH 3.4	0.257 ns [0.925 ns]	ND	ND		6.5 ns [0.974 ns]			
pH 3.9	0.259 ns [1.0 ns]	ND	ND		6.7 ns [1.0 ns]			
pH 4.3[a]	ND	0.387 ns	2.7 ns	7.3 ns				
pH 4.5	ND	0.427 ns	3.0 ns	7.4 ns				
pH 5.6	ND	0.298 ns	2.5 ns	7.3 ns				

Table 1: The extracted excited-state lifetimes in nanoseconds of all tautomers and conformers of TLm in water from the global/target analysis of TRPL data at different pH values (continued)

	13-N		38-N	3-A			1-A		D
	cis	trans		trans	cis		cis	trans	
λ_{em} /nm	390 nm	405 nm	415 nm	440 nm	450 nm		420 nm	430 nm	435 nm
pH 6.0	ND	0.394 ns	3.0 ns	7.4 ns					
pH 6.6[b]	ND	0.470 ns			7.6 ns			3.7 ns[d]	
pH 7.1	ND	0.478 ns			7.6 ns			3.9 ns[d]	
pH 7.6	ND	0.512 ns			7.2 ns			3.6 ns[d]	
pH 8.5[c]	ND	ND			7.6 ns		0.559 ns	3.2 ns	
pH 8.9	ND	ND			7.6 ns		0.532 ns	2.6 ns	
pH 9.5	ND	ND			7.6 ns		0.620 ns	2.4 ns	
pH 10.6					7.5 ns		0.184 ps	ND	2.1 ns
pH 11.0					7.8 ns		0.198 ns	ND	2.1 ns
pH 11.5					7.5 ns		0.186 ns	ND	2.1 ns
pH 11.8					6.8 ns		0.146 ns	ND	2.1 ns

Species whose lifetimes are displayed in bold fonts were formed by ESPT. Minor species due to nonexponential behavior are shown in parentheses. Also, the *cis*-13-N

is blue-shifted with respect to *trans*-13-N as predicted by theory (Afaneh & Schreckenbach, 2015). ND means the species were quenched by either basic or acidic media, consequently their excited-lifetimes were not detected due to the low time-resolution of our instrument. [a]pH around the pK_a associated with the protonation-deprotonation equilibrium between 38-N and 3-A (Figure 10). [b]pH around the pK_a associated with the protonation-deprotonation equilibrium between 13-N and 3-A (Figure 10). [c]pH around the pK_a associated with the protonation-deprotonation equilibrium between 13-N and 1-A (Figure 10). [d]Species *trans*-1-A appeared with low amplitudes in the pH range from 6.6 to 8.5.

In summary, we have characterized the photophysical properties of TLm compound in water. Our results explain its ESPT behaviors as a photoacid using quantitative TRPL tools and considering the excited state population kinetics of its tautomers and conformers. All neutral and anionic forms of TLm have overlapped absorption and emission, yet their different acidities were best exploited in the present work to separate the spectra of all possible tautomers and conformers. Comprehensive, global and target kinetic analysis of excited-state population transfer were performed, in which the true emission spectra and excited-state lifetimes of all prototropic, tautomers and conformers were best sorted out in the pH range from 2 to 12. The experimental results support the premise that both conformers (*cis*-13-N and *cis*-1-A forms) are related to the ESPT process. Thus, photoprotolytic processes are strongly influenced by both tautomerization and conformation effects.

3.2 Spectrophysics of TLm in cellulose acetate nanofibers (confinement vs. polarity effects)

In the second part of the present work, the steady and TRPL spectral properties (position, intensity and excited-state lifetime) of TLm upon stirring with NFs in aqueous solution were monitored. Taken into consideration the spectrophyical properties of TLm in water, as described above, we have opted to stir the TLm with NFs under pH of 2, at which the neutral TLm species should persist. The ESPT process, which produces mono-anionic species, is also expected to occur at this pH. The NFs was then filtered out and used for analyses by SEM and EDS (see the Experimental Section). The EDS confirms the presence of N and S in the structure of TLMNFs (Figure 12).

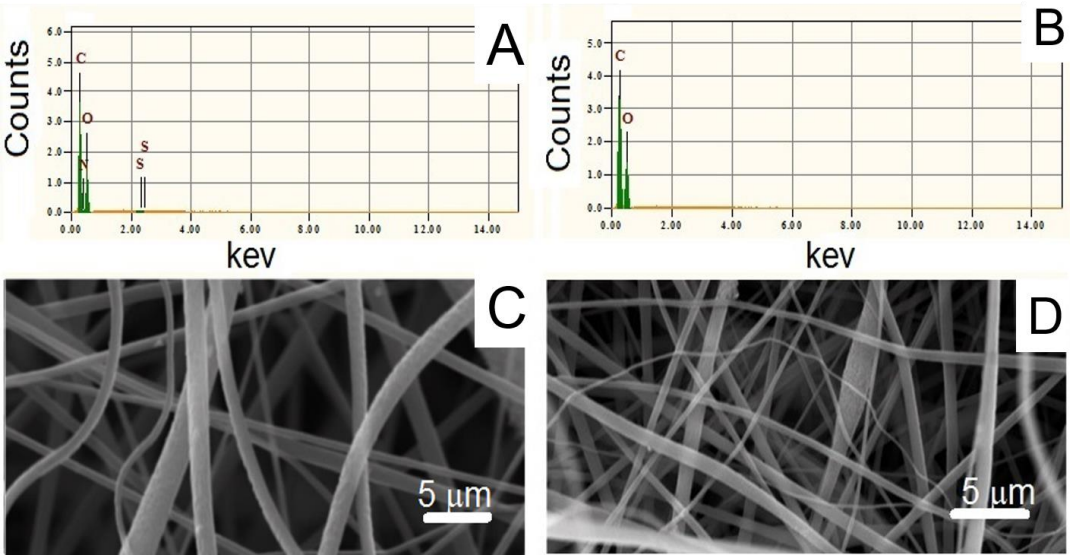

Figure 12: SEM images for cellulose acetate nanofibers (NFs) with (C) and without (D) stirring in aqueous solution of TLm under atmospheric conditions. The EDS spectra in ethanol for (A) TLmNFs(atm) and (B) NFs are also shown on the top of each image

The steady-state fluorescence spectra in Figure 10A clearly confirm that an interaction has occurred between TLm solid and NFs, leading to a shift in the

emission maximum from 420 nm to 441 nm in the case of the TLmNFs, which was prepared under atmospheric condition, whereas a shift from 420 nm to 407 nm was observed for the film, which was prepared under vacuum condition. The blue shift of the emission maximum and the enhancement of its intensity and excited-state lifetime (see below) can be best explained by polarity effects (non-radiative rate law). This indicates that TLm molecules when mixed with NFs under vacuum conditions experience a confined and non-polar environment (away from acetate moiety) within the pores of NFs (Figure 9). Contrarily, the TLm solids when mixed with NFs under atmospheric condition remain attached to the exterior part of the fibres (Figure 9). The NFs alone is non-emissive.

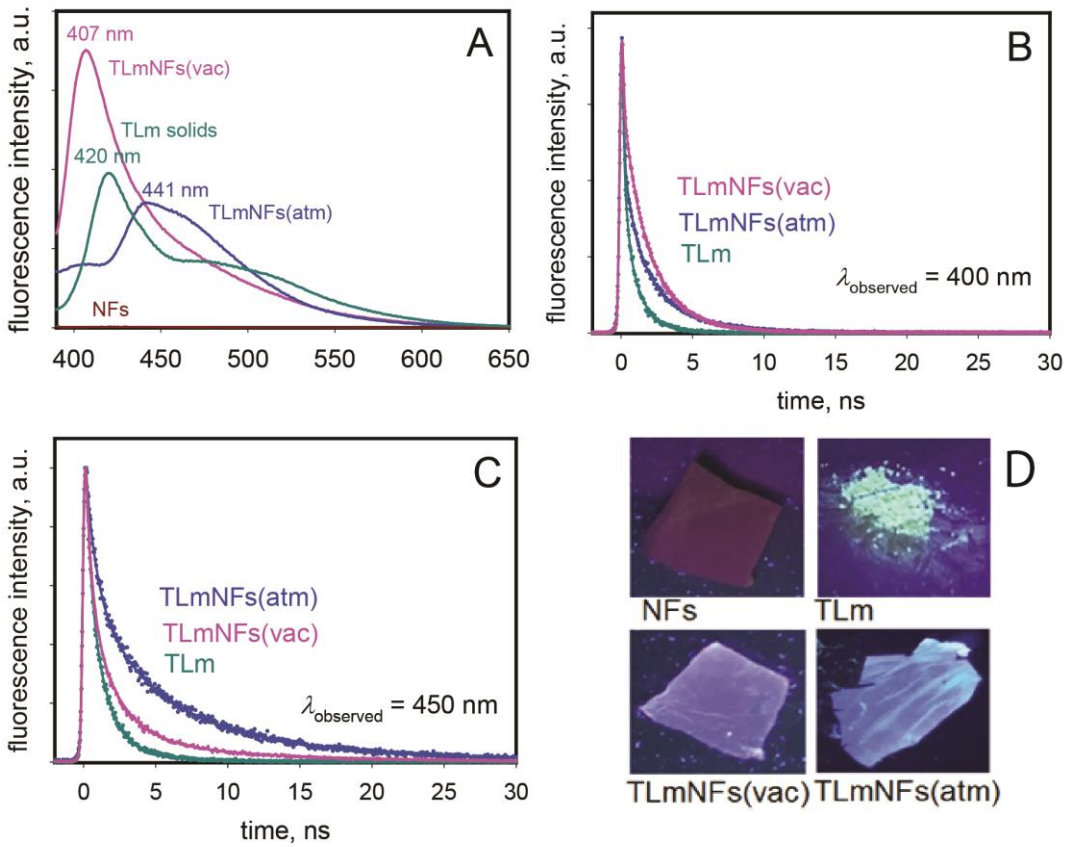

Figure 13: Photoluminescence (PL) spectra in the solid state for TLm before and after stirring with NFs under atmospheric (TLmNFs(atm)) and vacuum pressure (TLmNFs(vac)) at room temperature (A); and their fluorescence decay traces monitored at 400 nm (B) and 450 nm (C) after 375 nm excitation. The real photos for all solids are shown in D. Colored dots represent the raw data and colored solid lines correspond to the fits derived from the global analysis, see Figure S19, S20 and S21 in the Appendix, page 78, 79 and 80

By analogy to the results in solution, we have analysed the emission decays measured for solid TLm, TLmNFs(vac), and TLmNFs(atm) at different emission wavelengths across the entire emission spectra (Figures S19, S20 and S21 in the Appendix, page 78, 79 and 80). It transpires that the data are best fitted utilizing the global method, which assumes parallel unimoelcular kinetic model. This confirms the lack of ESPT process inside the NFs, which agrees with Huppert recent findings on carbohydrates' surface for similar Lm photoacids (Amdursky et al., 2014; Simkovitch

& Huppert, 2015a, 2015b). The authors attributed their results to the lack of water molecule inside the NFs in the presence of Lm photoacids. In contract to data in solution, each DAS peak in Table 2 appears to be associated with a distinct structure of TLm (in NFs) because we could not fit all data simultaneously. Thus, interpretation of each emission maximum and the associated lifetime constant in Table 2 requires a pre-knowledge on the solid-state structure of TLm and TLmNFs. This needs X-ray crystallographic studies, which is not available to us. However, it transpires from the trend in the data in Table 2 that distinct electronic states are observed depending on their emission maxima—400 nm (blue-shifted band) and 450 nm (red-shifted band)—and excited-state lifetime constants. While one specie emits at 400 nm, the species emit at the red side can be further sorted out as short-lived, long-lived, and very-longed species. In Figures 13 (B,C), the monitored emission decays at 400 for TLm solids before and after stirring with NFs films confirmed a 2-fold increase in the excited-state lifetime constants (2.2 versus 1.1 ns and 1.9 versus 1.1 ns for TLmNFs(atm) and TLmNFs(vac), respectively, (Table 2). The enhanced excited-state lifetime reflects a major role played by the confinement/rigidity factor, which restricts the movement of TLm inside the fibres. It must be noticed that the very-long lived species appear only under atmospheric condition at 450 nm (Figure 13C), thus contribute to the increased average excited-state lifetime constants monitored at 450 nm (Table S1 in the Appendix, page 88) with the addition of NFs (compare 38 versus 1.2 ns under atmospheric condition to 3.2 versus 1.2 ns under vacuum). Overall, both steady and TRPL measurements confirmed the interactions of TLm with NFs (Table 2).

Table 2: The extracted excited-state lifetimes in nanoseconds of all species of TLm in solid state with and without the NFs from the global analysis of TRPL data. Range of DAS maxima is shown in brackets. Average excited-state lifetime at 450 nm was calculated

	Blue-shifted specie (~ 400 ± 20 nm)	Red-shifted species (~ 450 ± 20 nm)			Average lifetime at 450 nm
		Short-lived	Long-lived	Very long-lived	
TLm	1.1 ns	0.223 ns	3.8 ns		1.2 ns
TLmNFs(vac)	1.9 ns	0.389 ns	9.6 ns		3.2 ns
TLmNFs(vac)Hg^{2+}(5:1)	1.9 ns	0.857 ns	8.1 ns		3.5 ns
TLmNFs(vac)Hg^{2+}(1:200)	1.9 ns	0.444 ns	8.0 ns		3.1 ns
TLmNFs(vac)Hg^{2+}(1:200,000)	1.9 ns	0.467 ns	7.5 ns		3.8 ns
TLmNFs(atm)	2.2 ns	0.557 ns	6.2 ns	15.9 ns	38 ns[a]
TLmNFs(atm)Hg^{2+}(5:1)	2.0 ns	0.497 ns	6.3 ns	80.5 ns	2.9 ns[a]
TLmNFs(atm)Hg^{2+}(1:200)	2.2 ns	0.594 ns	6.6 ns	38.1 ns	3.0 ns
TLmNFs(atm)Hg^{2+}(1:200,000)	1.9 ns	0.436 ns	5.9 ns	36.3 ns	3.0 ns
TLM-Hg^{2+} complex	1.0 ns	0.169 ps	3.7 ns		1.0 ns

[a]Values are presented as mean ± standard deviation, see Tables S1, S2, and S3 in the Appendix in pages 88, 90 and 91.

3.3 Fluorescence detection for mercuric acetate in solid state and nanofibers (static vs. dynamic quenching)

In the third part of the present study, we have tested the effects of adding mercuric acetate on the emission properties in the solid state of TLm (in NFs). The fluorescent sensing of TLm for Hg^{2+} ions in aqueous solution has already been reported experimentally by one of us (Na'il Saleh, 2009) and theoretically by others (Afaneh & Schreckenbach, 2015), from which it was concluded that the coordination with mercury ion occurs through the atoms sulphur, oxygen, and nitrogen with a 2-to-1 stoichiometry between ligand and metal (Afaneh & Schreckenbach, 2015). The mechanism of fluorescence quenching was also explained in detail through the molecular orbital calculations. (Afaneh & Schreckenbach, 2015) One expects two possible limiting cases for the fluorescence quenching—dynamic and static (Valeur & Berberan-Santos, 2013). In the dynamic case, the observed fluorescence lifetime of TLm decreases with the increase in the concentration of the quencher because of the opening on a new deactivation channel, whereas the in the static fluorescence quenching the observed lifetime is unaffected because the formed non-fluorescent associated complex in the ground state only decreases the number of emitters without an associated quenching molecule.

The PL and TRPL (Table 2 and Figure 14) were measured in solid state for TLmNFs(atm) and TLmNFs(vac) at different TLm/Hg^{2+} molar ratios—5:1, 1:200, and 1:200,000. The number of moles for TLm was 20 µmol. The PL spectra appear not to correlate with the moles of the added ions under either condition (Figures 14A and 14C) because of the involvement of multiple species, which confirms that steady-state data are not an absolute measure and are unreliable for creating a standard calibration

sensing curve in the solid state (Valeur & Berberan-Santos, 2013). Not to mention the intensity is also affected by the position of laser exposure to the measured film.

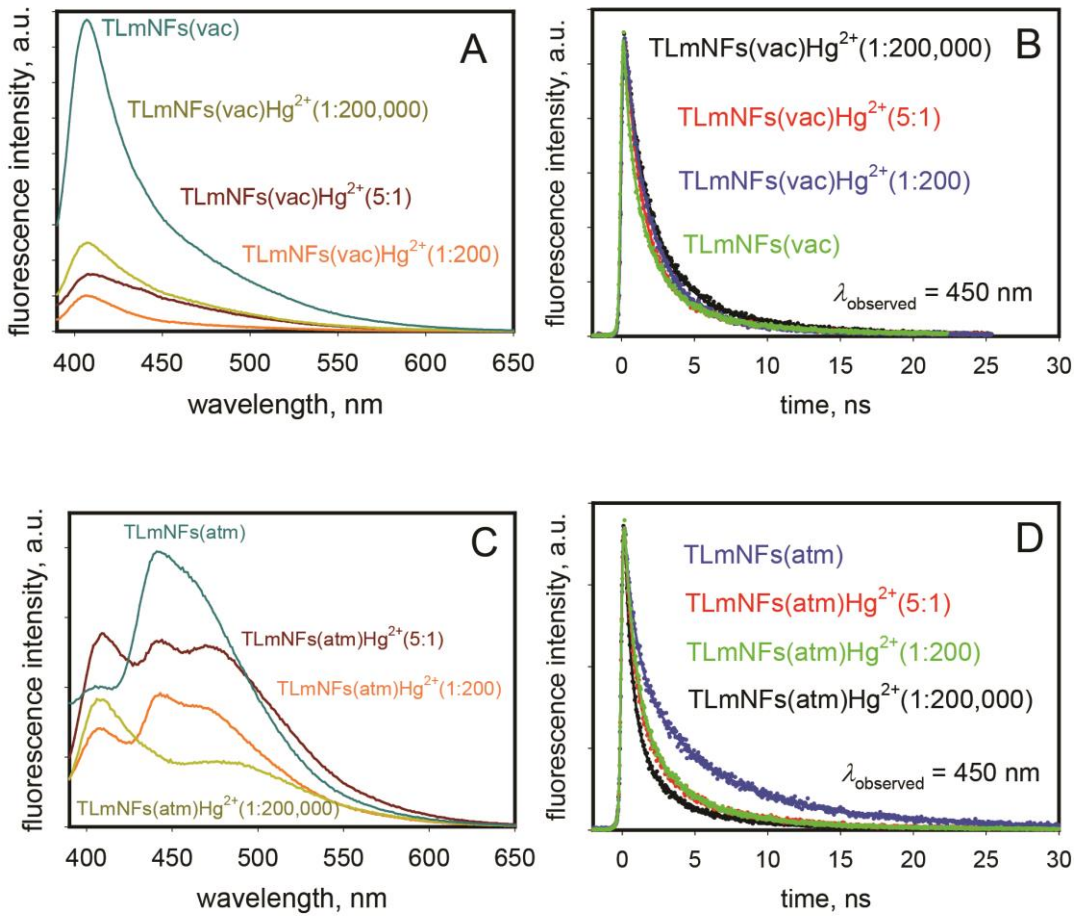

Figure 14: Photoluminescence (PL) spectra (A and C) of solid TLmNFs(vac) and TLmNFs(atm) before and after addition of mercuric ions at various TLm/Hg2+ molar ratios (as indicated in the graph), and fluorescence decay traces (B and D) of the same solid films monitored at 450 nm after excitation at 375 nm. The number of moles for TLm was 20 µmol. Colored dots represent the raw data and colored solid lines correspond to the fits derived from the global analysis, see Figures S22, S23, S24, S25, S26, and S27 in the Appendix in pages 81, 82, 83, 84, 85 and 86

However, adding one Hg^{2+} ion to 5 molecules of TLm is enough to decrease the average excited-state lifetime monitored at 450 nm from 38 ns to 2.9 ns (Table 2) for the case of NFs, which was prepared under atmospheric, not vacuum conditions (Figure 14D versus Figure 11B). We have, therefore, measured the PL and TRPL in

solid state for TLmNFs(atm) with additional TLm/Hg^{2+} molar ratios—100:1, 50:1, and 13:1—to clarify the mechanism of fluorescence quenching by mercuric ions and determine the linear sensing range (Table S1, S2, and S3 in the Appendix in pages 88, 90 and 91). The results in Figure 12 confirms that the average excited-state lifetime monitored at three wavelength: 430, 450 and 470 nm and presented as mean ± standard deviation (Tables S1, S3, and S3 in the Appendix, pages 88, 90 and 91), linearly correlate (R = 0.995, slope was 20 $mol^{-1}s^{-1}$) with the number of moles of Hg^{2+} ions (Figure 12A) up to 50:1 TLm/Hg^{2+} ratio. A linear plot (R = 0.995, slope was 17 $mol^{-1}s^{-1}$) between the excited-state lifetime associated with the very-longed lived species (Tables S1 in the Appendix in page 88), was also established (Figure 12B), confirming the sensitivity of this component to mercury ion. Indeed, the excited-state lifetime values associated with the DAS peak at 450 nm, not 400 nm (compare Figure 11D with Figure S28 in the Appendix, page 86) are more sensitive to mercuric concentrations.

Putting all together, the calibration curve constructed from excited-state lifetime data in the solid state utilizing TRPL measurements is, therefore, more accurate and quantitative, when compared to stationary data. The decrease in the excited-state lifetime value at 450 nm under atmospheric condition can be related to a predominant dynamic quenching, whereas a pure static mechanism governs the quenching under vacuum condition. The results, thus, provide accurate sensing data in the solid state with high sensitivity and selectivity (sub micromoles). Thus, the present results have a higher economic and environmental value and a wider adaptability to domestic users when compared to results in solution.

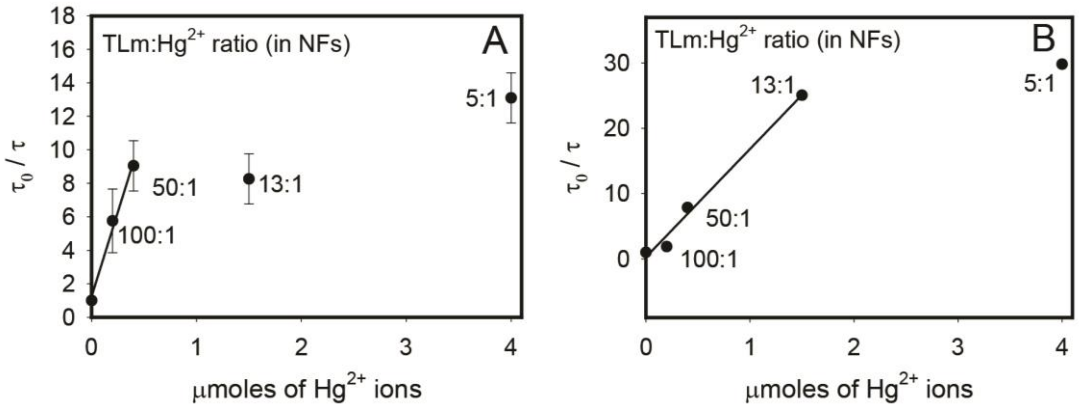

Figure 15: The dependence of the average (A) and the longest (B) excited-state lifetimes (τ) monitored at 450 nm (Table 2) for TLmNFs(atm) on the number of added moles of Hg2+. TLm/Hg2+ (in NFs) ratios are indicated in the figure. τ0 = unquenched lifetime. The number of moles for TLm was 20 μmol

3.4 Complex formation of TLm with mercuric acetate in the solid state

The FT-IR measurements (Figure S43 in the Supporting Information in page 105) for the prepared TLm-Hg^{2+} complex in solid state has confirmed the formation of the complex and the possible occurrence of static quenching inside NFs. The peaks associated with stretching frequencies of carbonyl and imine bonds were shifted to lower wavenumbers with the addition of mercuric acetate. In addition, no change in the excited-state lifetime constants, which were either measured at 400 nm or 450 nm, were observed with the addition of mercuric ions (1.1 versus 1.0 ns and 1.2 versus 1.0 ns, respectively, in Table 2 and Figures S19 and S29 in the Appendix-page 78 and 87. Moreover, the appearance of isosobestic points in the UV–vis absorption spectra upon titrating TLm with Hg^{2+} in aqueous solution (Figure S44 in the Supporting Information in page 106) indicate the formation of non-fluorescent complex at the ground state in the solid state and supports the static quenching observed above for the reaction of TLm with mercuric acetate inside the pores of NFs under vacuum condition (Figure 7).

Chapter 4: Conclusion

TRPL measurements have unfolded the confirmation effects on the ESPT process in the excited state of TLm in water. Only the *cis* conformers are involved in the ESPT process. The results, also, revealed, the mechanism of fluorescence quenching by mercuric ions of TLm fluorophore inside NFs in the solid state. Static quenching has occurred when TLm was loaded in NFs under vacuum, not atmospheric pressure. Despites the large number of reported sensors for mercuric ions in solid and solution, the results in the present work highlight the advantage of TRPL over steady-state emission methods for detection of picomoles of Hg^{2+} ions in the solid state.

.

References

Afaneh, A. T., & Schreckenbach, G. (2014). Conformation/Tautomerization effect on the pKa values of lumazine and 6-thienyllumazine. *Journal of Physical Organic Chemistry*, *27*(8), 690–700.

Afaneh, A. T., & Schreckenbach, G. (2015). Fluorescence Enhancement/Quenching Based on Metal Orbital Control: Computational Studies of a 6-Thienyllumazine-Based Mercury Sensor. *The Journal of Physical Chemistry A*, *119*(29), 8106–8116.

Agmon, N. (2005). Elementary Steps in Excited-State Proton Transfer. *The Journal of Physical Chemistry A*, *109*(1), 13–35.

Amdursky, N., Simkovitch, R., & Huppert, D. (2014). Excited-State Proton Transfer of Photoacids Adsorbed on Biomaterials. *The Journal of Physical Chemistry B*, *118*(48), 13859–13869.

Davis, B. W., Niamnont, N., Dillon, R., Bardeen, C. J., Sukwattanasinitt, M., & Cheng, Q. (2011). FRET Detection of Proteins Using Fluorescently Doped Electrospun Nanofibers and Pattern Recognition. *Langmuir*, *27*(10), 6401–6408.

Denofrio, M. P., Thomas, A. H., Braun, A. M., Oliveros, E., & Lorente, C. (2008). Photochemical and photophysical properties of lumazine in aqueous solutions. *Journal of Photochemistry and Photobiology A: Chemistry*, *200*(2), 282–286.

Engelborghs, Y., & Visser, A. J. W. G. (2016). *Fluorescence Spectroscopy and Microscopy Methods and Protocols*. Springer.

Förster, T. (1950). Die pH-Abhängigkeit der Fluoreszenz von Naphthalinderivaten. *Zeitschrift Für Elektrochemie Und Angewandte Physikalische Chemie*, *54*(7), 531–535.

Green, O., Gajst, O., Simkovitch, R., Shabat, D., & Huppert, D. (2017). Chloro benzoate cyanine picolinium photoacid excited-state proton transfer to water. *Journal of Photochemistry and Photobiology A: Chemistry*, *349*(Supplement C), 230–237.

Greish, Y. E., Meetani, M. A., Al Matroushi, E. A., & Shamsi, B. A. (2010). Effects of thermal and chemical treatments on the structural stability of cellulose acetate nanofibers. *Carbohydrate Polymers*, *82*(3), 569–577.

Halbritter, T., Kaiser, C., Wachtveitl, J., & Heckel, A. (2017). Pyridine–Spiropyran Derivative as a Persistent, Reversible Photoacid in Water. *The Journal of Organic Chemistry*, *82*(15), 8040–8047.

Hsieh, C.-C., Jiang, C.-M., & Chou, P.-T. (2010). Recent experimental advances on excited-state intramolecular proton coupled electron transfer reaction. *ACS Publications*, *43*, 1364–1374.

Ireland, J. F., & Wyatt, P. A. H. (1976). Acid-Base Properties of Electronically Excited States of Organic Molecules. In V. Gold (Ed.), *Advances in Physical Organic Chemistry* (Vol. 12, pp. 131–221). Retrieved from

Kaur, M., Cho, M. J., & Choi, D. H. (2016). A phenothiazine-based “naked-eye” fluorescent probe for the dual detection of Hg2+ and Cu2+: Application as a solid state sensor. *Dyes and Pigments*, *125*, 1–7.

Klein, R., & Tatischeff, I. (1987). TAUTOMERISM AND FLUORESCENCE OF LUMAZINE. *Photochemistry and Photobiology*, *45*(1), 55–65.

Klemm, D., Kramer, F., Moritz, S., Lindström, T., Ankerfors, M., Gray, D., & Dorris, A. (2011). Nanocelluloses: A New Family of Nature-Based Materials. *Angewandte Chemie International Edition*, *50*(24), 5438–5466.

Kundu, P. K., Samanta, D., Leizrowice, R., Margulis, B., Zhao, H., Börner, M., … Klajn, R. (2015). Light-controlled self-assembly of non-photoresponsive nanoparticles. *Nature Chemistry*, *7*, 646–652.

Lakowicz, J. R. (2006). *Principles of Fluorescence Spectroscopy* (Third Edition). Springer.

Li, J., Liu, Z., Tan, C., Guo, X., Wang, L., Sancar, A., & Zhong, D. (2010). Dynamics and mechanism of repair of ultraviolet-induced (6-4) photoproduct by photolyase. *Nature*, *466*(7308), 887–890. Retrieved from ProQuest Central. (746435520; 20657578)

Lichtman, J. W., & Conchello, J.-A. (2005). Fluorescence microscopy. *Nature Methods*, *2*, 910–919.

Mahato, P., Saha, S., Das, P., Agarwalla, H., & Das, A. (2014). An overview of the recent developments on Hg2+ recognition. *RSC Adv.*, *4*(68), 36140–36174.

Mohammed, O. F., Pines, D., Dreyer, J., Pines, E., & Nibbering, E. T. J. (2005). Sequential Proton Transfer Through Water Bridges in Acid-Base Reactions. *Science*, *310*(5745), 83–86.

Mondal, S. K., Sahu, K., Sen, P., Roy, D., Ghosh, S., & Bhattacharyya, K. (2005). Excited state proton transfer of pyranine in a γ-cyclodextrin cavity. *Chemical Physics Letters*, *412*(1), 228–234.

Moyon, N. S., Gashnga, P. M., Phukan, S., & Mitra, S. (2013). Specific solvent effect on lumazine photophysics: A combined fluorescence and intrinsic reaction coordinate analysis. *Chemical Physics*, *421*, 22–31.

Nguyen, L. T. H., Chen, S., Elumalai, N. K., Prabhakaran, M. P., Zong, Y., Vijila, C., … Ramakrishna, S. (2013). Biological, Chemical, and Electronic Applications of Nanofibers. *Macromolecular Materials and Engineering*, *298*(8), 822–867.

Ohkawa, K. (2015). Nanofibers of Cellulose and Its Derivatives Fabricated Using Direct Electrospinning. *Molecules*, *20*(5), 9139–9154.

Omollo, E., Zhang, C., Mwasiagi, J. I., & Ncube, S. (2014). Electrospinning cellulose acetate nanofibers and a study of their possible use in high-efficiency filtration. *Journal of Industrial Textiles*, 45(5), 716–729.

Owens, P. (2009). *Time-Resolved Fluorescence Spectroscopy of Crude Petroleum Oils* (Doctoral dissertation).

Presiado, I., Erez, Y., Gepshtein, R., & Huppert, D. (2010). Excited-State Intermolecular Proton Transfer of Lumazine. *The Journal of Physical Chemistry C*, *114*(8), 3634–3640.

Saleh, N., Graham, J., Afaneh, A., Al-Soud, Y. A., Schreckenbach, G., & Esmadi, F. T. (2012). Pteridine-based fluorescent pH sensors designed for physiological applications. *Journal of Photochemistry and Photobiology A: Chemistry*, *247*, 63–73.

Saleh, N., Rawashdeh, A.-M. M., Yousef, Y. A., & Al-Soud, Y. A. (2007). Structural characterization of new Cd2+ fluorescent sensor based on lumazine ligand: AM1 and ab initio studies. *Spectrochimica Acta Part A: Molecular and Biomolecular Spectroscopy*, *68*(3), 728–733.

Saleh, N., (2009). Luminescent sensor for Cd2+, Hg2+ and Ag+ in water based on a sulphur-containing receptor: quantitative binding–softness relationship. *Luminescence*, *24*(1), 30–34.

Serdiuk, I. E., & Roshal, A. D. (2017). Exploring double proton transfer: A review on photochemical features of compounds with two proton-transfer sites. *Dyes and Pigments*, *138*, 223–244.

Sigel, H. (2004). *Metal Ions in Biological Systems: Volume 42: Metal Complexes in Tumor Diagnosis and as Anticancer Agents*. CRC Press.

Simkovitch, R., & Huppert, D. (2015a). Excited-State Proton Transfer of Weak Photoacids Adsorbed on Biomaterials: 8-Hydroxy-1,3,6-pyrenetrisulfonate on Chitin and Cellulose. *The Journal of Physical Chemistry A*, *119*(10), 1973–1982.

Simkovitch, R., & Huppert, D. (2015b). Excited-State Proton Transfer of Weak Photoacids Adsorbed on Biomaterials: Proton Transfer on Starch. *The Journal of Physical Chemistry B*, *119*(30), 9795–9804.

Simkovitch, R., & Huppert, D. (2017). Photoprotolytic Processes of Lumazine. *The Journal of Physical Chemistry B*, *121*(1), 129–142.

Snellenburg, J. J., Laptenok, S., Seger, R., Mullen, K. M., & Van Stokkum, I. H. M. (2012). Glotaran: A Java-based graphical user interface for the R package TIMP. *Journal of Statistical Software*, 49(3).

Stevens, M. J., Hadfield, R. H., Schwall, R. E., Nam, S. W., Mirin, R. P., & Gupta, J. A. (2006). Fast lifetime measurements of infrared emitters using a low-jitter superconducting single-photon detector. *Applied Physics Letters*, *89*(3), 31109.

Sun, X., Liu, Y., Shaw, G., Carrier, A., Dey, S., Zhao, J., & Lei, Y. (2015). Fundamental Study of Electrospun Pyrene–Polyethersulfone Nanofibers Using Mixed Solvents for Sensitive and Selective Explosives Detection in Aqueous Solution. *ACS Applied Materials & Interfaces*, *7*(24), 13189–13197.

Valeur, B., & Berberan-Santos, M. N. (2013). *Molecular fluorescence: principles and applications* (2. ed). Weinheim: Wiley-VCH.

Wang, M., Meng, G., Huang, Q., & Qian, Y. (2012). Electrospun 1,4-DHAQ-Doped Cellulose Nanofiber Films for Reusable Fluorescence Detection of Trace Cu2+ and Further for Cr3+. *Environmental Science & Technology*, *46*(1), 367–373.

Wu, J., Wang, N., Zhao, Y., & Jiang, L. (2013). Electrospinning of multilevel structured functional micro-/nanofibers and their applications. *Royal Society of Chemistry*, *1*, 7290–7305.

Wang, X., Drew, C., Lee, S-H., Senecal, K., Kumar, J., Samuenlson, L. (2002). Electrospun Nanofibrous Membranes for Highly Sensitive Optical Sensors. *Nano Lett.*, *2*, 1273–1275.

List of Publications

Alzard, R. H., Bufaroosha, M. S., Al-Shamsi, N., Sohail, A., Al-Dubaili, N., Salem, A. A., ... & Saleh, N. I. (2019). Solubilization of Pyridone-Based Fluorescent Tag by Complexation in Cucurbit [7] uril. *ACS Omega*, *4*(1), 953-960.

Cuba, M., Al-Shamsi, N., Qamhieh, N., Saleh, N. I., Najar, A., Kumar, R. T., & Mahmoud, S. T. (2018). Synthesis and characterization of hybrid organic–inorganic nanocomposite for photocatalytic application. *Applied Physics A*, *124*(10), 672.

Al-Rawashdeh, N. A., Alshamsi, A. S., Hisaindee, S., Graham, J., & Al Shamisi, N. (2017). The efficiency of eco-friendly Schiff bases as corrosion inhibitor for stainless steel in hydrochloric acid solution. *Int. J. Electrochem. Sci*, *12*, 8535.

Appendix

Part S1. Global and target analysis of TRPL data at different pH values.

In the following paragraphs, the TRPL spectra of TLm in water were grouped into five groups of datasets depending on the pH range to shed more insights into the exact structures and dynamics of all the contributed species to the prototropic processes. The data were specifically analyzed by global and target methods (see Experimental Section) to extract the true emission spectra for all possible tautomers and conformers.

S1.1 TRPL of TLm in water (pH 2–4).

In this group, the average excited-state lifetime is increasing with the increase of pH values. Representative traces measured at 450 nm are shown in Figure S1. To fit properly TRPL data of TLm aqueous solutions in this pH range, at least 3 components are needed, as illustrated in Figure S2. While the first two lifetimes are not changing with pH, the last one is increasing its lifetime.

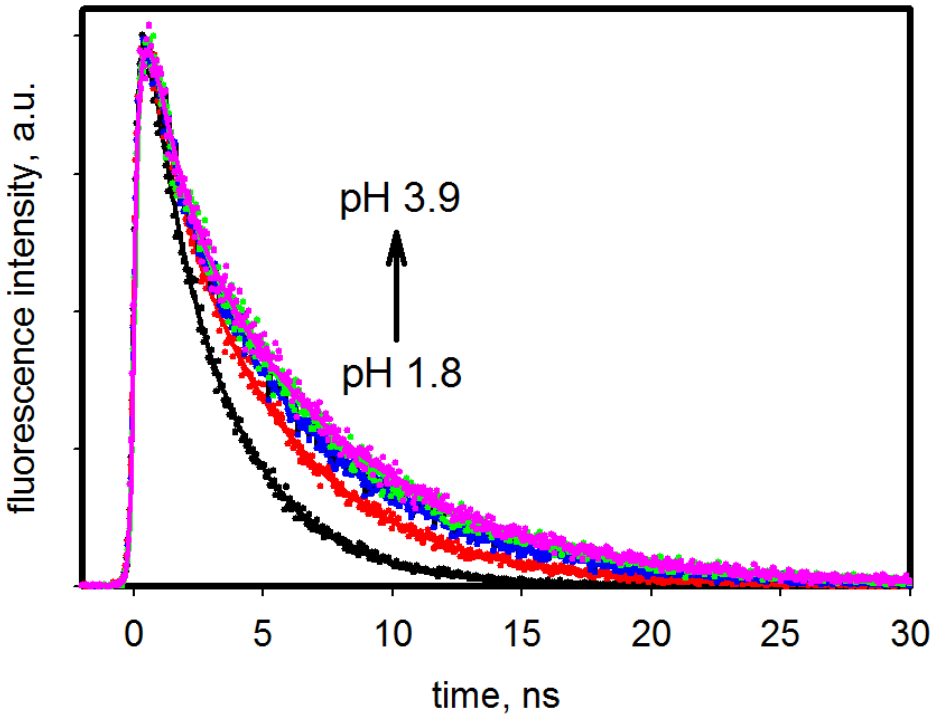

Figure S1**.** Fluorescence decay traces of TLm in water monitored at 450 nm after 375 nm excitation in the pH range from 2 to 4. The colored dots represent the raw data and the solid lines with the same colors correspond to the fits derived from the global/target analysis

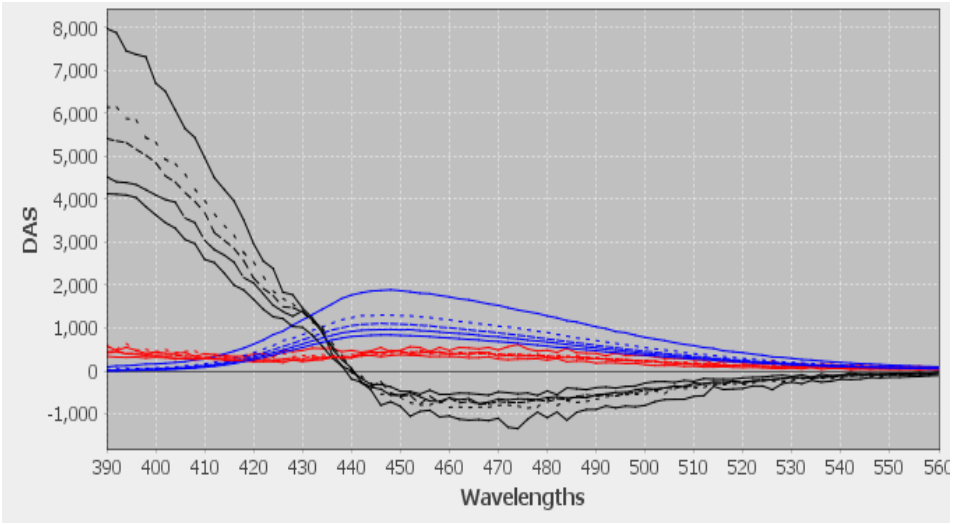

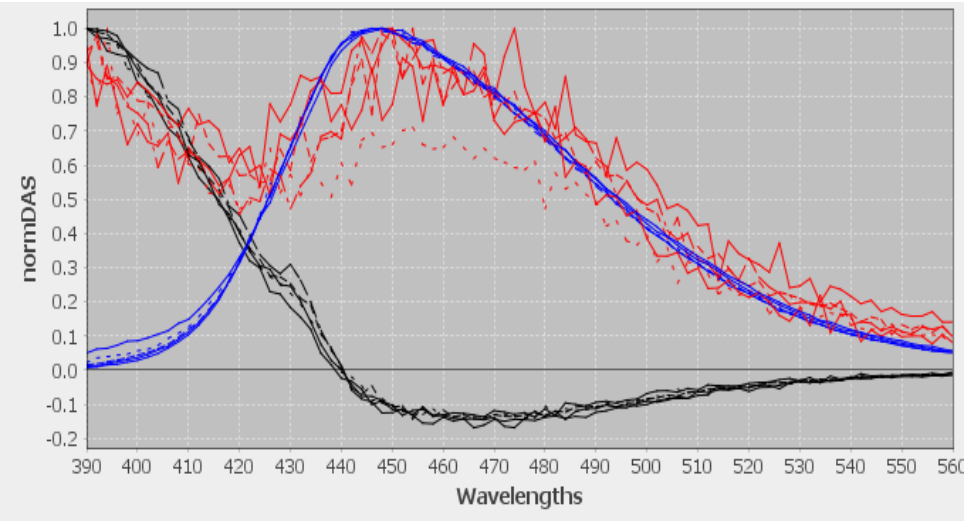

Figure S2**.** The results of global analysis of TRPL data measured for TLm in water in the pH range from 2–4

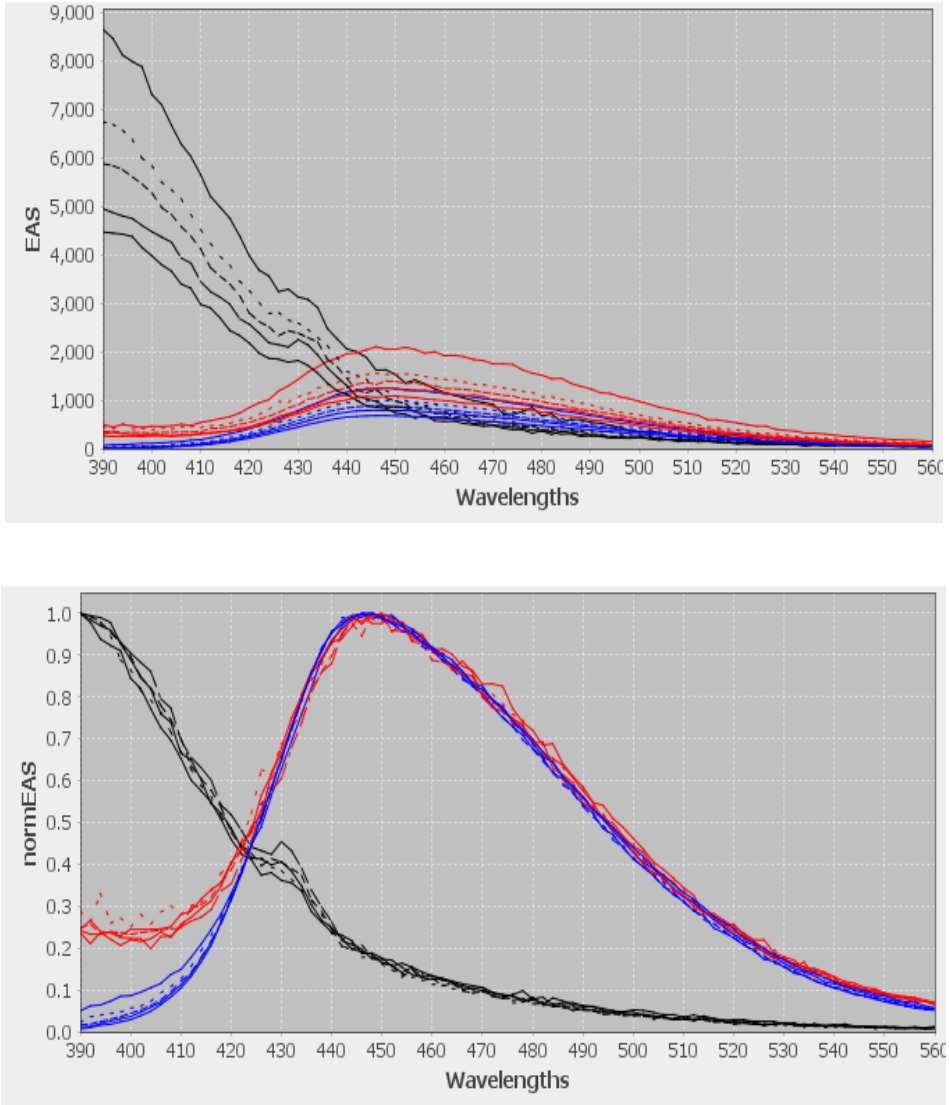

Figure S2. The results of global analysis of TRPL data measured for TLm in water in the pH range from 2–4 (continued)

The first DAS (black) has positive and negative parts, which can be interpreted as a transformation of the one component into another, by virtue of the observed slow rise time of the fluorescence in the observed emission traces at 450 nm (Figure S3). The shape of the second DAS corresponds to a mixture of two different components with similar decay times. The last component (blue DAS in Figure S2) has the most significant contribution to the steady-state fluorescence in Figure 2A.

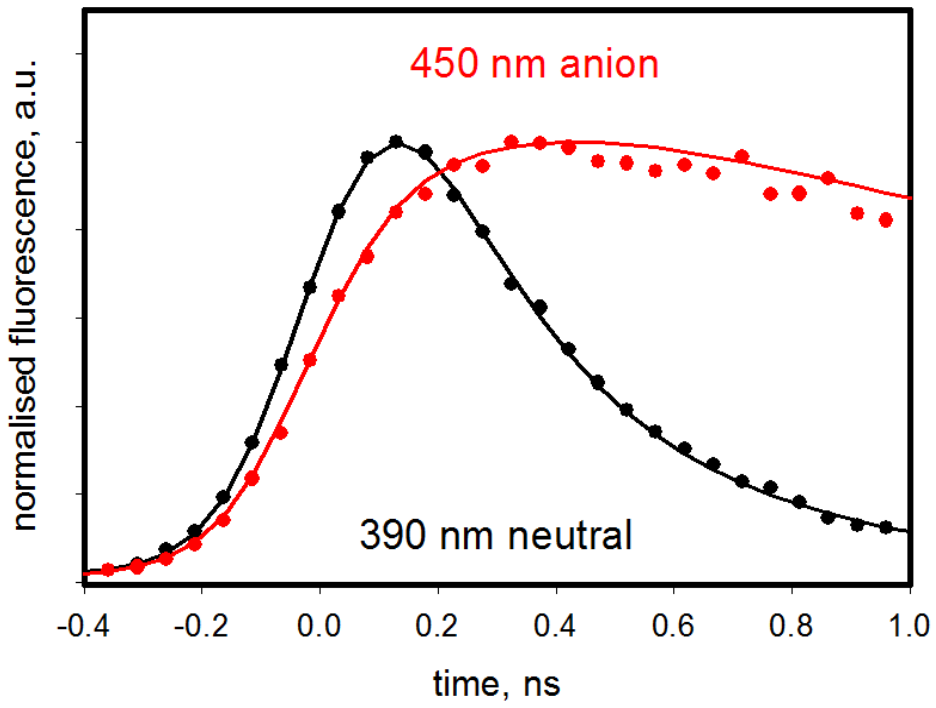

Figure S3. Fluorescence decays of TLm in water monitored at 390 nm (black) and 450 nm (red) at pH 1.77. The colored dots represent the raw data and the solid lines with the same colors correspond to the fits derived from the target analysis. A clear rise is seen at 450 nm for the anion, 3-A

To resolve the true spectra of the species, a target analysis was applied. The estimated spectra and applied target scheme are shown in Figure S4. Full summary of the target analysis is shown in the Figure S5. Each of the compartments in the estimated spectra of the species in Figure S4 is modeled as a bi-exponential decay. The estimated lifetimes of the components from target analysis are summarized in Table 1, in which each component has a major and minor population with distribution around 90 and 10 % respectively, giving rise a total of 4 lifetime values (Table 1).

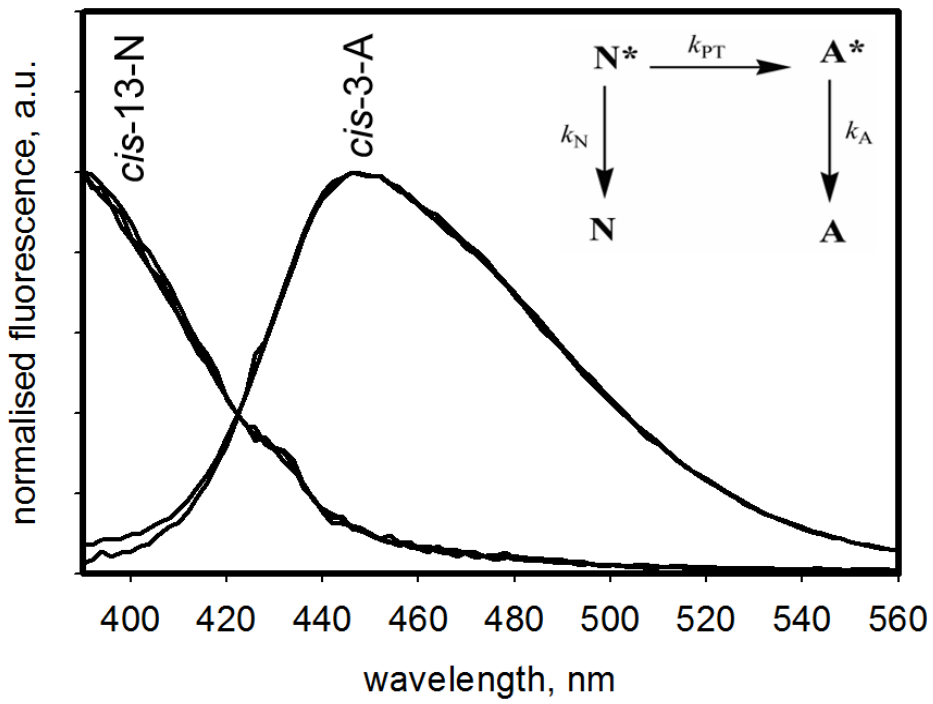

Figure S4. SAS of TLm in water in the pH range from 2–4 with the kinetic scheme resulted from target analysis (see below)

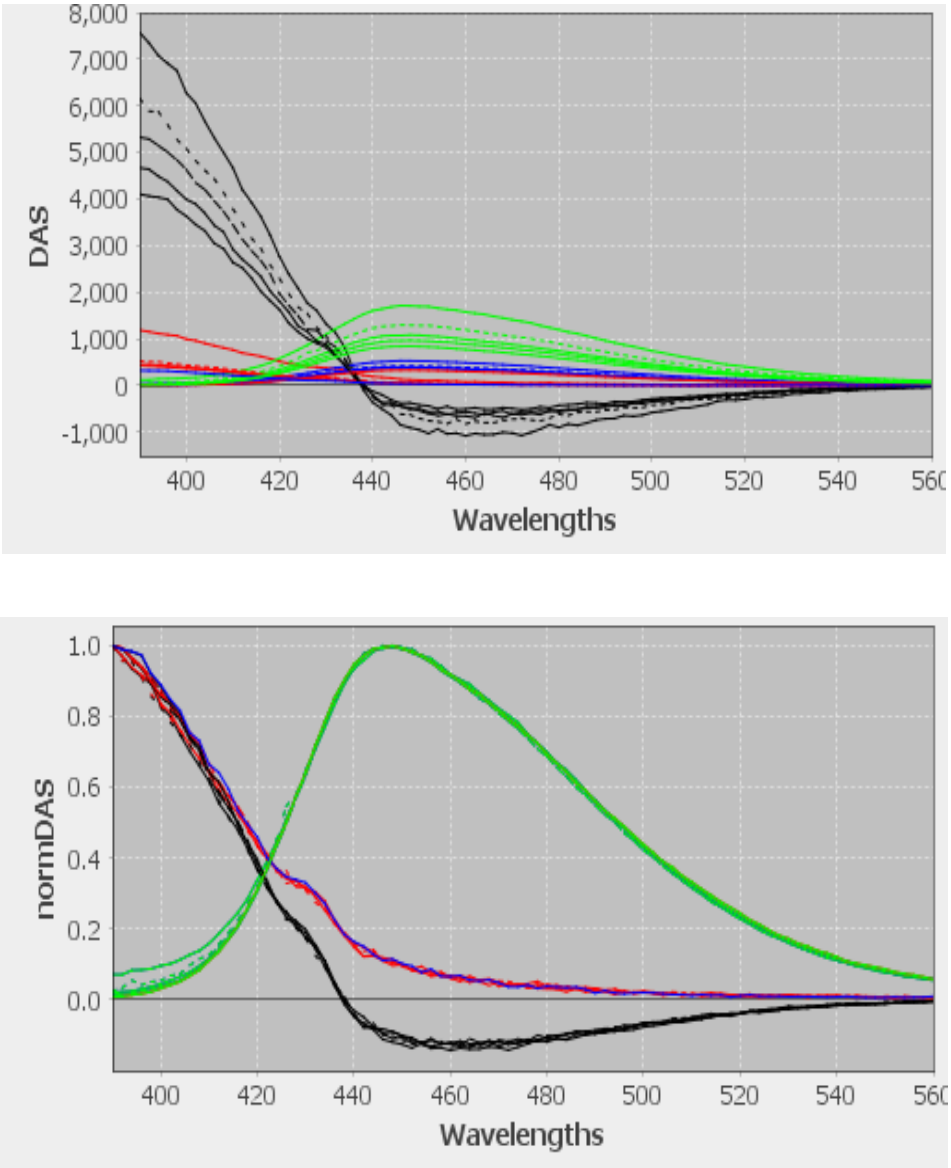

Figure S5. The results of target analysis of TRPL data measured for TLm in water at pH range from 2–4

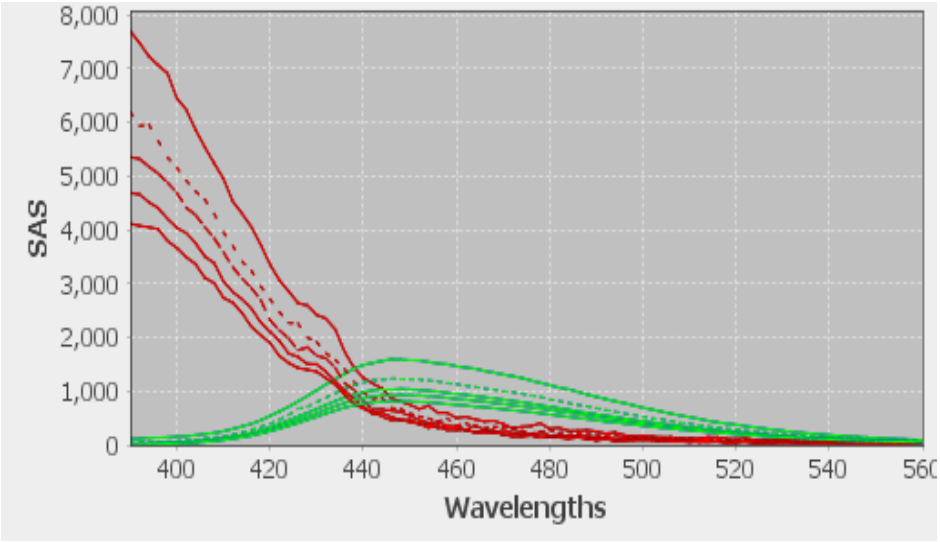

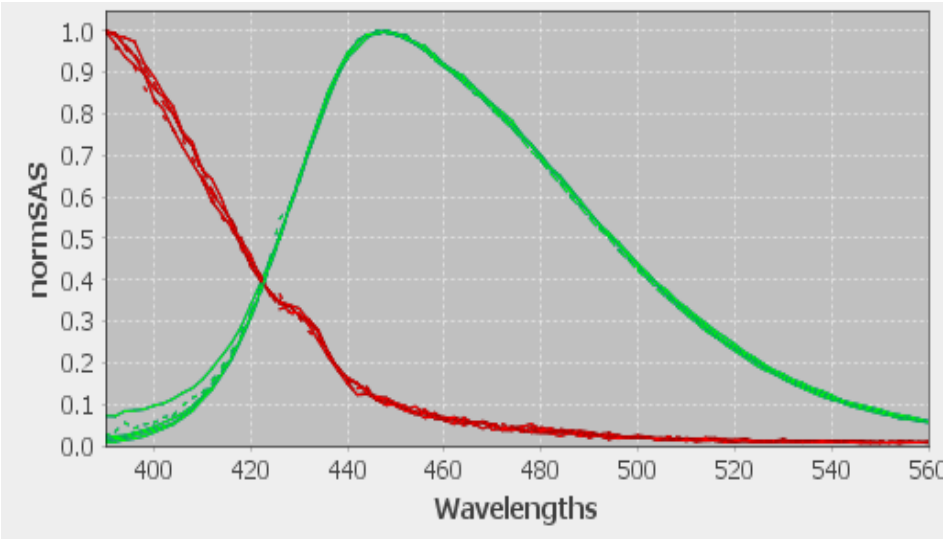

Figure S5. The results of target analysis of TRPL data measured for TLm in water at pH range from 2–4 (Continued)

Considering the trend in stability of the neutral and anionic tautomers of TLm at ground states (see main text), the fast-major component was assigned to *cis*-13-N, which emits at 390 nm (Figure 10) The component was deprotonated through ESPT on the order of 250 ps. In addition, considering the calculated pK_a values in Figure 7, the resultant species from deprotonation step was attributed to *cis*-3-A species, whose emission amplitudes at 450 nm and lifetime around 7.9 ns was increasing with pH due

to suppression of acid quenching. (Denofrio, Thomas, Braun, Oliveros, & Lorente, 2008; Klein & Tatischeff, 1987) Observed non-exponentiality of the species could be attributed to ESPT/back reaction or germinate recombination. Comparison with the analysis for the TRPL data observed for TLm in Methanol (MeOH) and D_2O is made in Figures S6 and S7. Assuming 1.45 ns is an intrinsic lifetime of *cis*-13-N component; ESPT can be calculated to be on the order of 3.2 ns^{-1}.

The compartmental model for TLm system with ESPT (the inset in Figure S4) describes the kinetic expression behinds an ESPT process, in which N* represents the excited *cis*-13-N population while A* the excited *cis*-3-A population. The rate constants k_N and k_A correspond to decay to the ground state for neutral and anionic, respectively and k_{PT} is the rate of proton transfer from *cis*-13-N to *cis*-3-A. The population transfer of neutral excited state (N*) to anionic excited state (A*) is considered as an example in accordance with the known two-state model as described by the following eq 1 and eq 2.

$$\frac{dN^*(t)}{dt} = -(k_N + k_{PT})\, N^*(t)$$

$$\frac{dA^*(t)}{dt} = k_{PT}N^*(t) - k_A A^*(t) \qquad (1)$$

$$N^*(t) = N_0^*\, e^{-(k_N+k_{PT})t} = N_0^*\, e^{\frac{-t}{\tau_1}}$$

$$A^*(t) = -\frac{N_0^*\, k_{PT}}{k_N + k_{PT} - k_A}\, e^{-\frac{t}{\tau_1}} + \frac{N_0^*\, k_{PT}}{k_N + k_{PT} - k_A}\, e^{-\frac{t}{\tau_2}}$$

$$\tau_1 = \frac{1}{k_N+k_{PT}} \qquad \tau_2 = \frac{1}{k_A} \qquad (2)$$

S1.2 TRPL of TLm in MeOH and D_2O.

The global analysis for the time-resolved emission data observed for TLm in MeOH is shown in Figure S6, where only neutral components are expected. There are no signs of any interconversion between components. Therefore, the parallel model was used to fit the data. The sample in MeOH shows fluorescence dominated by the component with a lifetime of 1.45 ns and spectral peak around 390 nm. The second component with amplitude (around 20% or so) has a lifetime around 315 ps and spectral maximum around 405 nm. The two components interchanged with one another. The third minor component with the lifetime of the 6 ns has its spectral maximum at 455 mn. The dominated component of 1.45 ns is overlapping well with cis-13-N specie resolved in the target analysis (Figure S5). The interpretation of the spectra and lifetime observed in MeOH is based on the lack of ESPT process. The resolved emission lifetime and maximum are 1.45 ns at 390 nm for cis-13-N species, 315 ps at 405 nm for 38-N decay time, and 6 ns at 455 nm for 3-A species in MeOH. In D_2O (Figure S7), slower rise time for the *cis*-3-A component at 450 nm is observed when compared to that in water at the same pH (Figure S2), which also confirms the occurrence of the ESPT process.

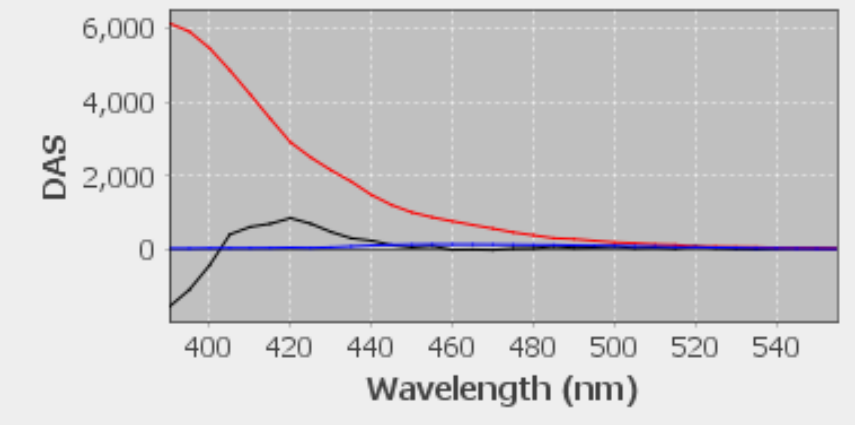

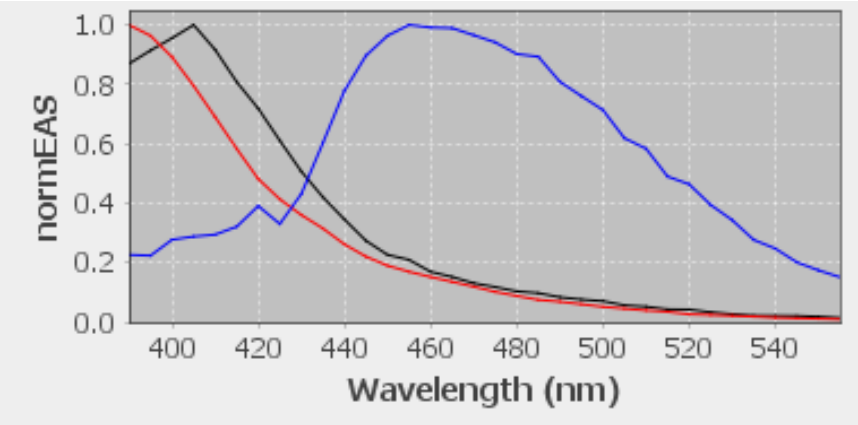

Figure S6. The results of global analysis of TRPL data measured for TLm in MeOH

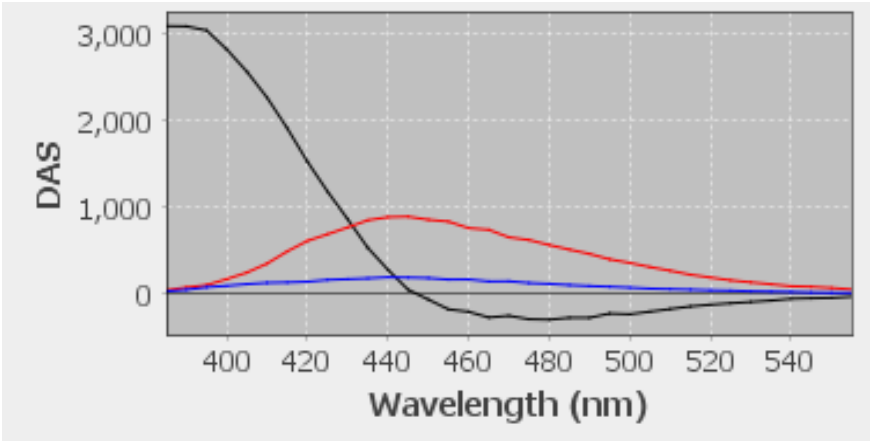

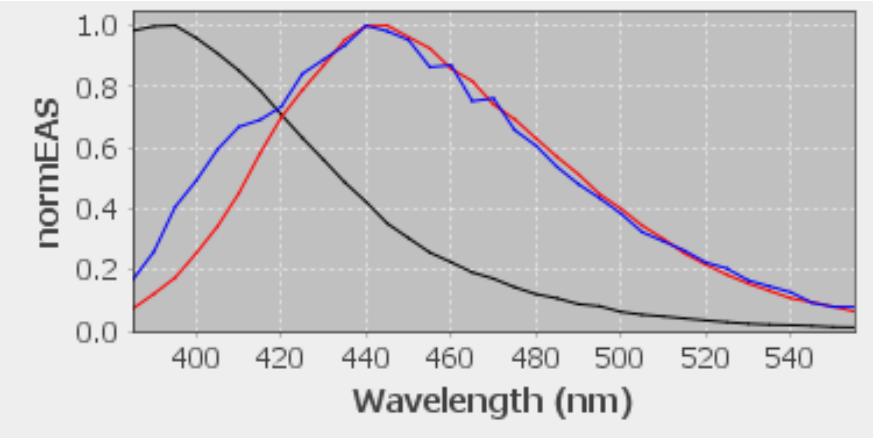

Figure S7. The results of global analysis of TRPL data measured for TLm in D_2O (pD 2.4)

S.1.3. TRPL of TLm in water (pH 4–6)

There are at least 3 lifetimes necessary to fit the TRPL data in that group (Figure S8). All datasets in that group can be fitted simultaneously. There are no signs of any interconversion between components. Therefore, the estimated DAS can be assigned to real species spectra. The estimated lifetimes (Figure S9) were: 470 ps, 3.0 ns, and 7.3 ns with emission maxima at 405, 415, 440 nm, respectively (Table 1). The relative amplitudes of the components are also changing with the pH.

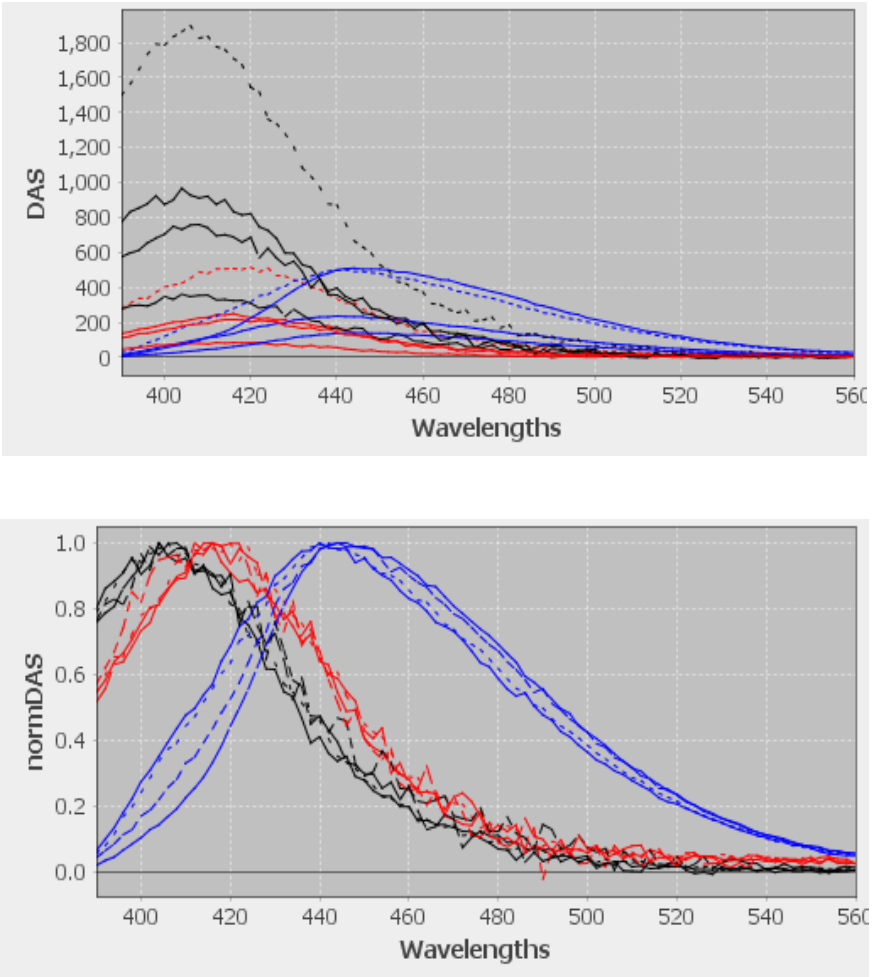

Figure S8. The results of global analysis of TRPL data measured for TLm in water at pH range from 4–6

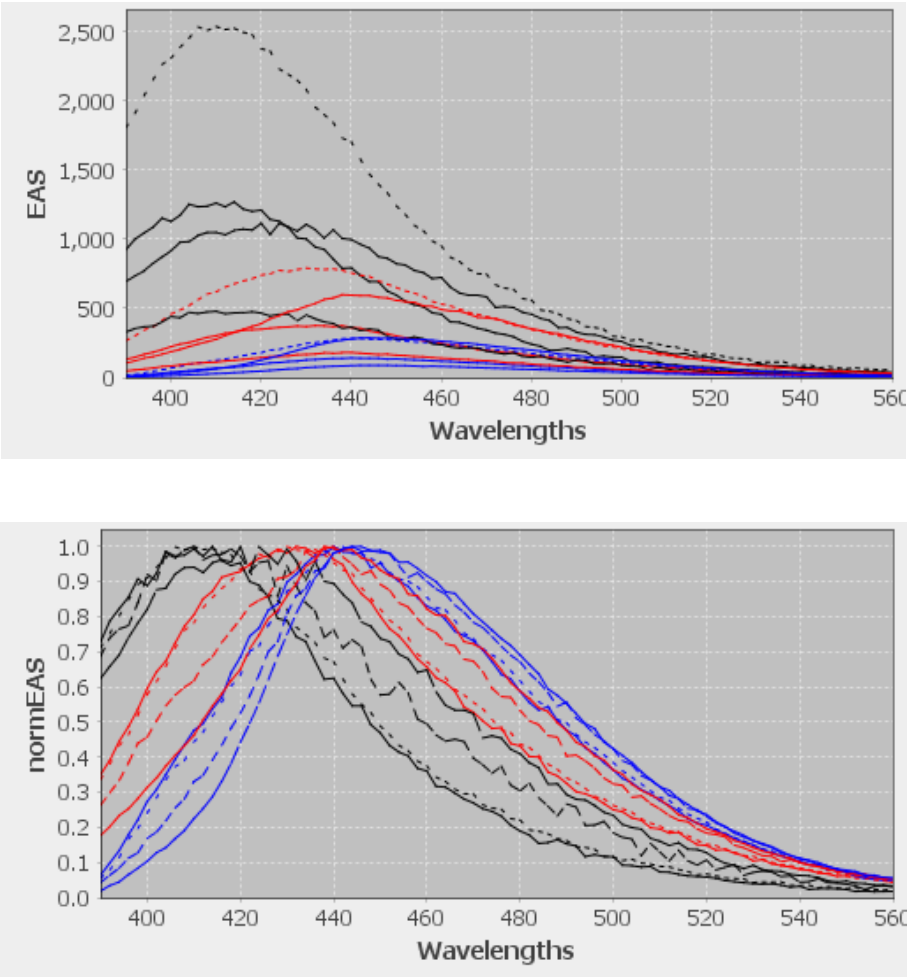

Figure S8. The results of global analysis of TRPL data measured for TLm in water at pH range from 4–6 (Continued)

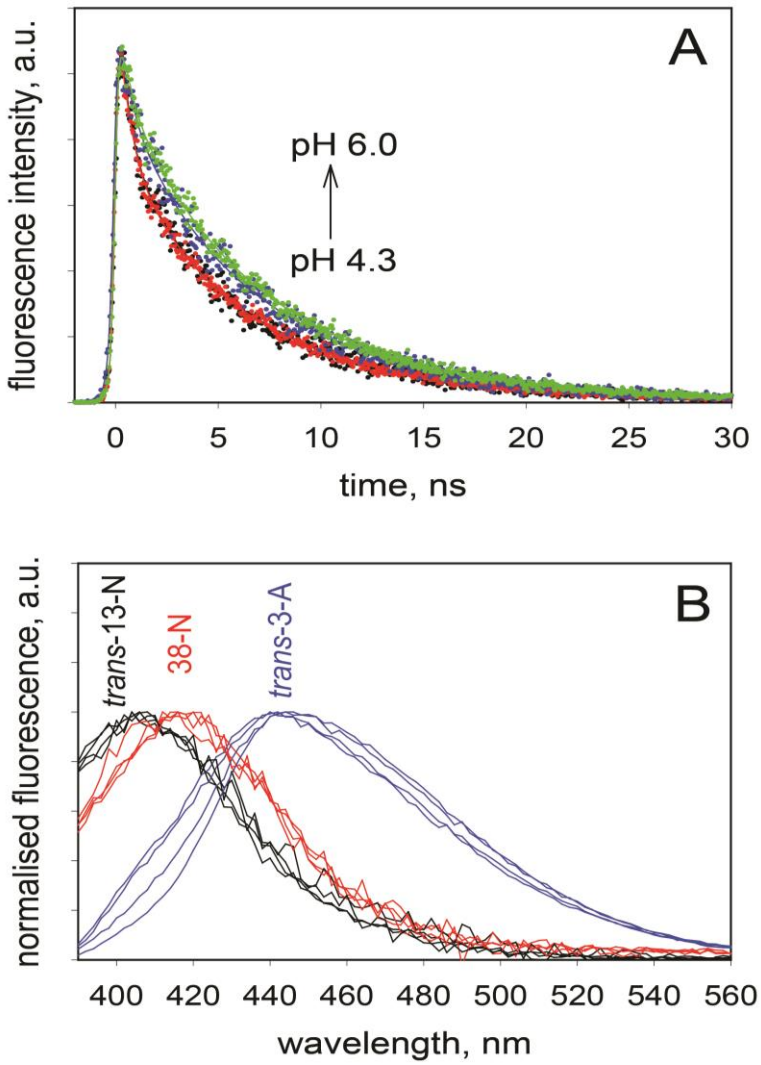

Figure S9. A) Fluorescence decay traces of TLm in water monitored at 450 nm after 375 nm excitation in the pH range from 4 to 6. Colored dots represent the raw data and colored solid lines correspond to the fits derived from the global analysis. B) Global analysis results for TLm in water in the same pH range (data are fitted simultaneously)

The average fluorescence lifetime is continuing to increase with the increase of pH, as shown in Figure S9A. The estimated spectra for datasets measured at pH 4.3 till pH 6.0 are presented in Figure S9B. In Figure S9B, normalization clearly reveals the first two species to have lifetimes of 470 ps with a peak position at 405 nm and 3.0 ns with a peak position at 415 nm, regardless of the pH chosen. However, the specie

with the lifetime of 7.3 ns, whose emission maximum occurs at 440 nm become narrower with the increase of pH value. This observation is accompanied by non-exponentiality of the component with the lifetime of 3.0 ns (415 nm). For Example, at pH 4.3, the spectrum of this species can be decomposed into a linear combination of two species. Moreover, Figure S10 shows the spectrum of that component with lifetime of 3.0 ns overlaid with the difference between components with lifetime of 7.3 ns measured at pH 6.0 and pH 4.3. Such nice overlapping can be explained by relating the species at 7.3 ns to that at 3.0 ns.

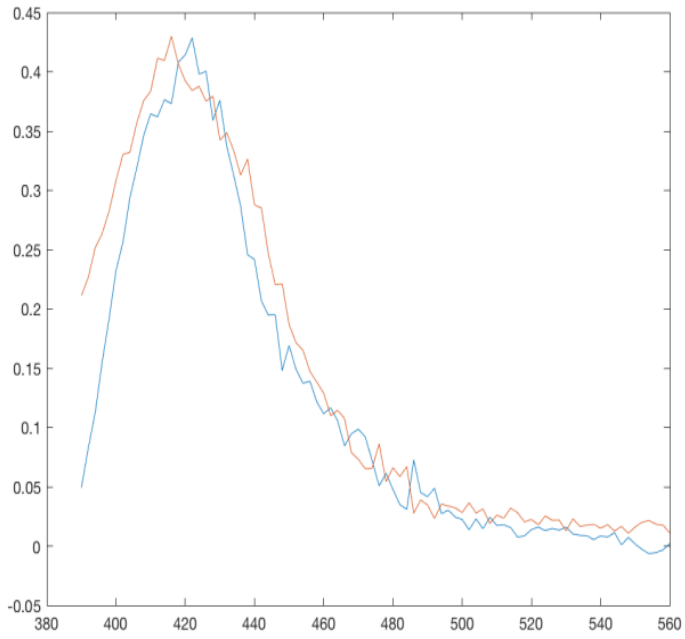

Figure S10. The overlapping of the spectrum 3.3 ns component with the difference between components with lifetime of 7.4 ns measured at pH 6.6 and pH 4.4

Following the prototropic equilibrium in Chart 2 (pK_a ~ 4-5; pH 4.3 in Table 1), which is associated with the protonation-deprotonation equilibrium between 38-N and 3-A, it is plausible to assume that in this pH range 4–6, the narrowing of spectrum at

440 nm, which belongs to the species with lifetime 7.3 ns upon increasing the pH is due to the deprotonation of 38-N (415 nm, 3.0 ns), forming *trans*-3-A form, with no signs of ESPT activity. Moreover, the third specie belongs to *trans*-13-N (405 nm, 470 ps), which is expected to be red-shifted relative to the spectrum for *cis*-13-N (405 versus 390 nm; see theoretical production in the main text).

S.1.4. TRPL of TLm in water at pH 6–8 and pH 8–10.

There are once again 3 lifetimes necessary to fit the TRPL data in any of these pH ranges within a parallel model: 470 ps (405 nm), 3.7 ns (430 nm), and 7.9 ns (450 nm), see Figures S11 and S12 for pH range from 6-8, as well as 550 ps (420 nm), 3.7 ns (430 nm), and 7.9 ns (450 nm), see Figures S13 and S14 for pH range from 8-10.

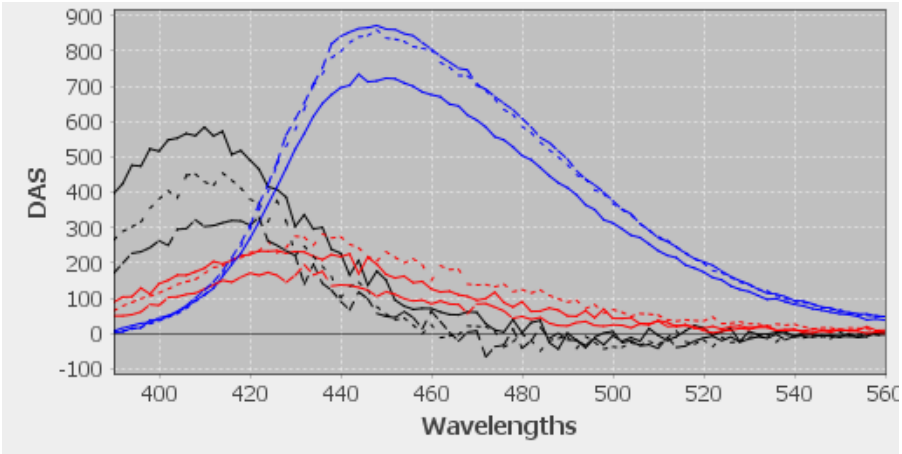

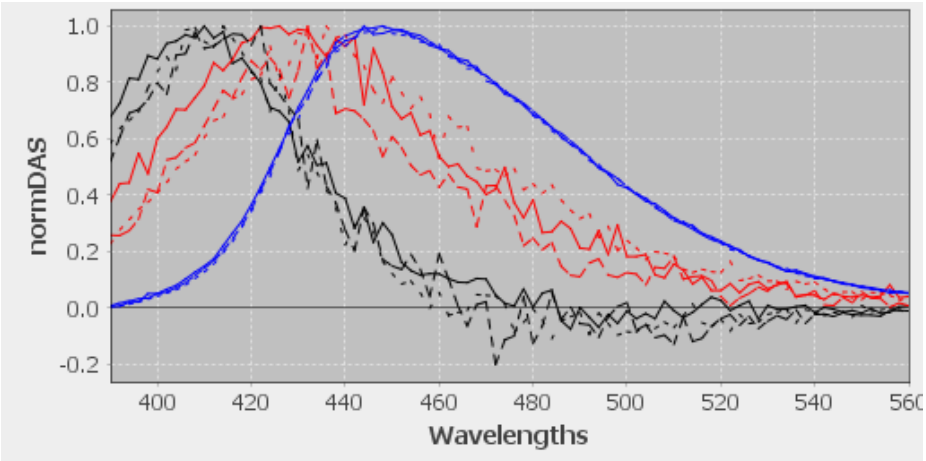

Figure S11. The results of global analysis of TRPL data measured for TLm in water at pH range from 6–8

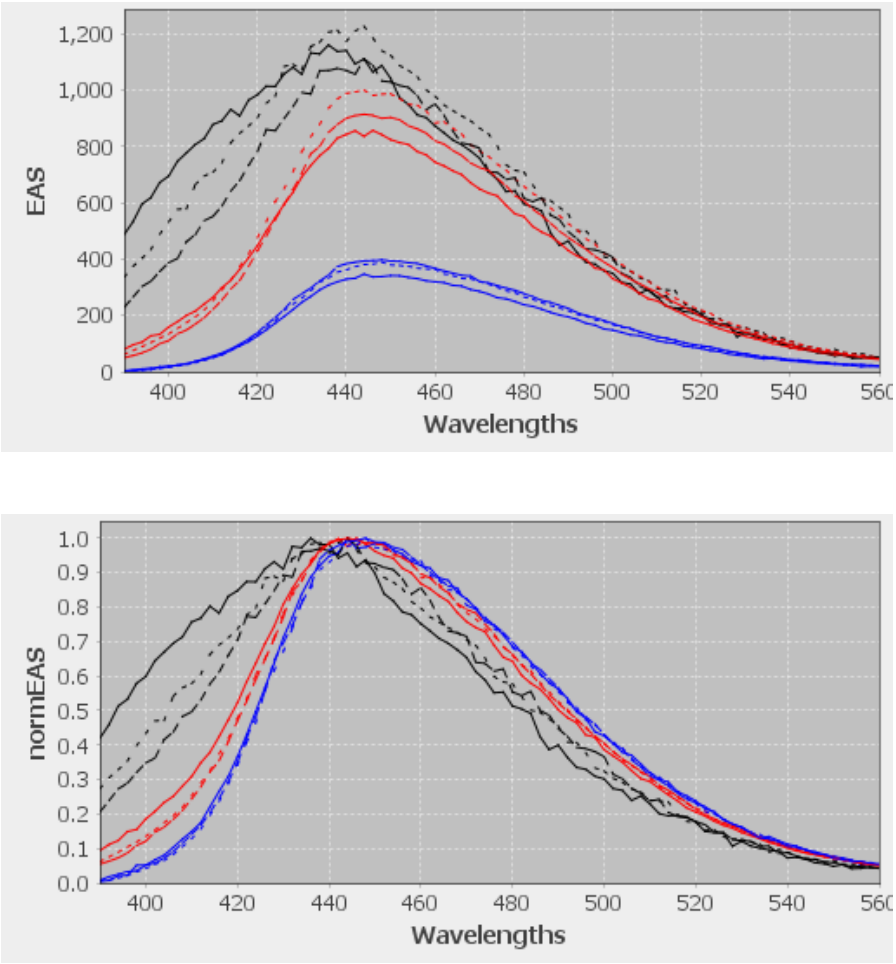

Figure S11. The results of global analysis of TRPL data measured for TLm in water at pH range from 6–8 (Continued)

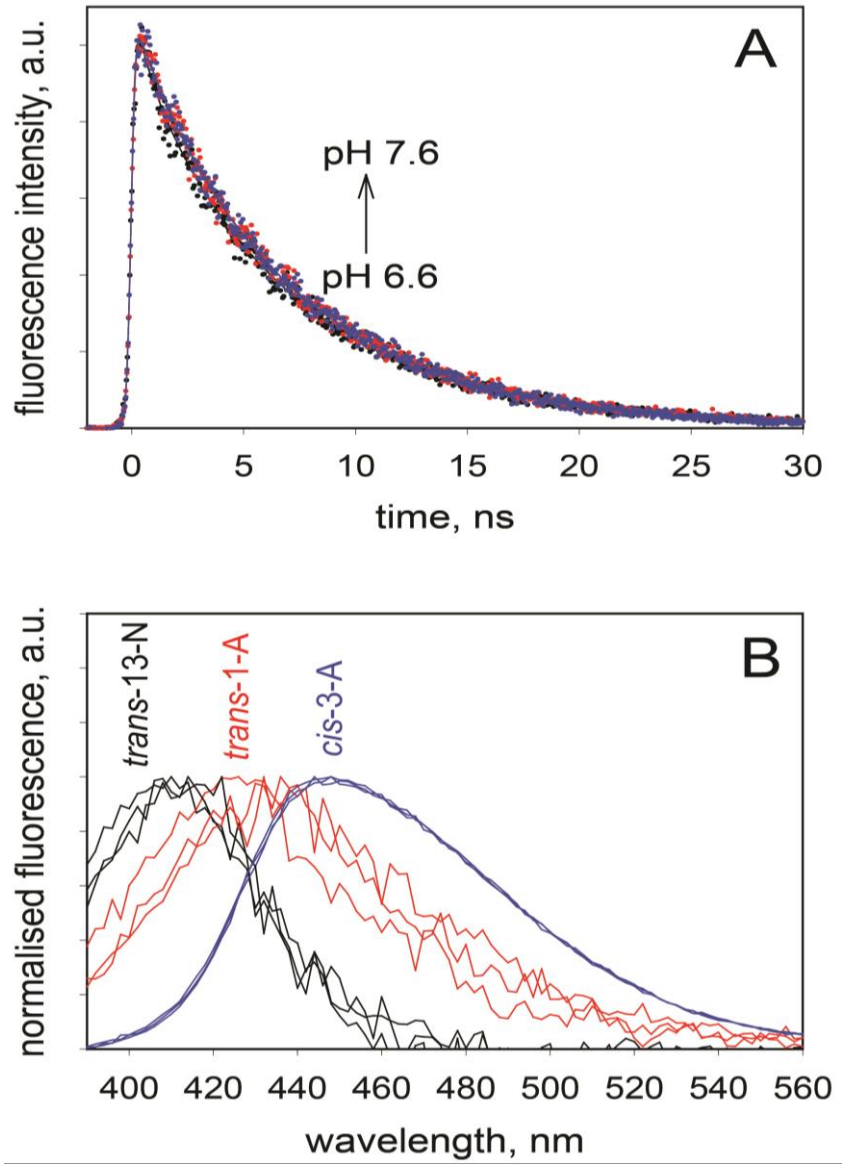

Figure S12**.** A) Fluorescence decay traces of TLm in water monitored at 450 nm after 375 nm excitation in the pH range from 6 to 8. Colored dots represent the raw data and colored solid lines correspond to the fits derived from the global analysis. B) Global analysis results for TLm in water in the same pH range (data are fitted simultaneously)

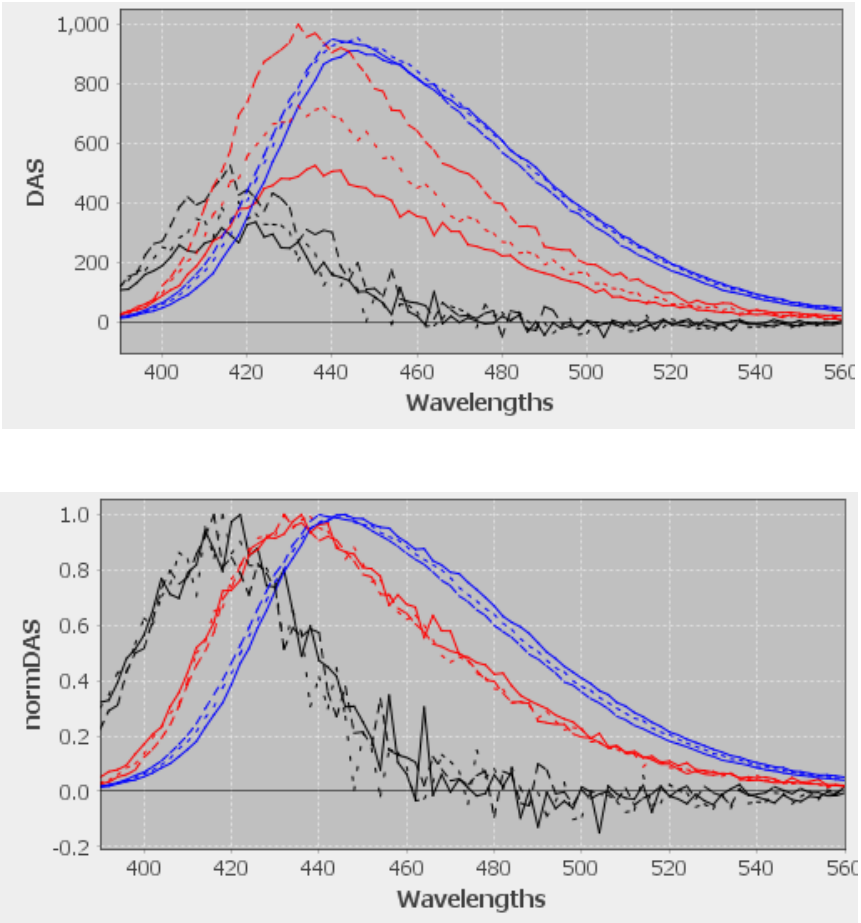

Figure S13**.** The results of global analysis of TRPL data measured for TLm in water at pH range from 8–10

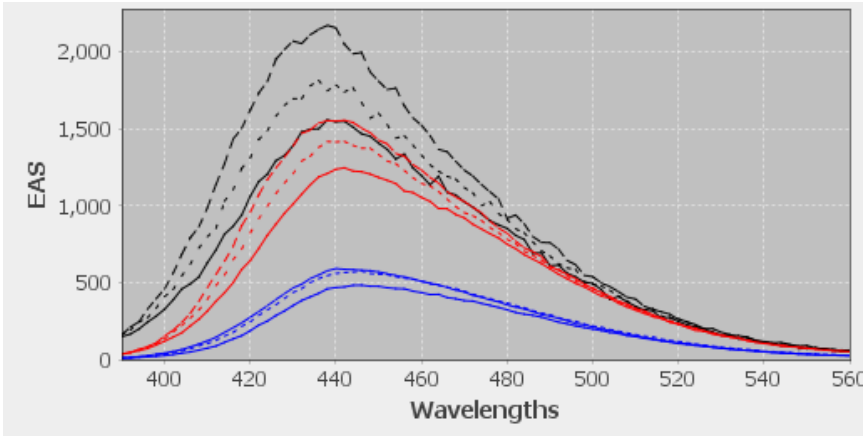

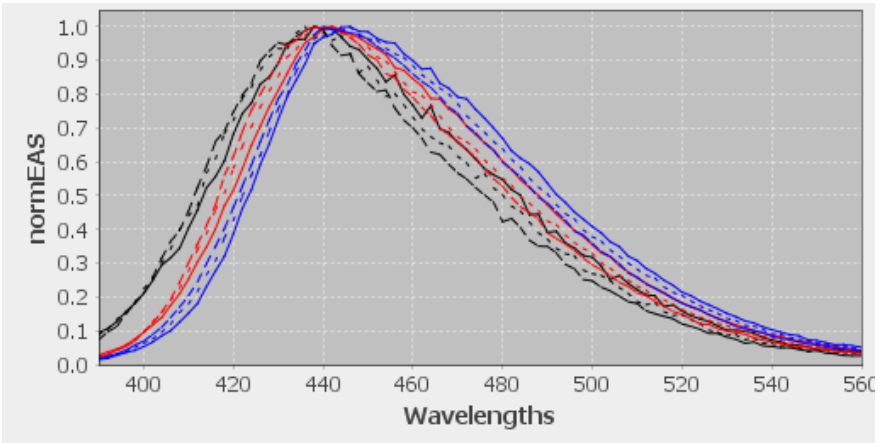

Figure S13. The results of global analysis of TRPL data measured for TLm in water at pH range from 8–10 (continued)

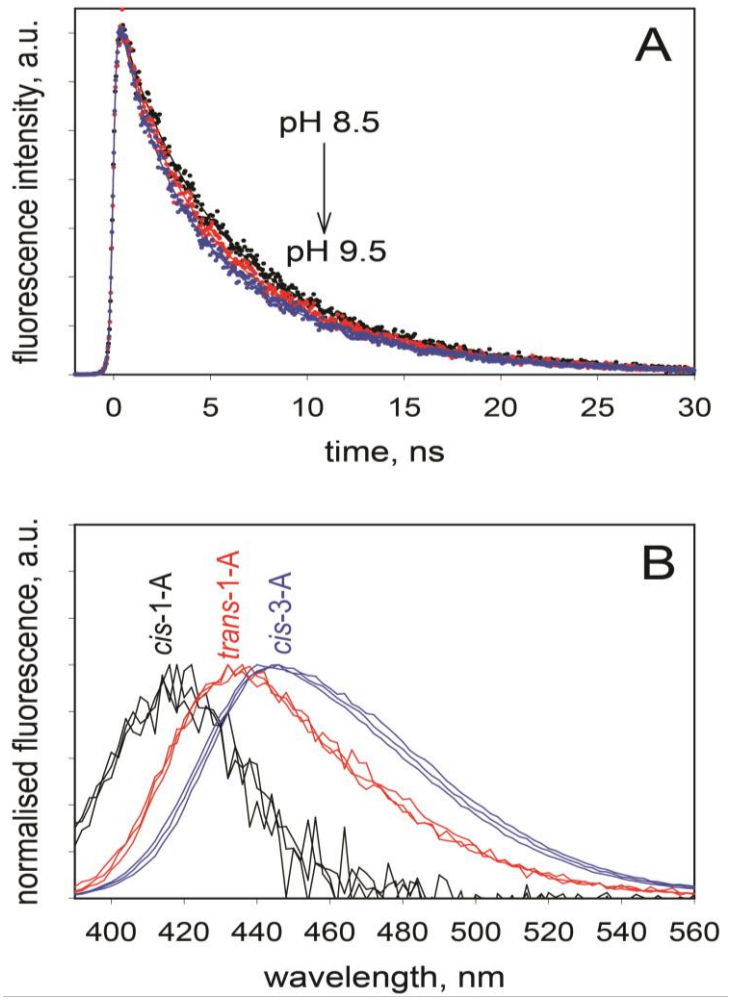

Figure S14. A) Fluorescence decay traces of TLm in water monitored at 450 nm after 375 nm excitation in the pH range from 8 to 10. Colored dots represent the raw data and colored solid lines correspond to the fits derived from the global analysis. B) Global analysis results for TLm in water in the same pH range (data are fitted simultaneously)

The conclusion from analyzing the data in these pH ranges (6–8 and 8–10) is that deprotonation of *trans*-13-N (405 nm, 470 ps) generates *trans*-1-A (430 nm, 3.7 ns) with a concomitant production of *cis*-3-A species (450 nm, 7.9 ns) and *cis*-1-A species (420 nm, 550 ps) in the pH range from 8–10 presumably from an unresolved *cis*-13-N due to basic quenching. No signs of ESPT activity were observed in either pH ranges. These assignments once again come in harmony with the theoretical

prediction of pK_a values in Chart 2 (pK_a ~8–10) that is associated with the protonation-deprotonation equilibrium between 13-N and either 3-A (pK_a ~8 in Chart 1; 6.6 in Table 1) or 1-A (pK_a ~10 in Chart 1; 8.5 in Table 1). Notice that the amplitudes of DAS spectra that belong to *trans*-1-A were very low in the pH range below pK_a value of 8.

S.1.5. TRPL of TLm in water at pH 10–12.

At pH 10–12, an evolution of fastest lifetime (420 nm, 550 ps) to a new component, whose emission peak appears around 435 nm and has a longer lifetime around 2.2 ns was observed (Figures S15, S16 and S17). The lifetime of fastest component in that case goes down to 146 ps with the increase in pH (Table 1). Addition of hydroxides has quenched emission of those species in the pH range, leading to a decrease in their lifetime.

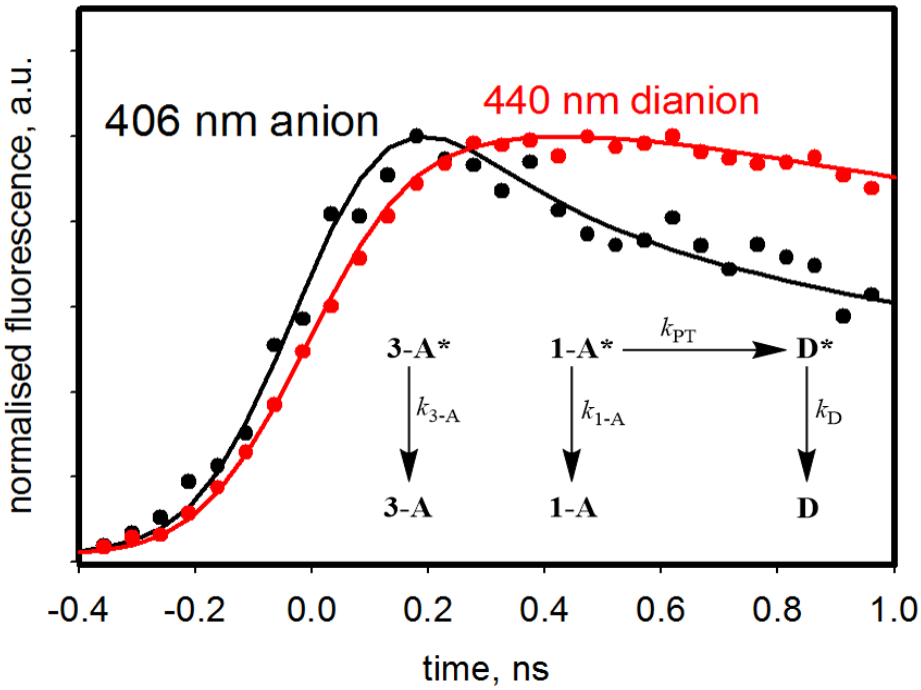

Figure S15. Fluorescence decay of TLm in water monitored at 405 nm (black) and 440 nm (red) at pH 11. Colored dots represent the raw data and colored solid lines correspond to the fits derived from the global/target analysis. A clear rise is seen at 440 nm for the dianionic, D

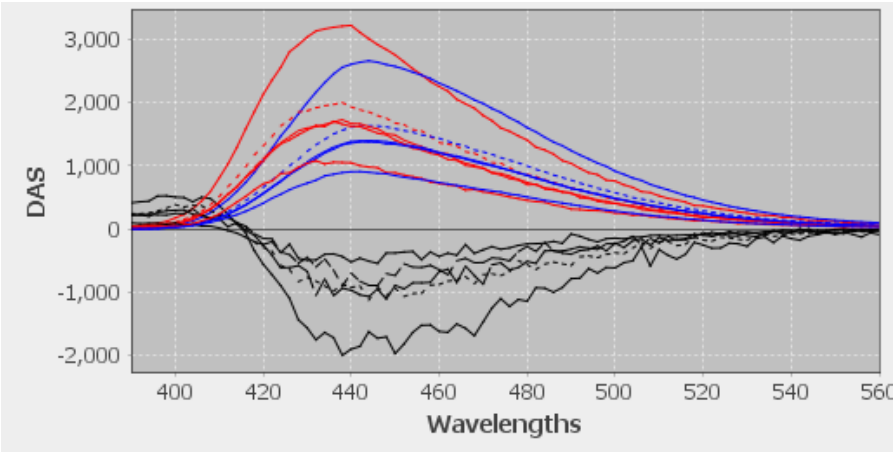

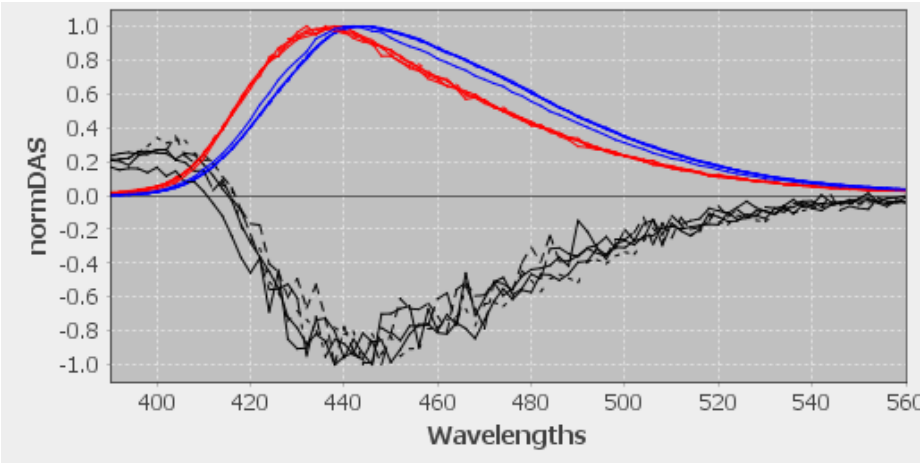

Figure S16. The results of global analysis of TRPL data measured for TLm in water at different pH values from 10–12

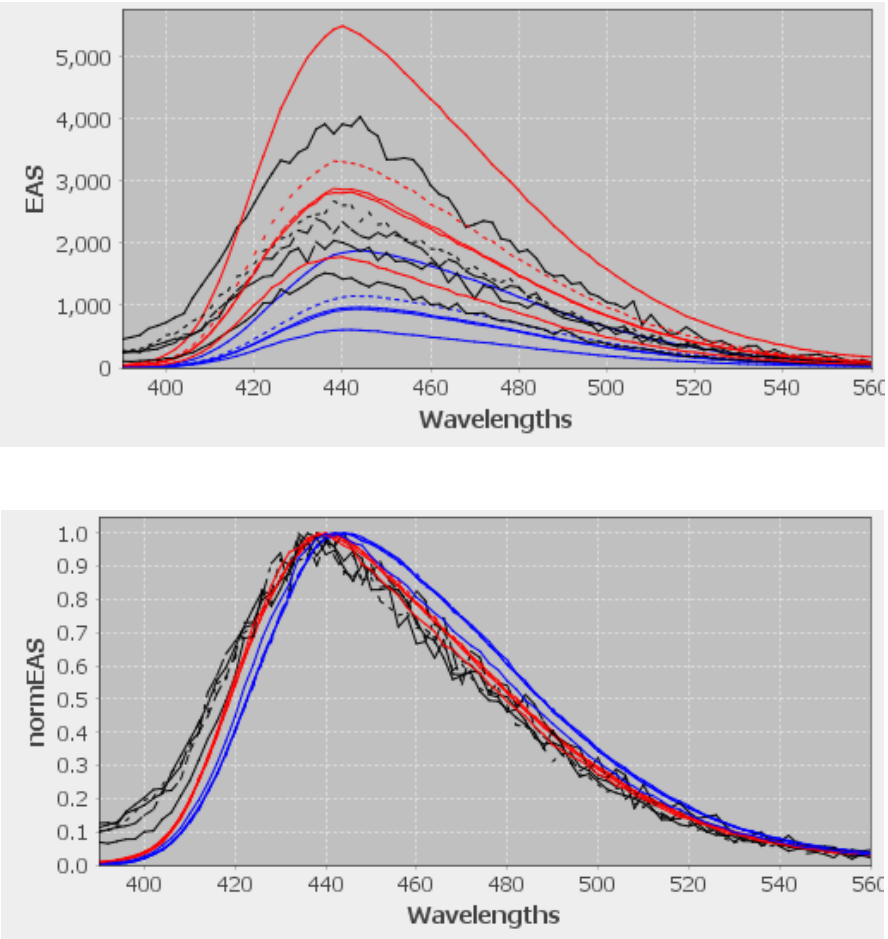

Figure S16. The results of global analysis of TRPL data measured for TLm in water at different pH values from 10–12 (continued)

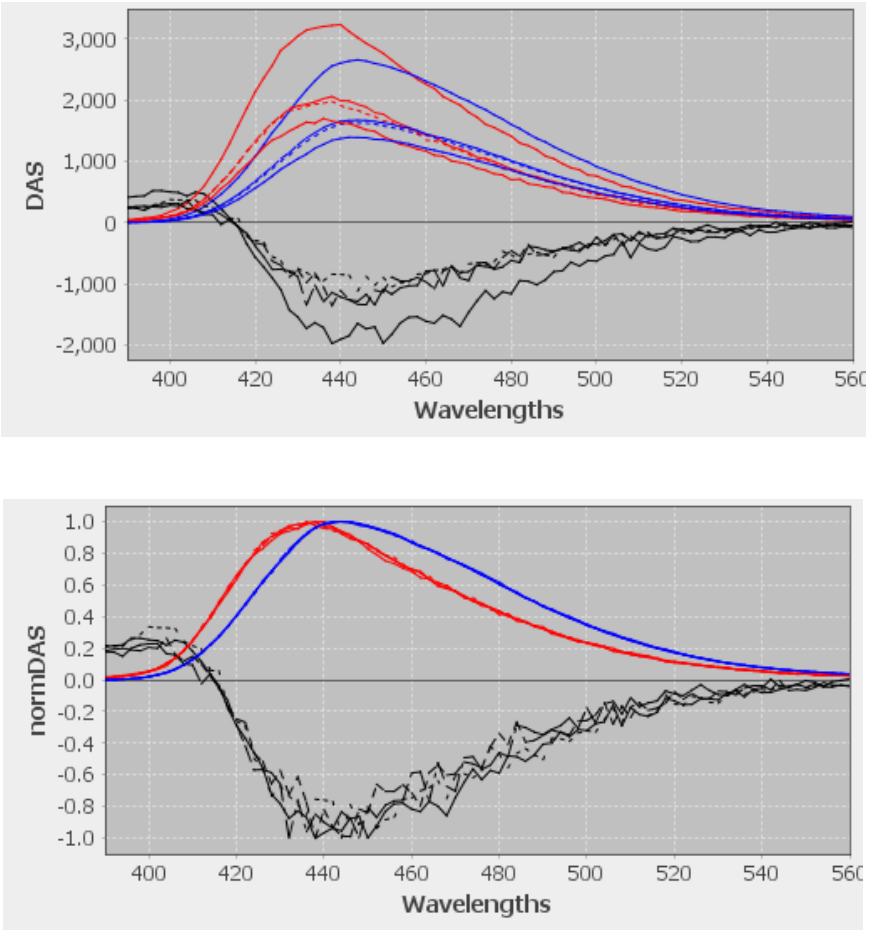

Figure S17. The results of target analysis of TRPL data measured for TLm in water at different pH values from 10–12

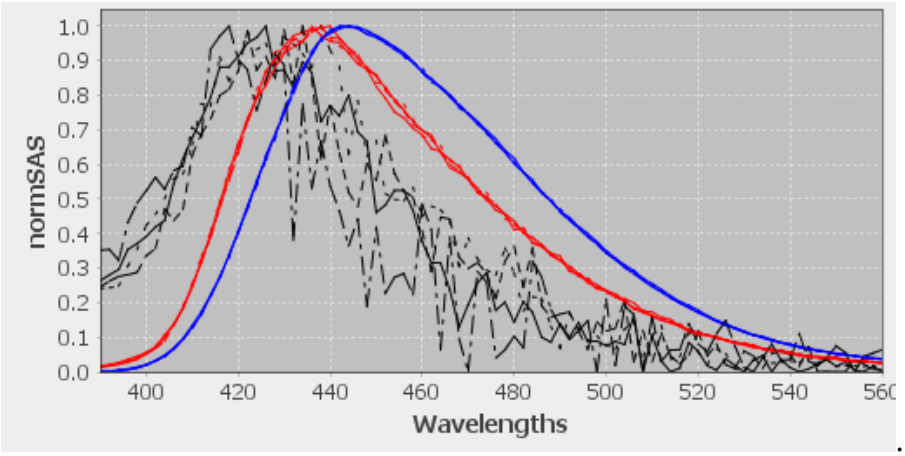

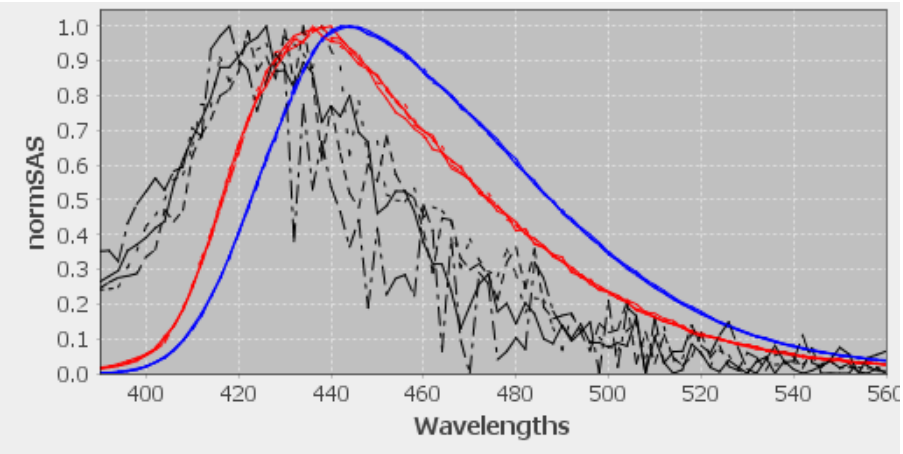

Figure S17. The results of target analysis of TRPL data measured for TLm in water at different pH values from 10–12 (continued)

Early results on the emission of Lm indicate that the fluorescence of LM is quenched by hydroxide anions.[1,2] The estimated lifetimes from the target analysis of datasets measured at pH 10–12 are 550 ps, 2.2 ns, 7.9 ns, whose emission peak occur at 420, 435, and 450 nm, respectively (Figure S18B). The average fluorescence lifetime doesn't change in this pH interval (Figure S18A). The conclusion from analyzing the data in this pH range is that second deprotonation of *cis*-1-A has formed D form (435 nm, 2.2 ns) through ESPT process, with a concomitant persistence of *trans*-3-A species (450 nm, 7.9 ns).

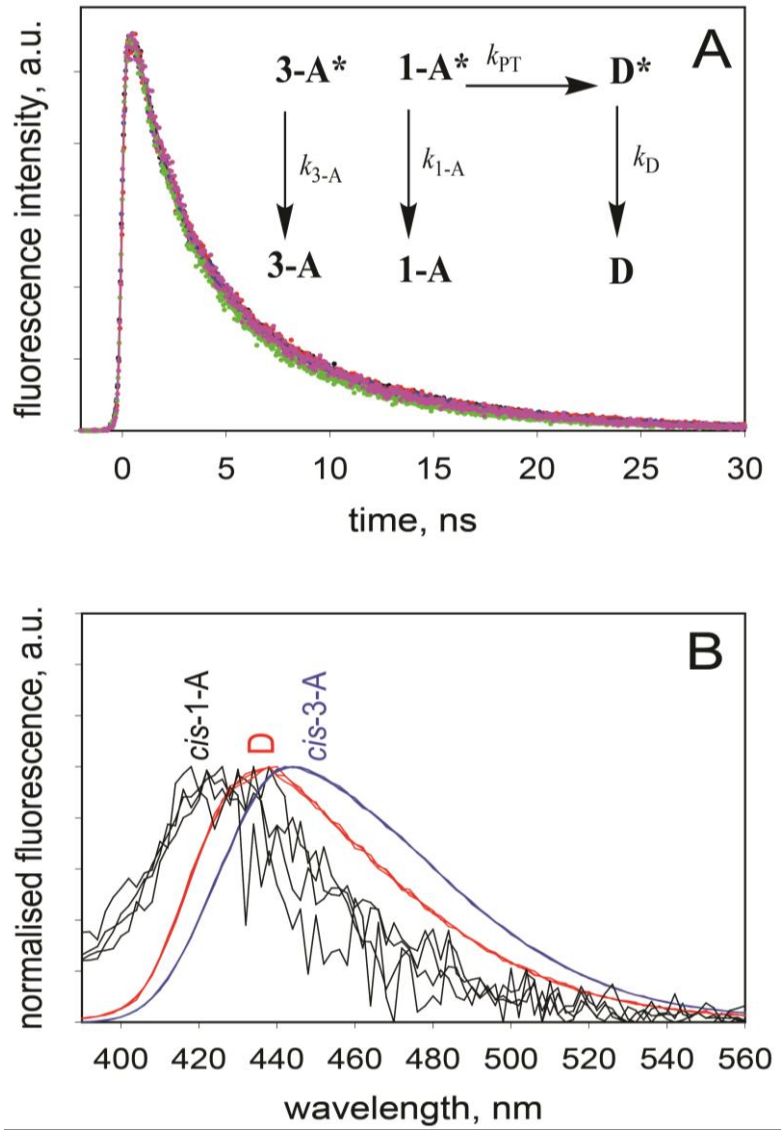

Figure S18. A) Fluorescence decay traces of TLm in water recorded at 440 nm after 375 nm excitation for the analyzed datasets in pH range from 10 to 12. B) SAS of TLm in water in the same pH range with the kinetic scheme resulted from target analysis

Part S2. Global analysis of TRPL data in the solid state.

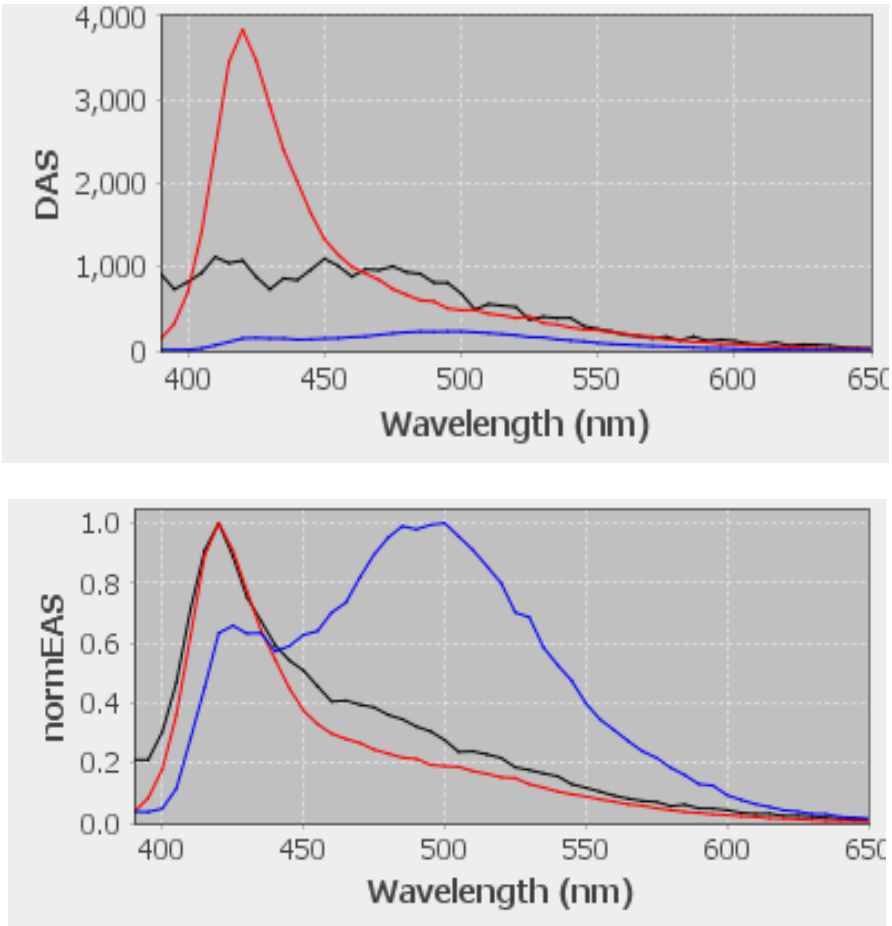

Figure S19. The results of global analysis of TRPL data measured for TLm solid

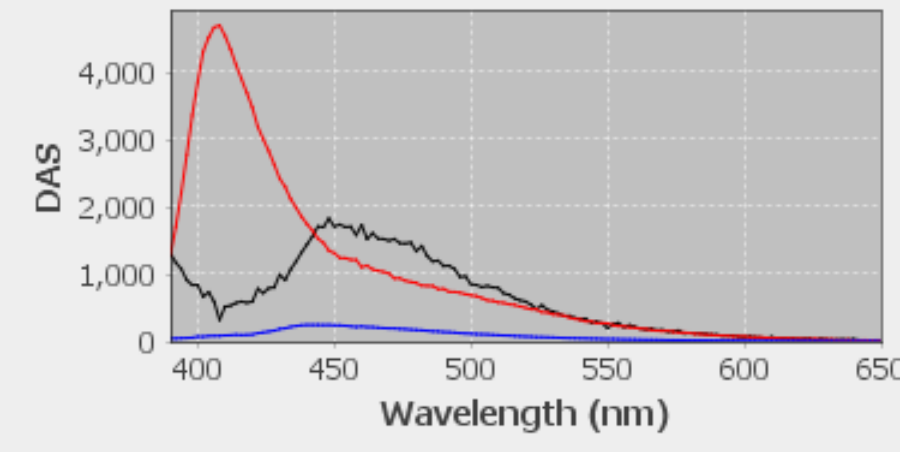

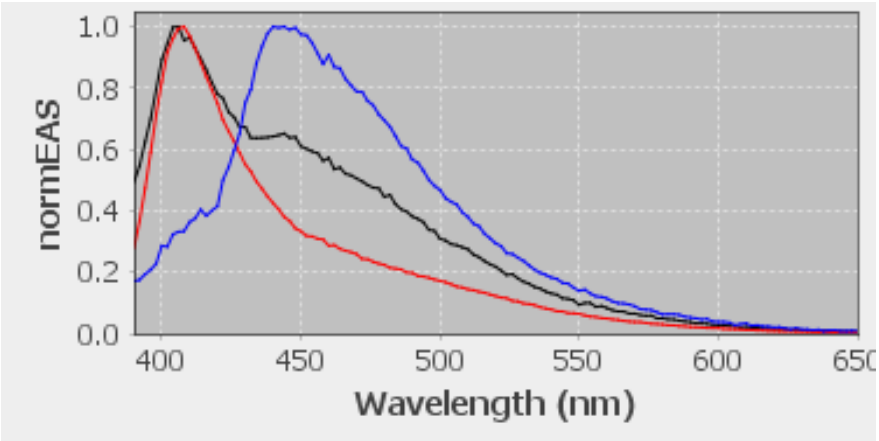

Figure S20. The results of global analysis of TRPL data measured for TLmNFs(vac)

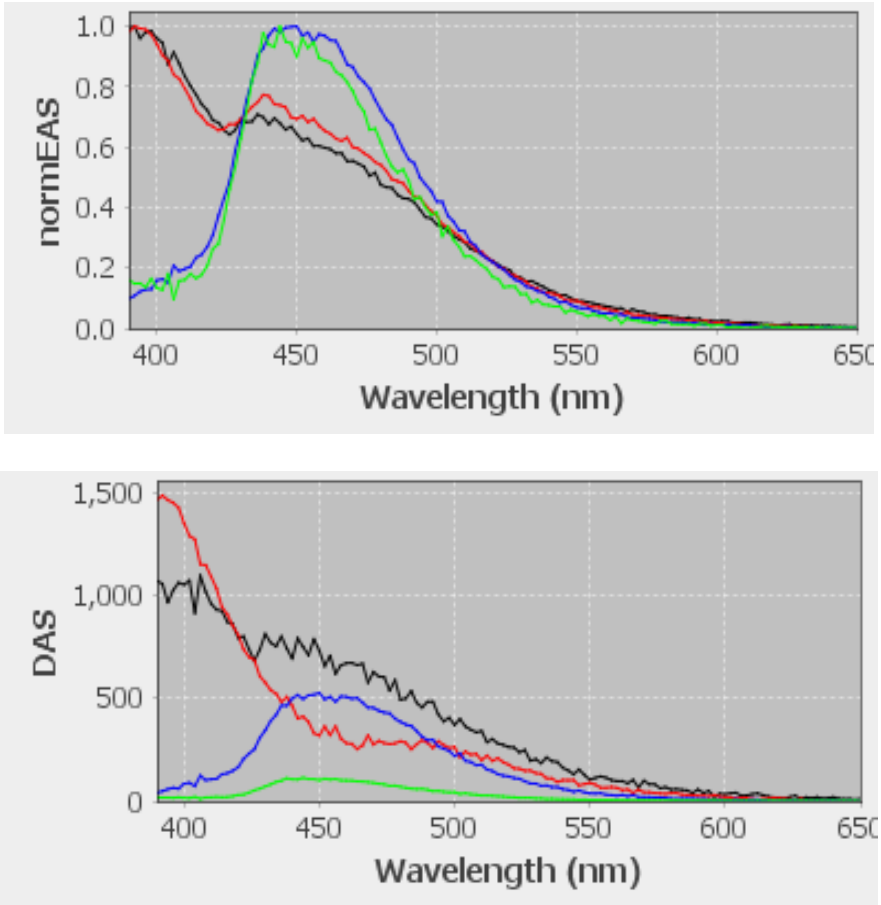

Figure S21. The results of global analysis of TRPL data measured for TLmNFs(atm)

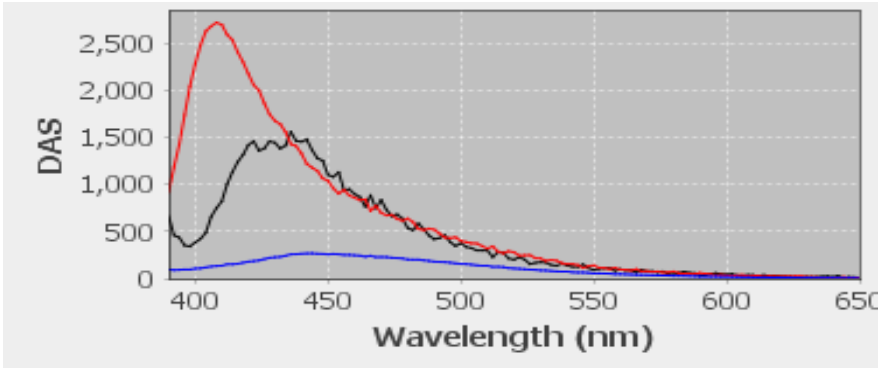

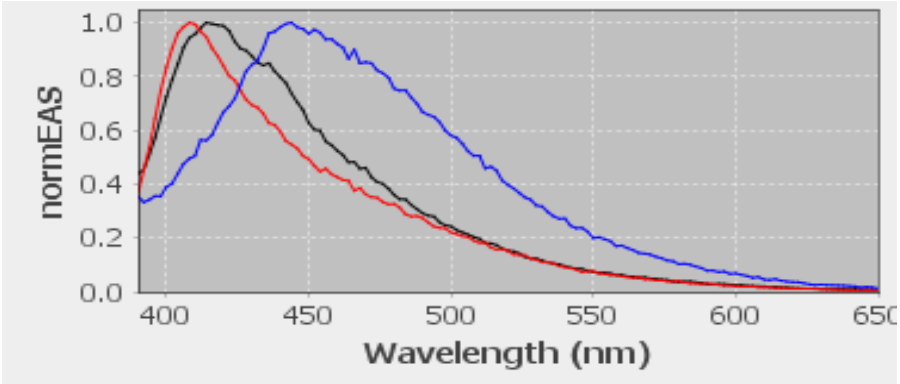

Figure S22. The results of global analysis of TRPL data measured for TLmNFs(vac)Hg^{2+}(5:1)

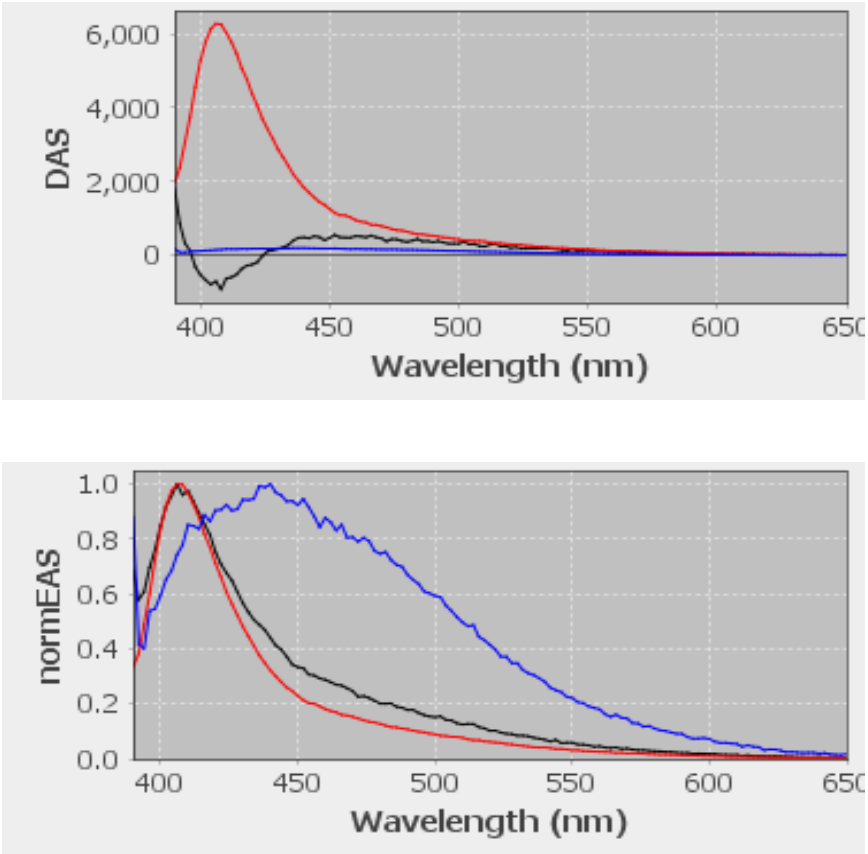

Figure S23. The results of global analysis of TRPL data measured for TLmNFs(vac)Hg^{2+} (1:200)

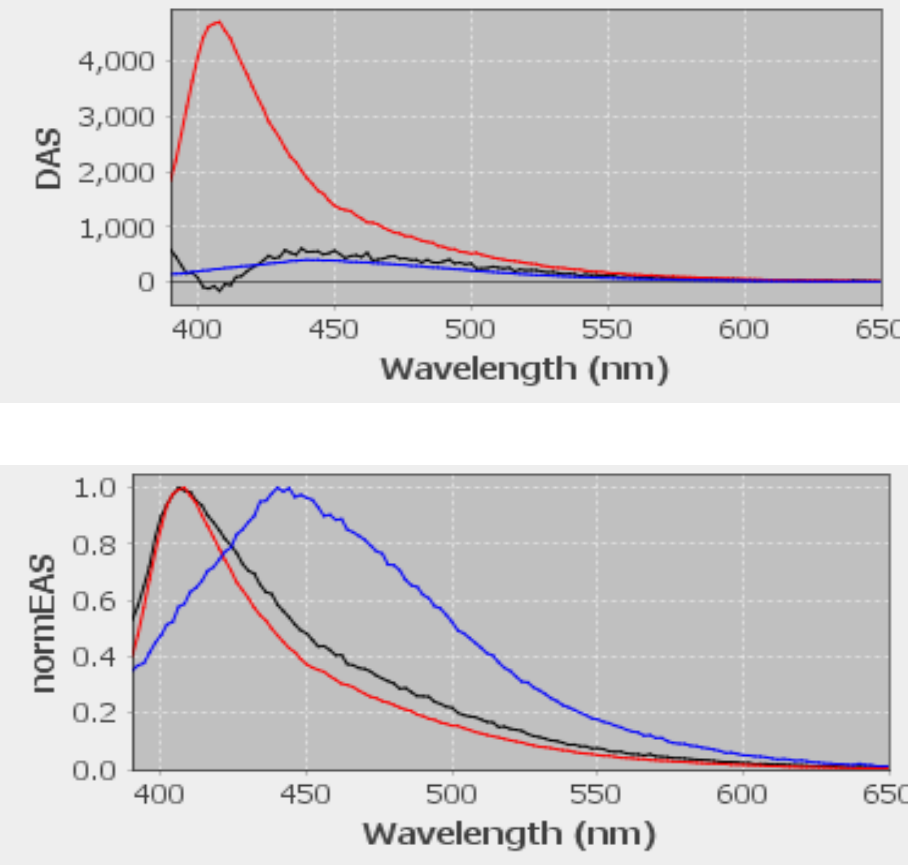

Figure S24. The results of global analysis of TRPL data measured for TLmNFs(vac)Hg^{2+} (1:200,000)

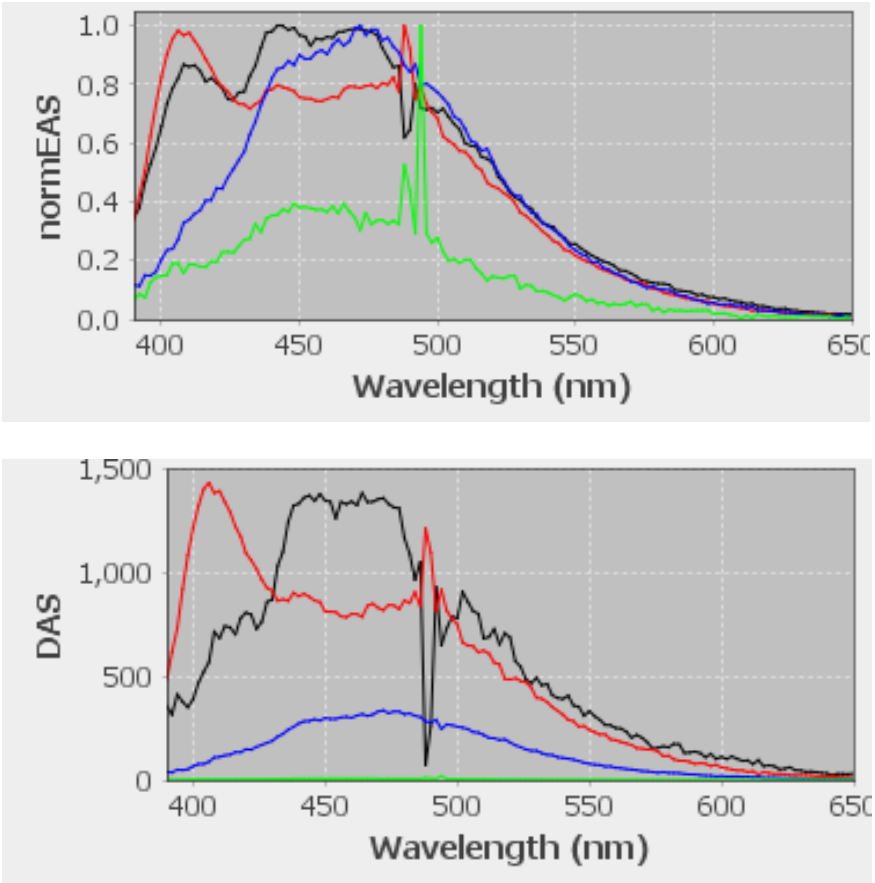

Figure S25. The results of global analysis of TRPL data measured for TLmNFs(atm)Hg^{2+} (5:1)

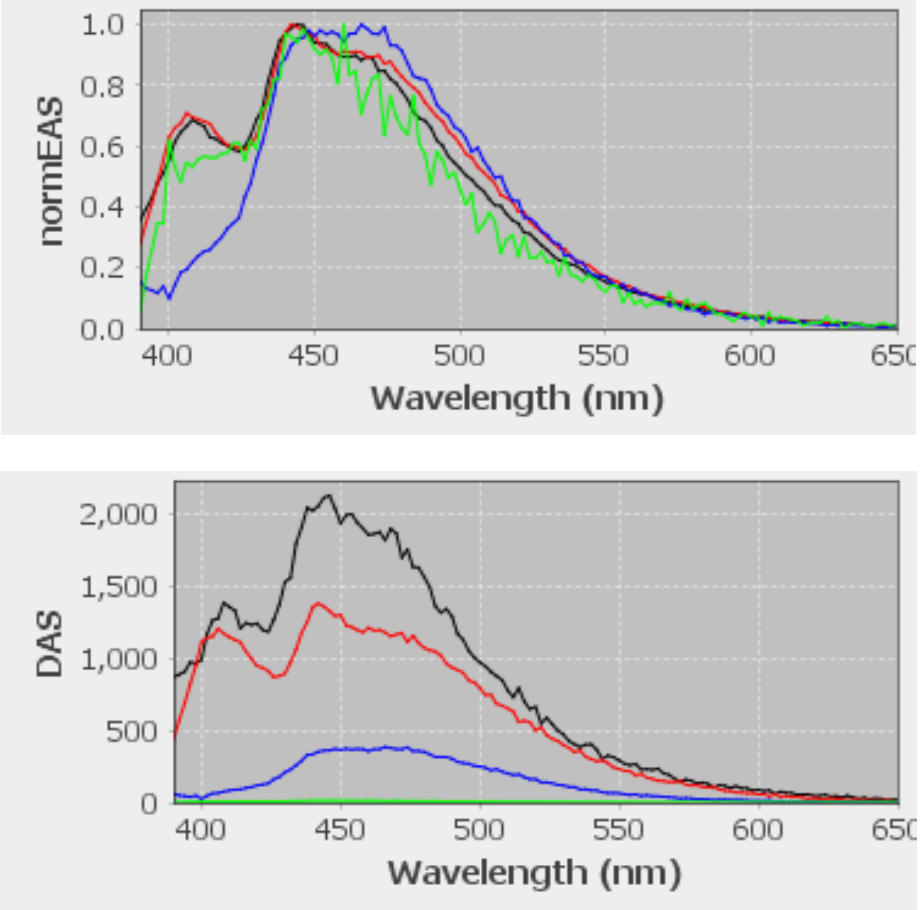

Figure S26. The results of global analysis of TRPL data measured for TLmNFs(atm)Hg^{2+}(1:200)

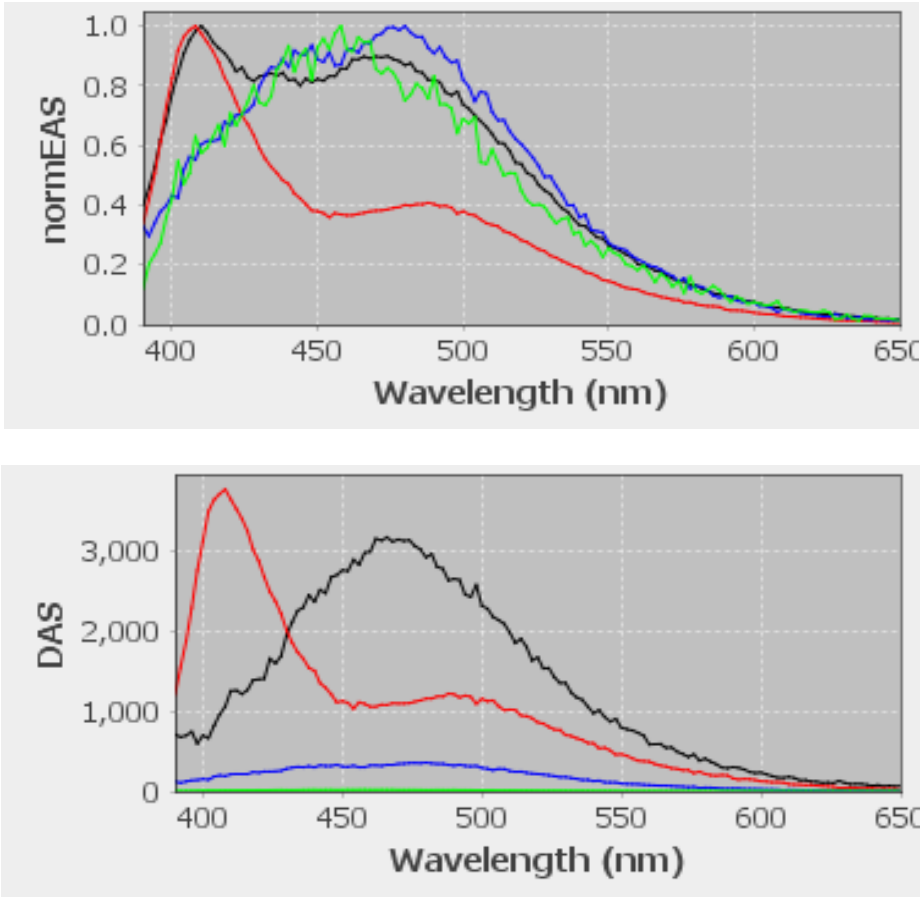

Figure S27. The results of global analysis of TRPL data measured for TLmNFs(atm)Hg^{2+}(1:200,000)

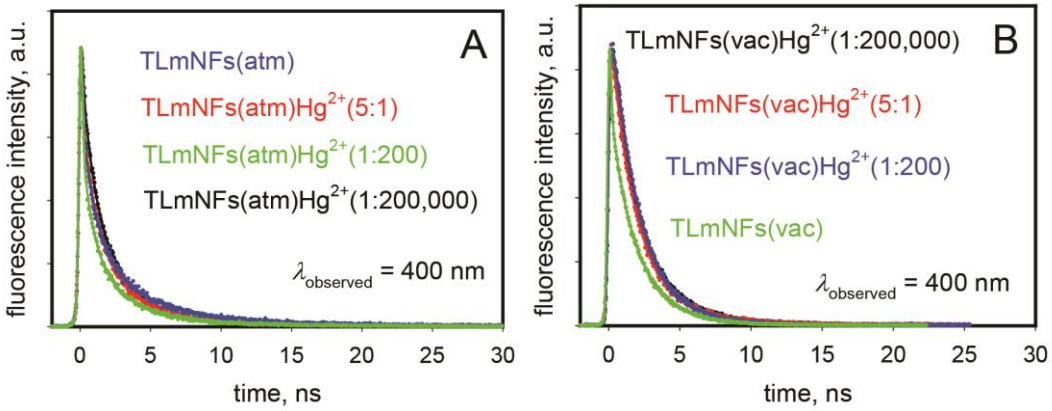

Figure S28. fluorescence decay traces of TLmNFs(atm) (A) and TLmNFs(vac) (B) monitored at 400 nm after 375 nm excitation

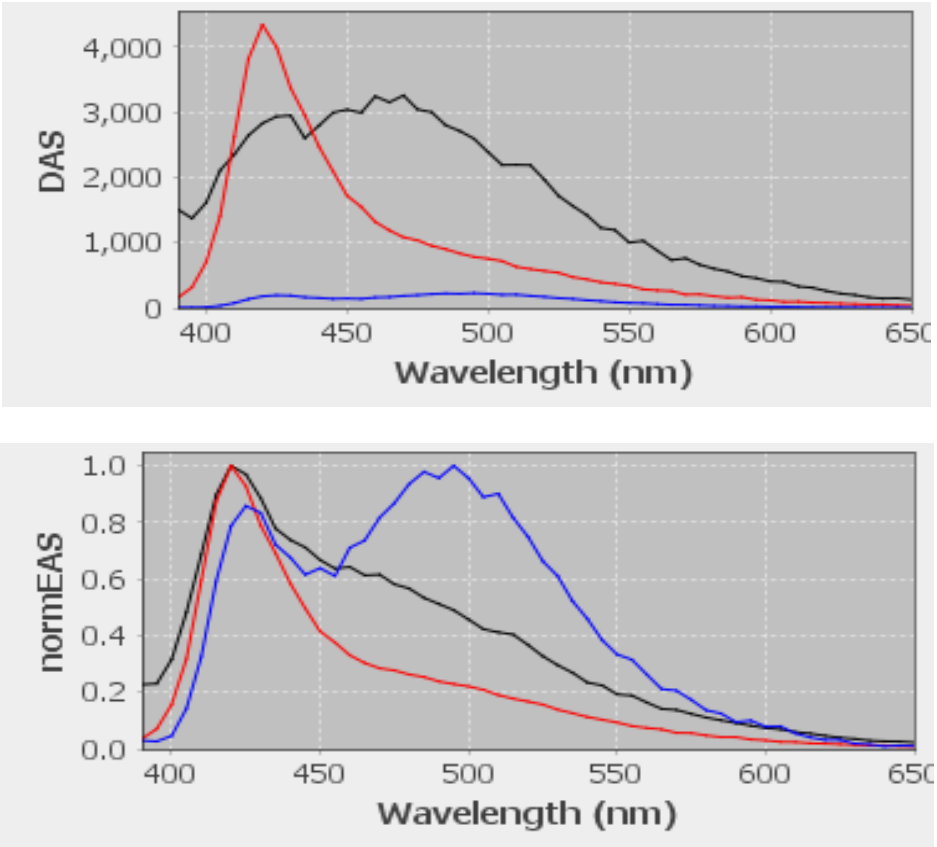

Figure S29. The results of global analysis of TRPL data measured for TLm-Hg^{2+} complex

Part S3: Average excited-state lifetime in solid state.

The source data for Tables S1, S2, and S3 are shown in Figures S30, S31, S32, S33, S34, S35, S36, S37, S38, S39, S40, S41, and S42.

Table S1. The excited-state lifetime constants in nanoseconds (ns) for different TLm solid samples (as indicated). The excitation wavelength was at 375 nm with a spectral resolution of ~30 ps. The monitored wavelength was at 450 nm.

TLm/Hg^{2+} ratios	τ_i (ns)	f_i	$\bar{\tau}$ (ns)	Mean $\bar{\tau}$ (ns)[a]	Chi-Square
TLmNFs (atm) (without metal ions)	0.1 2.1 7.7 173	0.06 0.14 0.45 0.35	65	38	1.017
100:1 (atm)	0.3 1.7 5.1 92	0.35 0.34 0.29 0.02	3.9	6.6	0.987
50:1 (atm)	0.3 1.9 6.3 22	0.21 0.35 0.42 0.02	3.8	4.2	1.010
13:1 (atm)	0.1 0.8 2.9 6.9	0.05 0.10 0.29 0.56	4.8	4.6	0.951
5:1 (atm)	0.05 0.6 2.1 5.8	0.14 0.19 0.27 0.39	3.0	2.9	1.143
200:1 (atm)	0.03 0.6 2.6 7.7	0.23 0.17 0.39 0.20	3.0		1.243
200,000:1 (atm)	0.04 0.40 2.02 6.49	0.16 0.21 0.35 0.28	3.0		1.140

[a]Values are presented as mean ± standard deviation for the data in Tables S1, S2 and S3.

Table S1. The excited-state lifetime constants in nanoseconds (ns) for different TLm solid samples (as indicated). The excitation wavelength was at 375 nm with a spectral resolution of ~30 ps. The monitored wavelength was at 450 nm (continued**)**

TLm/Hg^{2+} ratios	τi (ns)	fi	$\bar{\tau}$ (ns)	Mean $\bar{\tau}$ (ns)	Chi-Square
TLmNFs (vac) (without metal ions)	0.21 1.95 7.22	0.2653 0.4107 0.3239	3.2		1.378
1:5 (vac)	0.55 2.06 6.70	0.21 0.42 0.37	3.5		1.373
200:1 (vac)	0.30 1.942 6.504	0.1261 0.5646 0.3093	3.1		1.277
200,000:1 (vac)	0.425 2.129 7.256	0.1009 0.5435 0.3556	3.8		1.196
Solid TLm	0.11 1.04 3.23	0.2925 0.5195 0.188	1.2		1.304
TLm-Hg^{2+} solid complex	0.148 1.067 3.214	0.3757 0.4901 0.1342	1.0		1.253

Table S2. The excited-state lifetime constants in nanoseconds (ns) for TLmNFs(atm) with and without the addition of mercuric ions. The excitation wavelength was at 375 nm with a spectral resolution of ~30 ps. The monitored wavelength was at 430 nm.

TLm/Hg^{2+} ratios	τ_i (ns)	f_i	$\bar{\tau}$ (ns)	Mean $\bar{\tau}$ (ns)[a]	Chi-Square
TLmNFs (atm) (without metal ions)	0.1 2.1 7.7 173	0.13 0.31 0.52 0.04	12.1	38	1.02
100:1	0.3 1.7 5.1 92	0.31 0.37 0.29 0.04	5.6	6.6	0.99
50:1	0.3 1.9 6.3 22	0.18 0.41 0.31 0.10	5.0	4.2	1.01
13:1	0.1 0.8 2.9 6.9	0.05 0.10 0.29 0.56	4.2	4.6	0.95
5:1	0.05 0.6 2.1 5.8	0.18 0.13 0.40 0.29	2.6	2.9	1.14

[a]Values are presented as mean ± standard deviation for the data in Tables S1, S2 and S3.

Table S3. The excited-state lifetime constants in nanoseconds (ns) for TLmNFs(atm) with and without the addition of mercuric ions. The excitation wavelength was at 375 nm with a spectral resolution of ~30 ps. The monitored wavelength was at 470 nm.

TLm/Hg^{2+} ratios	τ_i (ns)	f_i	$\bar{\tau}$ (ns)	Mean $\bar{\tau}$ (ns)[a]	Chi-Square
TLmNFs (atm) (without metal ions)	0.1 2.1 7.7 173	0.12 0.15 0.55 0.19	37	38	1.02
100:1	0.3 1.7 5.1 92	0.34 0.32 0.25 0.09	10	6.6	0.99
50:1	0.3 1.9 6.3 22	0.24 0.34 0.40 0.02	3.7	4.2	1.01
13:1	0.1 0.8 2.9 6.9	0.04 0.13 0.22 0.62	4.2	4.6	0.95
5:1	0.05 0.6 2.1 5.8	0.08 0.19 0.30 0.43	3.2	2.9	1.14

[a]Values are presented as mean ± standard deviation for the data in Tables S1, S2 and S3.

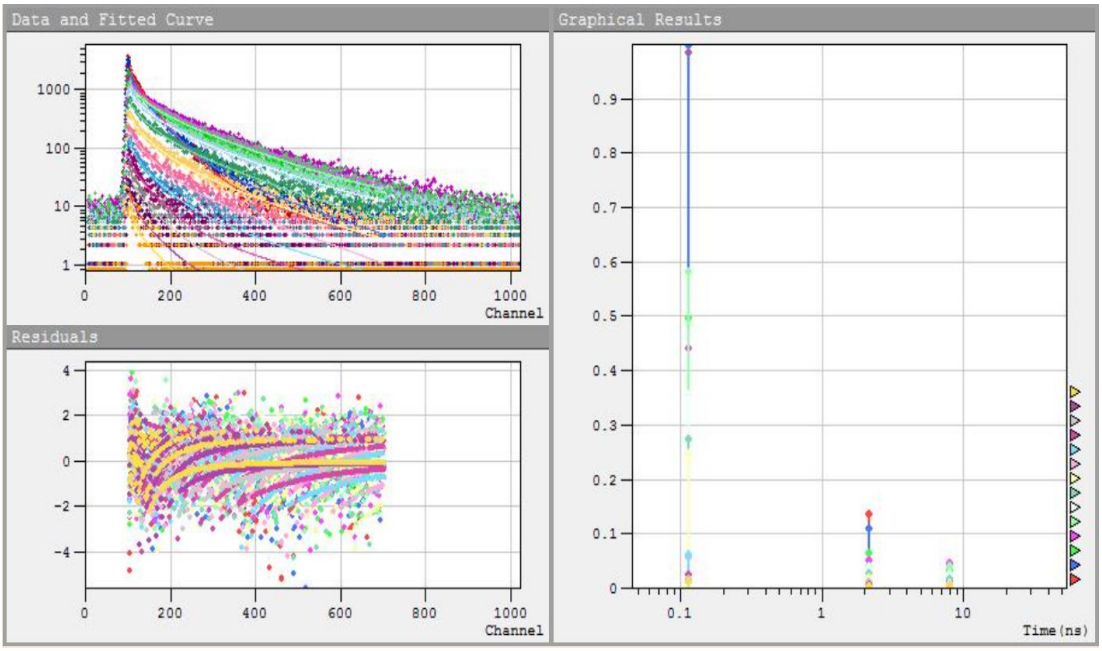

Figure S30. Collected emission decays of TLmNFs(atm). Data were measured over the entire emission spectrum from 390 to 650 nm every 20 nm with a dwell time of 10 s at each wavelength. Excitation was at 375 nm. Data at each wavelength were fitted to a four-exponential model convoluted with IRF of ~ 30 ps (as shown in the residuals).

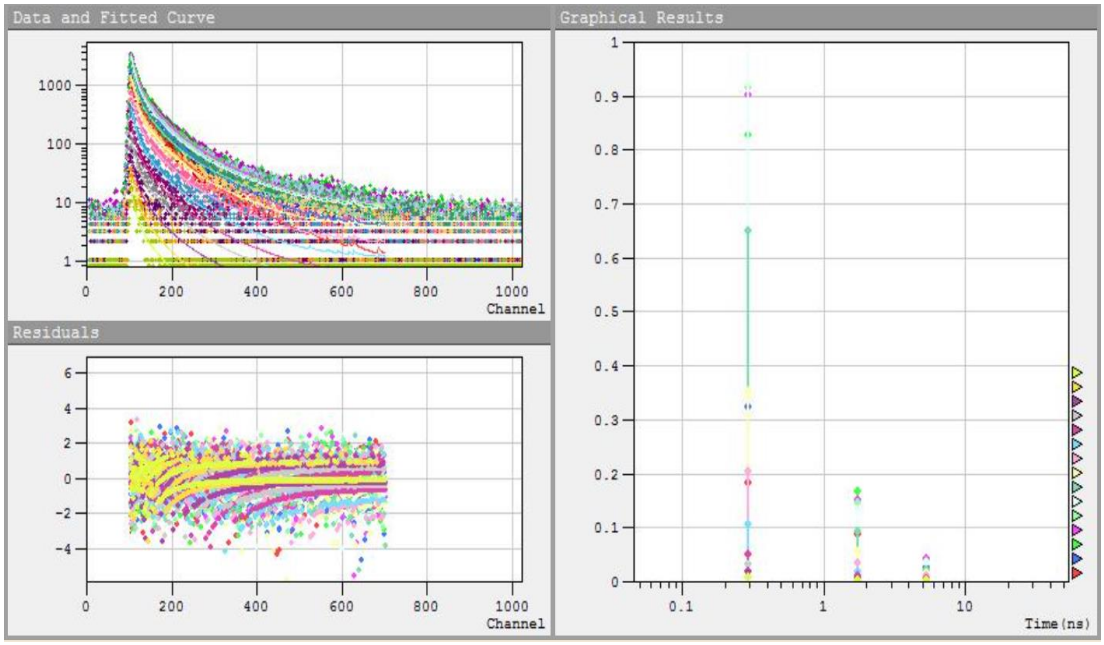

Figure S31. Collected emission decays of TLmNFs(atm)/Hg^{2+} in a 100:1 ratio. Data were measured over the entire emission spectrum from 390 to 650 nm every 20 nm with a dwell time of 10 s at each wavelength. Excitation was at 375 nm. Data at each wavelength were fitted to a four-exponential model convoluted with IRF of ~ 30 ps (as shown in the residuals)

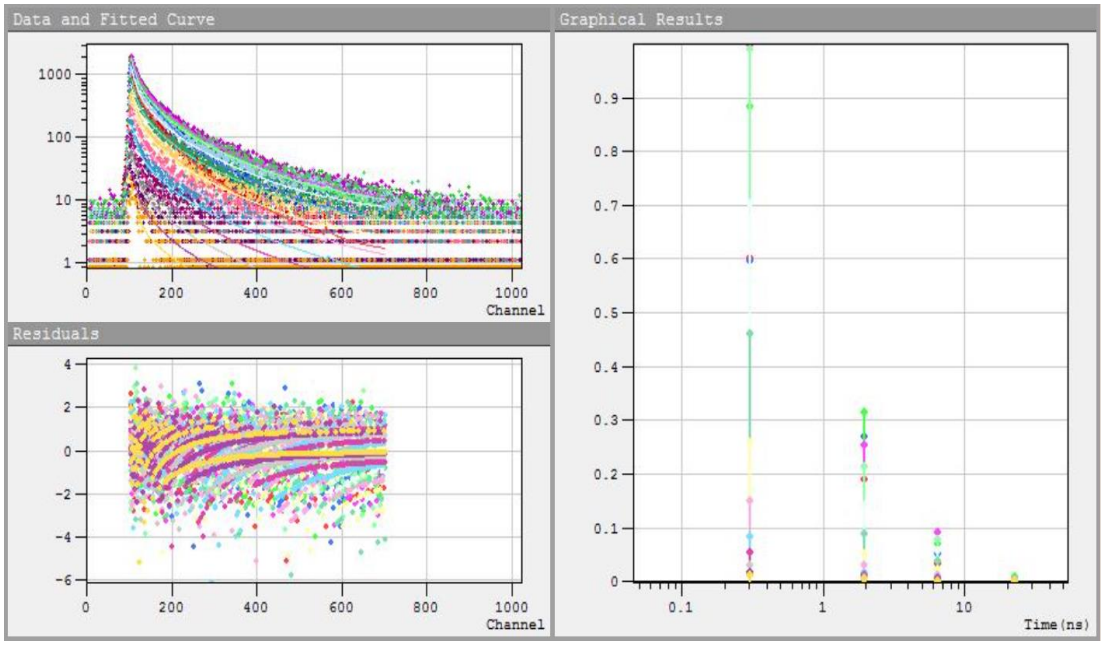

Figure S32. Collected emission decays of TLmNFs(atm)/Hg^{2+} in a 50:1 ratio. Data were measured over the entire emission spectrum from 390 to 650 nm every 20 nm with a dwell time of 10 s at each wavelength. Excitation was at 375 nm. Data at each wavelength were fitted to a four-exponential model convoluted with IRF of ~ 30 ps (as shown in the residuals)

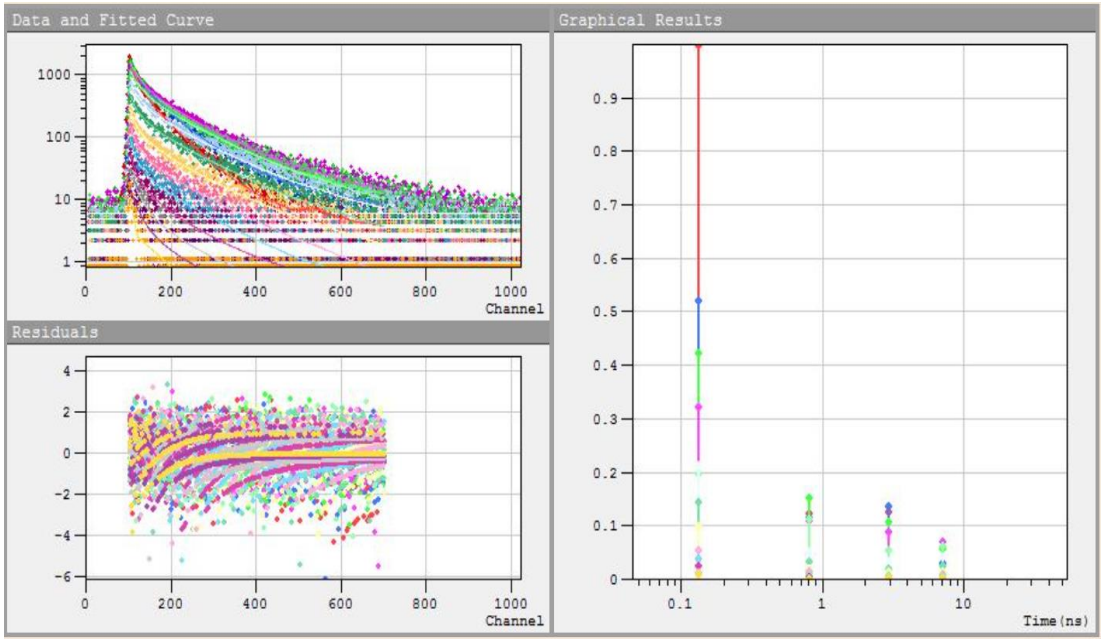

Figure S33. Collected emission decays of TLmNFs(atm)/Hg^{2+} in a 13:1 ratio. Data were measured over the entire emission spectrum from 390 to 650 nm every 20 nm with a dwell time of 10 s at each wavelength. Excitation was at 375 nm. Data at each wavelength were fitted to a four-exponential model convoluted with IRF of ~ 30 ps (as shown in the residuals)

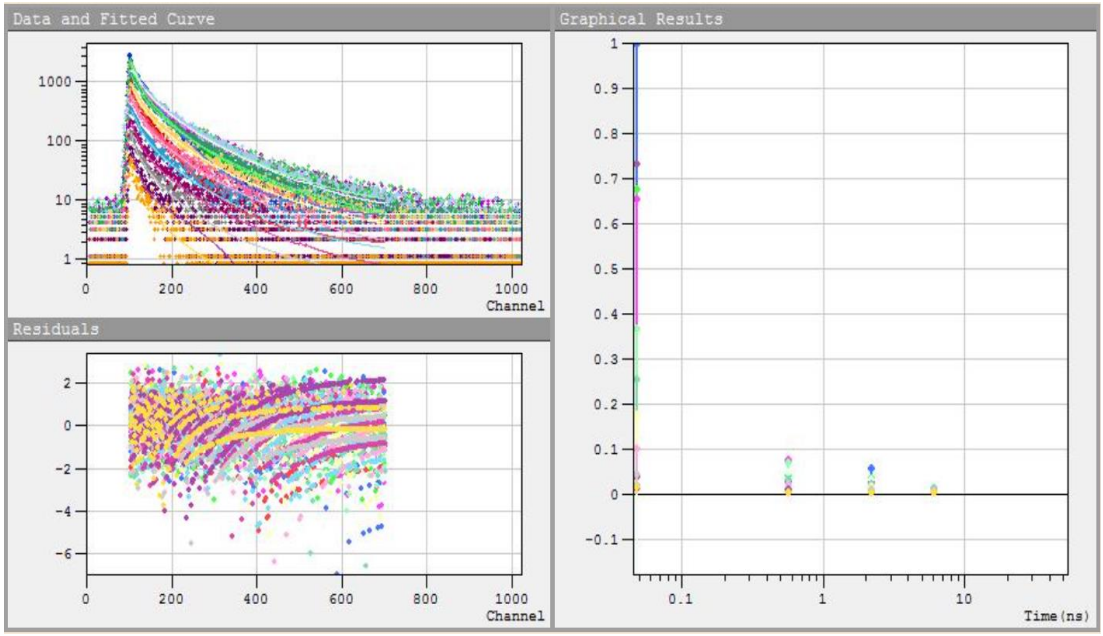

Figure S34. Collected emission decays of TLmNFs(atm)/Hg^{2+} in a 5:1 ratio. Data were measured over the entire emission spectrum from 390 to 650 nm every 20 nm with a dwell time of 10 s at each wavelength. Excitation was at 375 nm. Data at each wavelength were fitted to a four-exponential model convoluted with IRF of ~ 30 ps (as shown in the residuals)

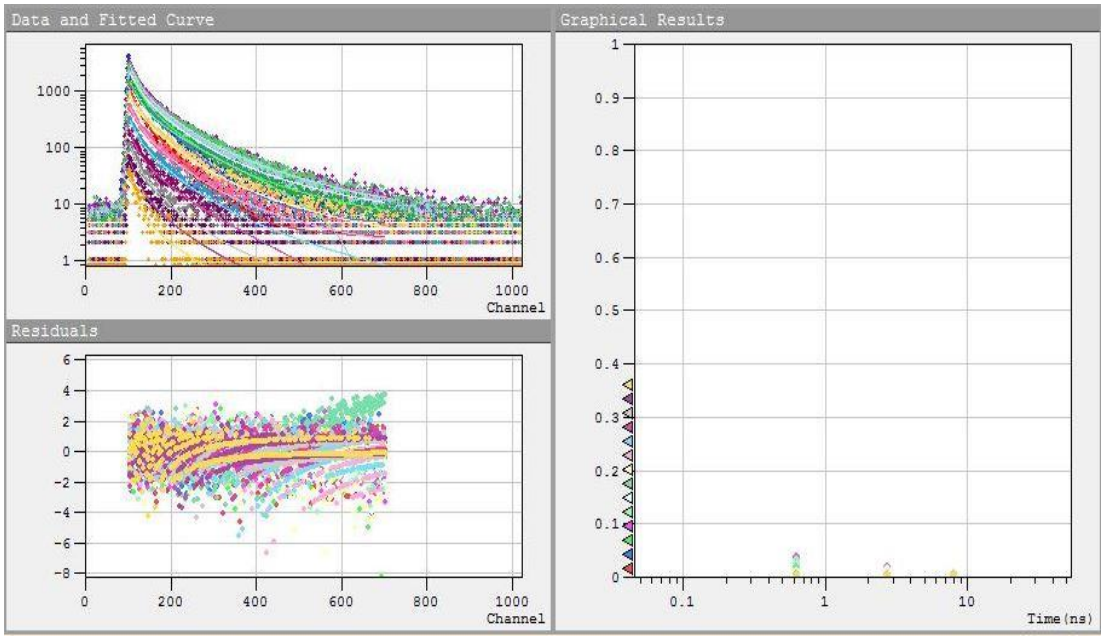

Figure S35. Collected emission decays of TLmNFs(atm)/Hg^{2+} in a 1:200 ratio. Data were measured over the entire emission spectrum from 390 to 650 nm every 20 nm with a dwell time of 10 s at each wavelength. Excitation was at 375 nm. Data at each wavelength were fitted to a four-exponential model convoluted with IRF of ~ 30 ps (as shown in the residuals)

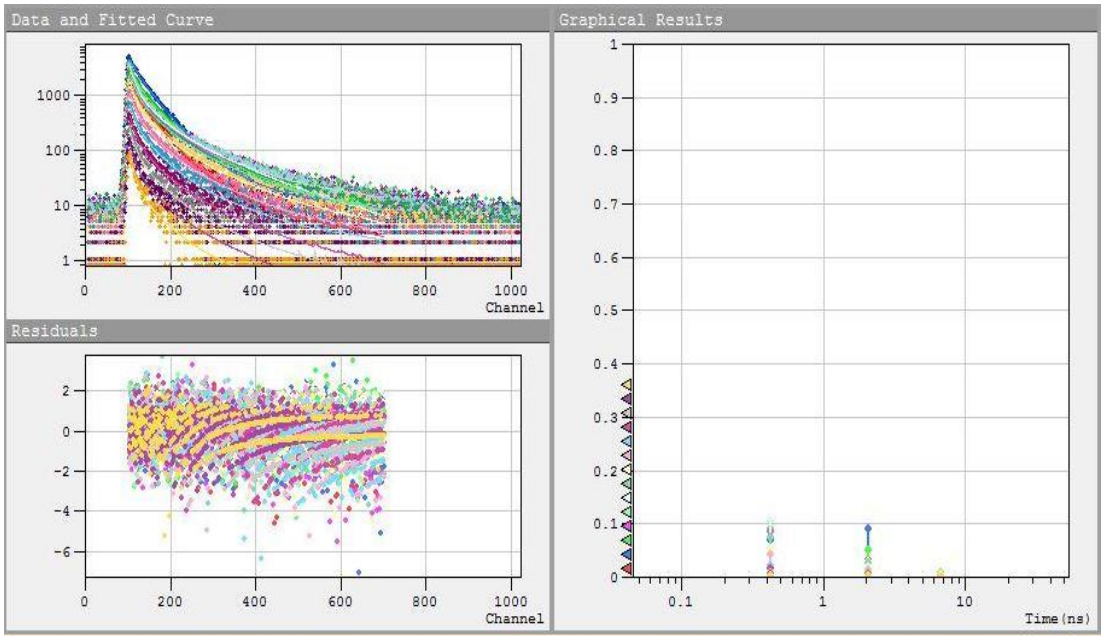

Figure S36. Collected emission decays of TLmNFs(atm)/Hg^{2+} in a 1:200,000 ratio. Data were measured over the entire emission spectrum from 390 to 650 nm every 20 nm with a dwell time of 10 s at each wavelength. Excitation was at 375 nm. Data at each wavelength were fitted to a four-exponential model convoluted with IRF of ~ 30 ps (as shown in the residuals)

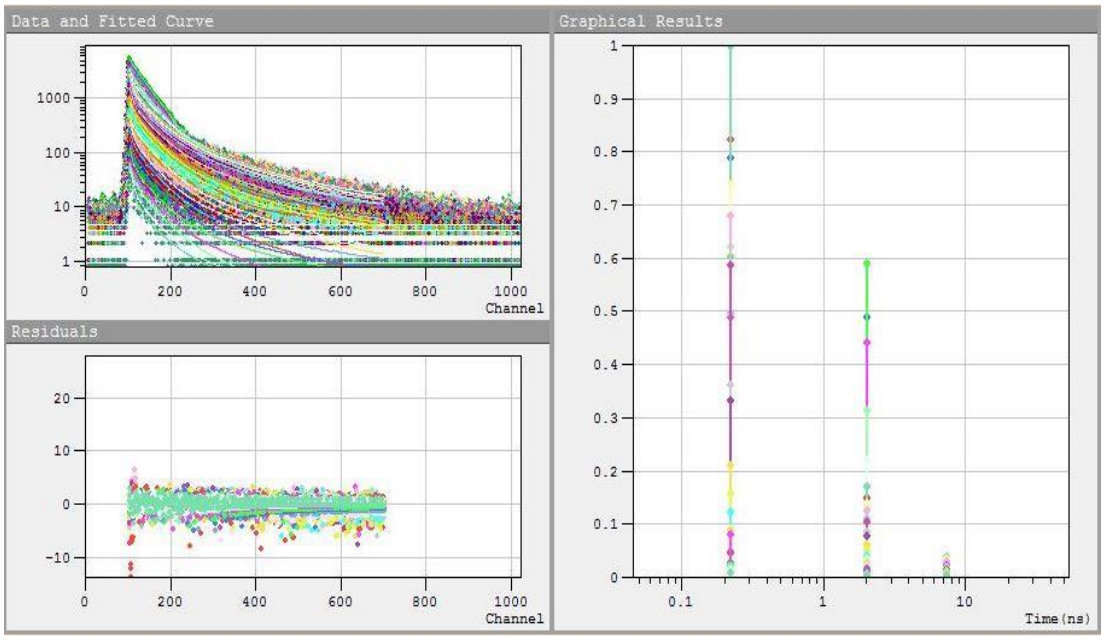

Figure S37. Collected emission decays of TLmNFs(vac). Data were measured over the entire emission spectrum from 390 to 650 nm every 10 nm with a dwell time of 10 s at each wavelength. Excitation was at 375 nm. Data at each wavelength were fitted to a four-exponential model convoluted with IRF of ~ 30 ps (as shown in the residuals)

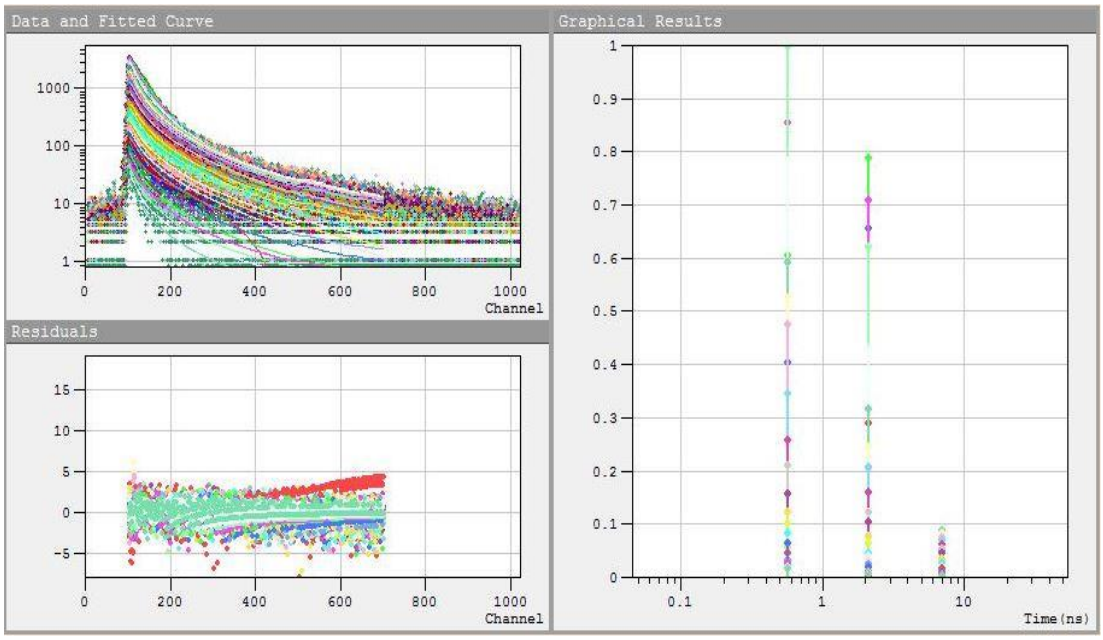

Figure S38. Collected emission decays of TLmNFs(vac)/Hg^{2+} in a 5:1 ratio. Data were measured over the entire emission spectrum from 390 to 650 nm every 10 nm with a dwell time of 10 s at each wavelength. Excitation was at 375 nm. Data at each wavelength were fitted to a four-exponential model convoluted with IRF of ~ 30 ps (as shown in the residuals).

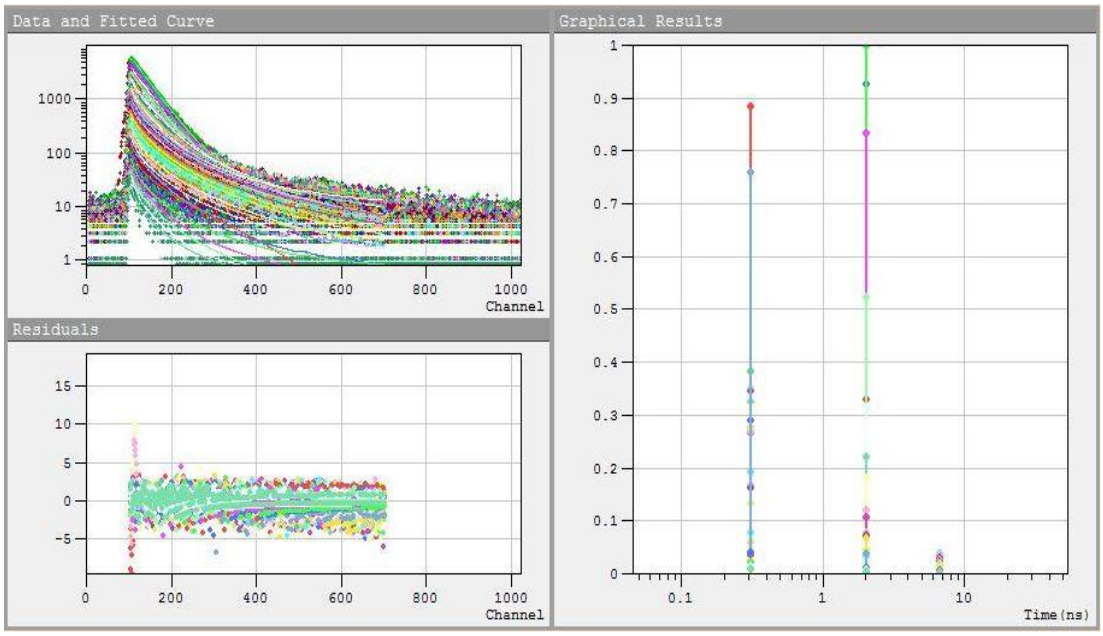

Figure S39. Collected emission decays of TLmNFs(vac)/Hg^{2+} in a 1:200 ratio. Data were measured over the entire emission spectrum from 390 to 650 nm every 10 nm with a dwell time of 10 s at each wavelength. Excitation was at 375 nm. Data at each wavelength were fitted to a four-exponential model convoluted with IRF of ~ 30 ps (as shown in the residuals)

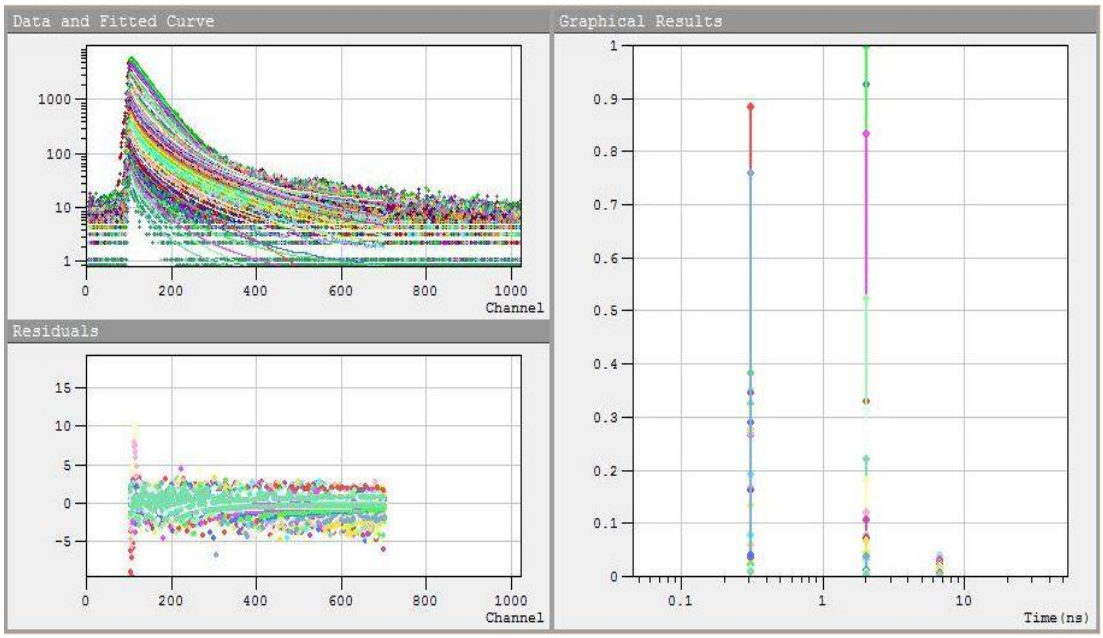

Figure S40. Collected emission decays of TLmNFs(vac)/Hg^{2+} in a 1:200,000 ratio. Data were measured over the entire emission spectrum from 390 to 650 nm every 10 nm with a dwell time of 10 s at each wavelength. Excitation was at 375 nm. Data at each wavelength were fitted to a four-exponential model convoluted with IRF of ~ 30 ps (as shown in the residuals)

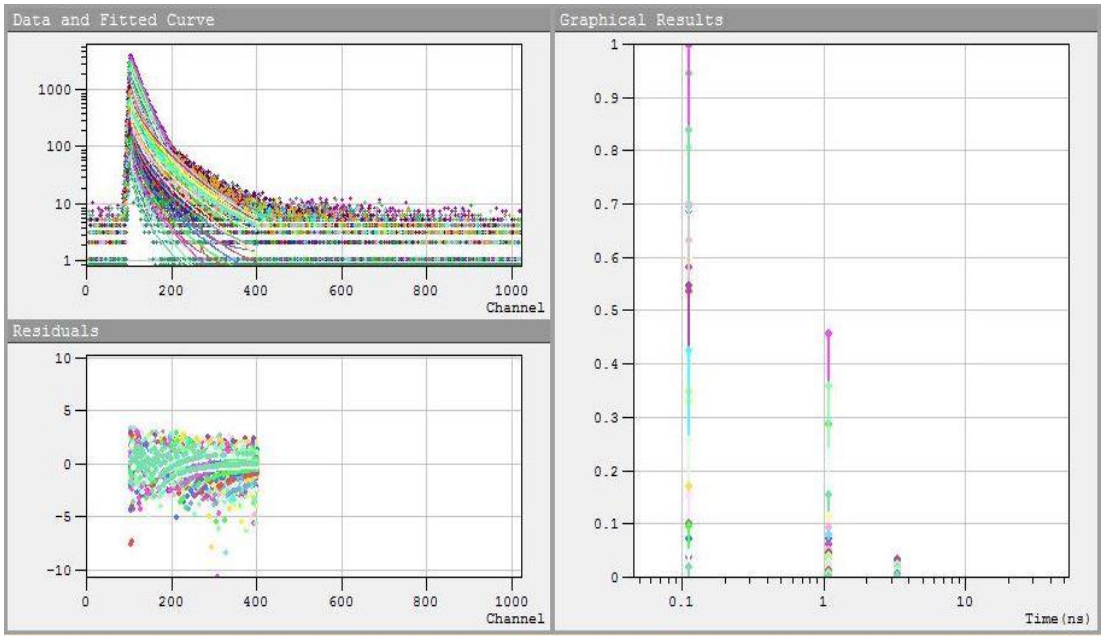

Figure S41. Collected emission decays of TLm solid. Data were measured over the entire emission spectrum from 390 to 650 nm every 10 nm with a dwell time of 10 s at each wavelength. Excitation was at 375 nm. Data at each wavelength were fitted to a four-exponential model convoluted with IRF of ~ 30 ps (as shown in the residuals)

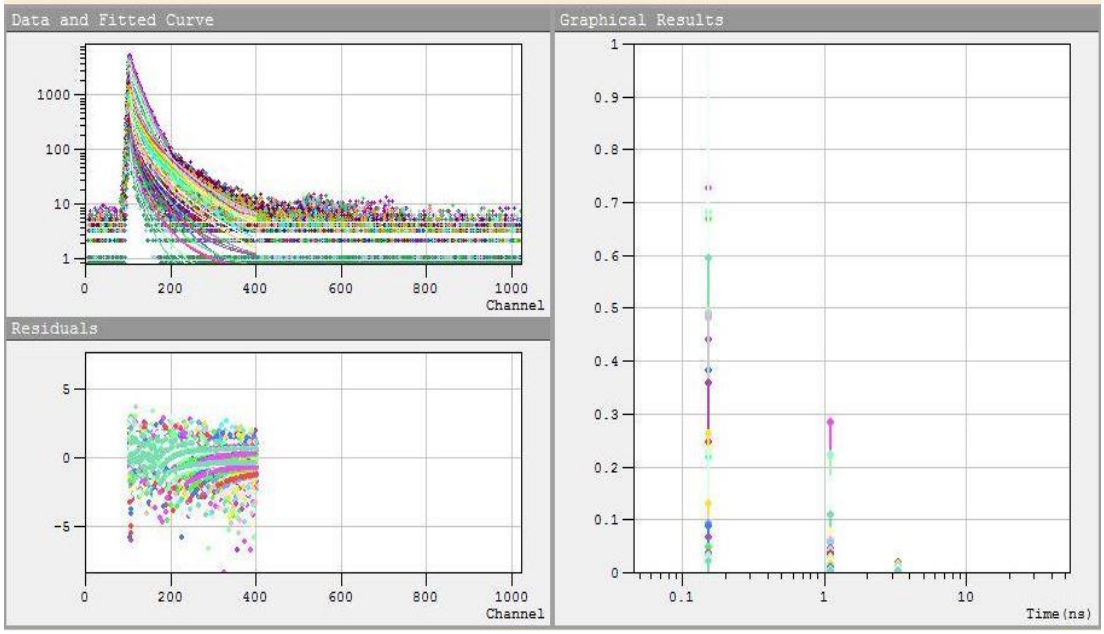

Figure S42. Collected emission decays of TLm-Hg^{2+} solid complex. Data were measured over the entire emission spectrum from 390 to 650 nm every 10 nm with a dwell time of 10 s at each wavelength. Excitation was at 375 nm. Data at each wavelength were fitted to a four-exponential model convoluted with IRF of ~ 30 ps (as shown in the residuals)

Part S4: UV–vis absorption and FTIR Spectra for TLm-Hg^{2+} complex.

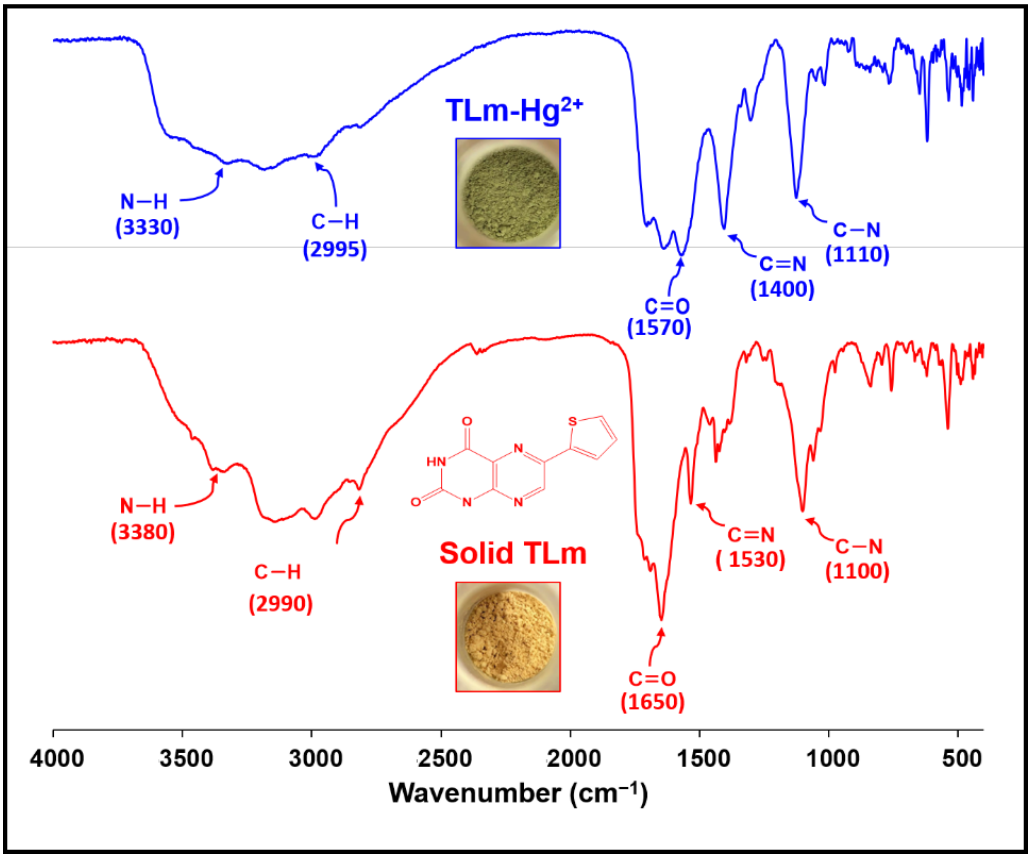

Figure S43. The FTIR Spectra for TLm and TLm-Hg^{2+} solids in KBr desks.

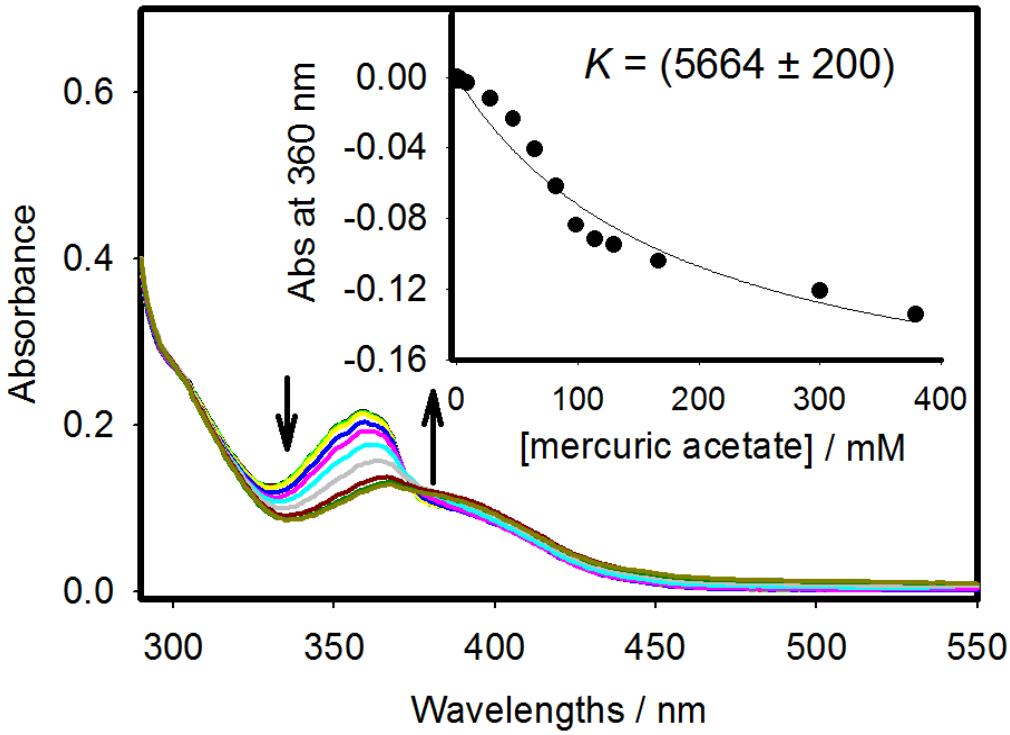

Figure S44. Binding titration of TLm with mercuric acetate at pH 3 showing the evolution of the UV−vis absorption spectra of TLm (10 μM) with the addition of mercuric acetate in water media. The inset shows the nonlinear fitting according to a 1:1 binding model (solid line, see the Experimental Section)

Standard Deviation Calculator

Result

Sample Standard Deviation, s	26.414200726125
Variance (Sample Standard), s^2	697.71
Population Standard Deviation, σ	21.567104580819
Variance (Population Standard), σ^2	465.14
Total Numbers, N	3
Sum:	114
Mean (Average):	38
Standard Error of the Mean ($SE_{\bar{x}}$):	15.250245899657

Confidence Interval Approximations, If sampling distribution of the mean follows normal distribution

Confidence Level	Range
68.3%, $SE_{\bar{x}}$	22.749754100343 - 53.250245899657
90%, $1.645SE_{\bar{x}}$	12.913345495065 - 63.086654504935
95%, $1.960SE_{\bar{x}}$	8.1095180366726 - 67.890481963327
99%, $2.576SE_{\bar{x}}$	-1.284633437516 - 77.284633437516
99.9%, $3.291SE_{\bar{x}}$	-12.188559255771 - 88.188559255771
99.99%, $3.891SE_{\bar{x}}$	-21.338706795565 - 97.338706795565
99.999%, $4.417SE_{\bar{x}}$	-29.360336138784 - 105.36033613878
99.9999%, $4.892SE_{\bar{x}}$	-36.604202941121 - 112.60420294112

A. Standard deviation and mean calculation for the average excited-state lifetime of TLmNFs(atm)

Standard Deviation Calculator

Result

Sample Standard Deviation, s	3.2593455375786
Variance (Sample Standard), s^2	10.623333333333
Population Standard Deviation, σ	2.6612444874949
Variance (Population Standard), σ^2	7.0822222222222
Total Numbers, N	3
Sum:	19.7
Mean (Average):	6.5666666666667
Standard Error of the Mean ($SE_{\bar{x}}$):	1.881784023503

Confidence Interval Approximations, If sampling distribution of the mean follows normal distribution

Confidence Level	Range
68.3%, $SE_{\bar{x}}$	4.6848826431637 - 8.4484506901697
90%, $1.645SE_{\bar{x}}$	3.4711319480042 - 9.6622013853291
95%, $1.960SE_{\bar{x}}$	2.8783699806008 - 10.254963352733
99%, $2.576SE_{\bar{x}}$	1.719191022123 - 11.41414231121
99.9%, $3.291SE_{\bar{x}}$	0.37371544531832 - 12.759617888015
99.99%, $3.891SE_{\bar{x}}$	-0.75535496878348 - 13.888688302117
99.999%, $4.417SE_{\bar{x}}$	-1.745173365146 - 14.878506698479
99.9999%, $4.892SE_{\bar{x}}$	-2.63902077631 - 15.772354109643

B. Standard deviation and mean calculation for the average excited-state lifetime of TLmNFs(atm)/Hg^{2+} in a 100:1 ratio.

Standard Deviation Calculator

Result

Sample Standard Deviation, s	0.73384830403383
Variance (Sample Standard), s^2	0.53853333333333
Population Standard Deviation, σ	0.59918463116324
Variance (Population Standard), σ^2	0.35902222222222
Total Numbers, N	3
Sum:	12.46
Mean (Average):	4.1533333333333
Standard Error of the Mean ($SE_{\bar{x}}$):	0.42368751587828

Confidence Interval Approximations, If sampling distribution of the mean follows normal distribution

Confidence Level	Range
68.3%, $SE_{\bar{x}}$	3.729645817455 - 4.5770208492116
90%, $1.645SE_{\bar{x}}$	3.4563673697136 - 4.8502992969531
95%, $1.960SE_{\bar{x}}$	3.3229058022119 - 4.9837608644548
99%, $2.576SE_{\bar{x}}$	3.0619142924309 - 5.2447523742358
99.9%, $3.291SE_{\bar{x}}$	2.7589777185779 - 5.5476889480888
99.99%, $3.891SE_{\bar{x}}$	2.5047652090509 - 5.8019014576157
99.999%, $4.417SE_{\bar{x}}$	2.281905575699 - 6.0247610909677
99.9999%, $4.892SE_{\bar{x}}$	2.0806540056568 - 6.2260126610099

C. Standard deviation and mean calculation for the average excited-state lifetime of TLmNFs(atm)/Hg^{2+} in a 50:1 ratio.

Standard Deviation Calculator

Result

Sample Standard Deviation, s	0.3605551275464
Variance (Sample Standard), s^2	0.13
Population Standard Deviation, σ	0.29439202887759
Variance (Population Standard), σ^2	0.086666666666667
Total Numbers, N	3
Sum:	13.8
Mean (Average):	4.6
Standard Error of the Mean ($SE_{\bar{x}}$):	0.20816659994661

Confidence Interval Approximations, If sampling distribution of the mean follows normal distribution

Confidence Level	Range
68.3%, $SE_{\bar{x}}$	4.3918334000534 - 4.8081665999466
90%, $1.645SE_{\bar{x}}$	4.2575659430878 - 4.9424340569122
95%, $1.960SE_{\bar{x}}$	4.1919934641046 - 5.0080065358954
99%, $2.576SE_{\bar{x}}$	4.0637628385375 - 5.1362371614625
99.9%, $3.291SE_{\bar{x}}$	3.9149237195757 - 5.2850762804243
99.99%, $3.891SE_{\bar{x}}$	3.7900237596077 - 5.4099762403923
99.999%, $4.417SE_{\bar{x}}$	3.6805281280358 - 5.5194718719642
99.9999%, $4.892SE_{\bar{x}}$	3.5816489930612 - 5.6183510069388

D. Standard deviation and mean calculation for the average excited-state lifetime of TLmNFs(atm)/Hg^{2+} in a 13:1 ratio.

Standard Deviation Calculator

Result

Sample Standard Deviation, s	0.30550504633039
Variance (Sample Standard), s^2	0.093333333333333
Population Standard Deviation, σ	0.24944382578493
Variance (Population Standard), σ^2	0.062222222222222
Total Numbers, N	3
Sum:	8.8
Mean (Average):	2.9333333333333
Standard Error of the Mean ($SE_{\bar{x}}$):	0.17638342073764

Confidence Interval Approximations, If sampling distribution of the mean follows normal distribution

Confidence Level	Range
68.3%, $SE_{\bar{x}}$	2.7569499125957 - 3.109716754071
90%, $1.645SE_{\bar{x}}$	2.6431826062199 - 3.2234840604468
95%, $1.960SE_{\bar{x}}$	2.5876218286876 - 3.2790448379791
99%, $2.576SE_{\bar{x}}$	2.4789696415132 - 3.3876970251535
99.9%, $3.291SE_{\bar{x}}$	2.3528554956858 - 3.5138111709809
99.99%, $3.891SE_{\bar{x}}$	2.2470254432432 - 3.6196412234235
99.999%, $4.417SE_{\bar{x}}$	2.1542477639352 - 3.7124189027315
99.9999%, $4.892SE_{\bar{x}}$	2.0704656390848 - 3.7962010275819

E. Standard deviation and mean calculation for the average excited-state lifetime of TLmNFs(atm)/Hg^{2+} in a 5:1 ratio.

جامعة الإمارات العربية المتحدة
United Arab Emirates University
UAEU
Shrieen M Wolicod
UAEU Libraries
DigitizationDepatment
United Arab Emirates

Digitally signed by Shrieen
DN: cn=Shrieen, o=UAEU, ou=Libraries Deanship, email=shrieen@uaeu.ac.ae, c=AE
Date: 2019.09.11 11:40:58 +04'00'